UNIVERSITY OF CALIFORNIA, SAN DIEGO

Approaches to studying collective migration, diffusion and integrated organ-on-a-chip technologies

A dissertation submitted in partial satisfaction of the

requirements for the degree Doctor of Philosophy

in

Bioengineering

by

Han Liang Lim

Committee in Charge:

Professor Shyni Varghese, Chair
Professor Pedro Cabrales
Professor Geert Schmid-Schoenbein
Professor Anne Wallace
Professor Jing Yang

2017

The dissertation of Han Liang Lim is approved, and it is acceptable in quality and form for publication on microfilm and electronically:

Chair

University of California, San Diego

2017

Epigraph

“For a successful technology, reality must take precedence over public relations, for Nature cannot be fooled.”

Richard P. Feynman

Table of Contents

List of Figures

Acknowledgements

I would like to sincerely thank and acknowledge many individuals who have contributed tremendously towards the completion of my graduate degree. I would like to first and foremost thank my wife, Virginia Chan, for supporting me throughout the different stages of my life. I extend this gratitude to her for being tolerant of my willfulness, and staying with me through the worst of times. I consider myself truly lucky to have met someone like her, who has come to accept me completely for who I am, and helped me grow to who I have become.

Secondly, I would like to thank my Ph.D. advisor, Shyni Varghese, for being the best advisor one can have. I will always remember joining the lab as an undergraduate student and working with Shyni through most weekends and holidays. She was always patiently guiding me through each step of every experiment. Throughout the years, she has devoted tremendous amounts of time and effort to teach me not only to become a better scientist, but also a better person. Lastly, I would like to thank her for tolerating my many mistakes and allowing me to pursue my numerous curiosities, ultimately culminating in this thesis.

I would also like to thank those who have helped shaped and molded my scientific abilities throughout my stint as a graduate student. Specifically, I would like to extend my gratitude to Aereas Aung, a brilliant colleague and close friend who I consider my second mentor in this lab. Since joining the mechanics subgroup, we have embarked on a series of zany and unlikely projects, many of which despite not coming to fruition, have taught me much about the ways to approach Science.

In addition, I would like to thank all the present and the past Varghese lab members, from the first members such as Chao Zhang, to our newest recruit in Jasper Zeng. I will always appreciate the many interactions, scientific or otherwise, that we have had. This lab has been unique in its collaborative nature and wide range of research topics, and I have learned much from everyone that has walked through and sat at these benches.

I would also like to extend my gratitude to my many teachers and mentors over the years who have selflessly dedicated time and energy to my mental growth. Through them I came to first realize my passion for Science. They have always generously shared every ounce, every iota of what they know, each one supplementing knowledge that others have left to me. They have truly helped mold my understanding of the world from the smallest atomic particles to the biggest astronomical bodies in the sky, which has helped me immensely in trying to discover new things for myself.

Lastly, I would like to thank my parents, Monghoo Lim and Kweechin Toh, for the hardships they have endured and the sacrifices they have had to make to ensure that I received the best possible education that the world could offer.

Chapter 2, in full, is a reprint of the material that has been submitted to Biotechnology Journal. “Alternating Control and Dynamic Malleability in Cell Pairs”. Lim, Han L.; Aung, Aereas; Arya, Gaurav; Varghese, Shyni. The dissertation author was the primary investigator and author of this paper.

Chapter 3, in full, is a reprint of the material is in preparation for submission to a scientific journal. “Quantifying Diffusivity amongst Cancer Spheroids Cultured in Matrices of Different Stiffnesses”. Lim, Han L.; Aung, Aereas;Varghese, Shyni. The dissertation author will be the primary investigator and author of this paper.

Chapter 4, in full, is a reprint of the material is in preparation for submission to a scientific journal. "The development of an integrated multi-organ organ-on-a-chip platform". Lim, Han L.; Agrawal, Gaurav; Varghese, Shyni. The dissertation author will be the primary investigator and author of this paper.

Vita

2009 Bachelor of Science in Bioengineering: Biotechnology,

University of California San Diego, La Jolla, United States

2017 Doctor of Philosophy in Bioengineering,

University of California San Diego, La Jolla, United States

Publications

Lim, H.L., Agrawal, G., and Varghese, S. "'You-on-a-chip': a modular integrated Organ-on-a-Chip platform for patient specific cancer drug testing" 2017. (in preparation).

Lim, H.L.†, Aung, A.†, and Varghese, S. "Quantifying Diffusivity amongst Cancer Spheroids Cultured in Matrices of Different Stiffnesses." 2017. (in preparation).

Lim, H.L.†, Aung, A.†, Arya, G.*, and Varghese, S*. "Mechanical oscillations and dynamic malleability in collectively migrating cell clusters." 2017.(submitted).

Aung, A., Theprungsirikul, J., **Lim, H.L.**, and Varghese, S. "Chemotaxis-driven assembly of endothelial barrier in a tumor-on-a-chip platform." *Lab on a Chip*. 16(10): 1886-98, 2016.

Aung, A.†, Bhullar, I.†, Theprungsirikul, J., Davey, S.K., **Lim, H.L.**, Chiu, Y., Ma, X., Dewan, S., Lo, Y., McCulloch, A., and Varghese, S. "3D cardiac μtissues within microfluidics device with real-time contractile force read out." *Lab on a Chip*. 16: 153-162. 2016.

Davey, S.K.†, Aung, A.†, Agrawal, G., **Lim, H.L.**, Kar, M., and Varghese, S. "Embedded 3D photo-patterning of hydrogels with diverse and complex architectures for tissue engineering and disease models." *Tissue Engineering: Part C*. 21(11): 1188-1196. 2015.

Kabra, H.†, Hwang, Y.S.†, **Lim, H.L.**, Kar, M., Arya, G., and Varghese, S. "Biomimetic Material-Assisted Delivery of Human Embryonic Stem Cell Derivatives for Enhanced In

Vivo Survival and Engraftment" *ACS Biomaterials Science & Engineering*. 1(1): 7–12. 2014.

Lim, H.L., Hwang, Y.S., Kar, M., and Varghese, S. "Smart hydrogels as functional biomimetic systems." *Biomaterials Science.* 2(5):603-618. 2014

Lim, H.L., Chuang, J.C., Tran, T., Aung, A., Arya, G.*, and Varghese, S.* "Dynamic Electromechanical Hydrogel Matrices for Stem Cell Culture." *Advanced Functional Materials.* 21 (1): 55-63. 2011.

Abstract of the Dissertation

Approaches to studying collective migration, diffusion and integrated organ-on-a-chip technologies

by

Han Liang Lim

Doctor of Philosophy in Bioengineering

University of California, San Diego, 2017

Professor Shyni Varghese, Chair

Cancer ranks amongst the most lethal diseases worldwide, partly due to there being more than 120 different types of cancer, each one different from the other (1). Even for

cancers from the same organ, different mutations in different cells within the same tissue can give rise to different types of cancer, which may require completely different treatments (1). Due to advancements in medical and pharmacological sciences, different drug regiments for different types of cancer exist, which has contributed to improving the survival rates for many cancer patients (2). However, due to inherent patient-to-patient differences in genetic and epigenetic makeup, not every patient responds in the same manner to the same treatment (3). To this end, to provide a more comprehensive treatment for cancer patients, scientists and doctors are suggesting personalized medicine as the new paradigm in cancer treatments to tailor drug regiments for each patient (3, 4). To realize this, drug testing platforms with cells derived from the patient should be used to obtain information about the specific patient's sensitivity to different drugs. Here we demonstrate a proof-of-concept 'you-on-a-chip' integrated device that utilizes organ-on-a-chip systems to recapitulate the patient's own physiological state outside of the human body. The organ-on-a-chip devices used here will consist of a 'cancer-on-a-chip' device containing the patient's own cancer cells, integrated with the 'liver-on-a-chip', 'heart-on-a-chip' and 'muscle-on-a-chip' devices. Each chip will contain micro-tissues derived from the same patient's own induced pluripotent cells. Here in this dissertation, I detail studies leading up to the development of this integrated organ-on-a-chip system, which we propose can be used as a personalized drug testing platform to tailor patients' treatments. Furthermore, such devices can also be used as a drug testing platform by pharmaceutical companies to elucidate the most efficacious drug from thousands of drug candidates.

Chapter 1 is a literature review focusing on collective migration, diffusion and organ-on-a-chip technology. The first segment focuses on the mechanical regulation of

collective migration, from the development of tools that allow us to elucidate these mechanical forces to the modern understanding of the different biological mechanism at play during collective migration. In the second segment, I cover studies that have examined diffusion of matter into cancer in many in vivo and in vitro platforms. Results from these studies show that there are multiple biological and physical barriers that can passively inhibit the diffusion of small molecules into tissue and into cancer cells. Lastly, in the final segment, I cover developments in the organ-on-a-chip field, such as the design and development of many different types of organ-on-a-chip platforms, as well as key studies that demonstrate integration of different organ-on-a-chips.

Collective migration is a key biological process that is involved in wound healing, morphogenesis, and cancer metastasis. In Chapter 2, using a protein-patterned platform, my colleagues and I study the mechanical interactions between two attached cells undergoing collective migration. Our results show that the role of the leading cell alternates between the two cells, as the pair migrates along the direction of the leading cell. We have also observed cooperativity between two cells in which the trailing cell mechanically softens itself to allow the leading cell to pull it along. Together, our observations show the two cells engaging in a mechanical "tug-of-war" where the trailing cell actively adjusts its own mechanical malleability to facilitate subtle movements of the cell pair.

Diffusion plays a key role in the transport of molecular agents into non-vascularized tumors. Past methods studying this have generalized the diffusivity within tumors by assuming its constant spatially in the tumor. However, recent studies have shown that microenvironmental factors, such as extracellular matrix rigidity, can play a role in affecting growth and packing within tumors, which we hypothesize can affect the spatial

variation of diffusivity in the tumor. In chapter 3, I utilized a cancer-on-a-chip device as a platform to quantify the spatial variations in the diffusivity of a spheroid encapsulated within gelatin methacrylate hydrogels of different rigidities. Our results show that substrates of different rigidities can impact the diffusion of small molecules in the deepest regions of cancer spheroids, which may affect the efficacy of drugs administered.

Chapter 4 describes integrating the simplified cancer-on-a-chip device into an integrated system comprising cancerous, muscle, heart and liver tissues. Such platforms can be used to understand tissue-tissue or even organ-organ cross talk. They can also be used measure off-target side effects of anti-cancer agents on humans, thereby allowing us to bypass animal models to obtain more clinically relevant drug efficacy results. Here we show that we can build different organs in different devices, and then integrate them in a modular manner while sustaining viability in them for short periods of time. Our results also demonstrate the continual functionality of these organs through this time.

Chapter 1: Past studies in collective migration, diffusion and organ-on-a-chip microphysiological platforms

1.1 Introduction

In this chapter, I will address several topics that have been of interest to the scientific community over the past decade. They are: the collective migration of cells, diffusion of small molecules through cells and tissue, and organ-on-a-chip micro-physiological platforms that can be used to study organ-organ crosstalk and interactions.

Firstly, the collective migration of cells plays a key role in important biological processes such as morphogenesis, wound healing, angiogenesis, and in disease progression such as cancer metastasis (5, 6). During collective migration, groups of cells would migrate together in a coordinated and efficient manner in order to achieve certain biological objectives (7). Studies have suggested that this coordination is a result of a combination of biochemical and mechanical signaling amongst the cells in the group (5, 7-9). However, this interplay between biochemical aspect of collective migration (10-12), and the mechanical signaling component (13, 14) is still poorly understood. In the next subsection, I will lay out studies that looked into this interplay between the mechanical and biochemical regulation of collective migration.

Next, I will address the current understanding of diffusion in the context of mass transfer into tumors or neoplastic tissues. Tumors are known for their ability to continue growing at sites away from blood vessels, which leads to the difficulty of trying to eradicate cancer with drugs that are delivered via the circulatory system. In many cases drugs enter

a tumor via diffusion, which is a slow process that can lead to prolonged exposure of a sub-lethal dose of the drug (15-18). Cancer cells that survive this can gain adaptive resistance to the drug, thereby making them even hard to kill (19-21). To better treat cancer, good models should be to assess the diffusivity of different drugs, to ensure the complete eradication of the tumor. Here in the next subsection, I will describe several key platforms that have been develop to study this drug penetration.

Lastly, emerging studies have shown that micro-physiological organ-on-a-chip systems have the potential to recapitulate organ-level functions in vitro (22-24). Here in this section I will go on to describe some landmark studies that have defined each of their respective organs, before addressing studies that integrated multiple organ-on-a-chip devices them into a whole device that demonstrates the capability for organ-organ crosstalk (25-28). As we increase the number of different organ types, such integrated devices will allow us to recreate whole human physiologies in vitro, which will have immense impact on both the medical and pharmaceutical industry.

1.2. Mechanical regulations of collective migration

Collective migration is the main mode of cellular migration in wound healing, cancer metastasis and morphogenesis(5, 6). Over the past two decades, it has attracted considerable attention from the scientific community, to try to understand the complex yet coordinated nature of the process (29-31). Understanding this will help further the understand of the processes that utilize collectively migrating cells, which may help us with wound healing or stopping cancer metastasis.

For collective migration to take place, cells come in contact with each other, allowing cell surface proteins such as cadherins on both cells' surfaces to come into contact and form cell-cell junctions that anchors the cells to each other (32, 33). Once joined, individual cells cannot pull apart from each other, and the cells that are attached to each other this way cannot migrate without dragging other cells that its attached to with it (Fig. 1.1) (7, 34).

Prior to forming multi-cellular collectives, integrin proteins on individual cells' surfaces bind to extracellular matrix proteins on the extracellular side (35), and is connected to cellular cytoskeleton through focal adhesions on the cytosolic side (36). Myosin motor proteins pull on the cytoskeletal actin, which transduces forces through the cytoskeleton across integrin proteins to the attached substrate, which allows cells to attach themselves to the environment (36). This force, known as the traction force, has been shown to play key roles in affecting cellular behavior, such as single cell migration, proliferation and differentiation of stem cells (37-40).

Conversely, after forming multi-cellular collectives, cells attached to other cells lose their ability to bind to their surrounding substrate, thereby losing traction against their surroundings (35, 41). This has become one of the identifying hallmarks of collective migration – a localized loss of traction at cell-cell junctions (Fig. 1.2) (35, 42). Formation of these cell-cell junctions in the cells behind the leading cells also prevents the trailing cells from becoming leading cells themselves (43-46). Biochemically, leading cells contain activated rac protein(47, 48), which facilitates the formation of lamellipodia at the leading edge via increased expression of actin branching protein arp2/3 (49, 50). However, formation of cell-cell junctions inactivates the expression of rac protein in the trailing cells,

rendering them unable to form additional lamellipodia (43, 45, 46). As a result, the motility of cell trailing is now reliant on their anchorage to their surrounding cells, against which they can exert pushing or pulling forces (13). Many in vitro models have thus been developed to quantify these push/pull forces and how they can constitute mechanical signaling between cells.

1.2.1. In vitro models and tools for determining intercellular stress in cellular collectives

To calculate the mechanical forces that exist for a group of attached cells, first, the traction forces that is exerted by the cellular collective on the underlying substrate must be determined (51, 52). Cell culture platforms, such as hydrogels and silicone substrates or silicone nanopillars on which cells can be grown, have been often used to obtain this traction force (52-54). In the case of hydrogels or silicone substrates, fluorescent nanoparticles are embedded within them from the gel synthesis step, and cells are grown on these substrates (54, 55). As the cells migrate, and the amount of strain in the hydrogel because of cellular traction forces can be obtained by tracking, using fluorescent microscopy, the small displacements of the embedded fluorescent nanoparticles. The traction forces can be obtained from these displacements by solving a system of linear elastostatic equations. Next, using this traction force as a computational input, the intercellular forces are then solved using different computational tools such as finite element analysis (52, 55).

Many of these studies have explored the implications of the phenotypic changes as cells start migrating in collectives. For example, the loss of substrate adhesion translates

into a general loss of traction stress and is reported in studies by Trepat and colleagues, Gardel and colleagues and Chien and colleagues (35, 54, 56). Studies have even shown that the cell-cell adhesion is strong enough for the leading cells to create epithelial bridges to move large cell sheets with only a small track of substrate for it to adhere itself to (56).

Others have used synthetic biological tools to modify proteins into molecular stress sensors within the cell. In a proof-of-concept study of one such tool, Schwartz and colleagues have engineered a fluorescent resonance energy transfer (FRET) system that can act as a tension sensor consisting of two fluorophores, the cyan mTFP1 and the yellow venus (A206K) separated by an elastic linker (amino acid sequence $(GPGGA)_8$) (57). As the cell cytoskeleton pulls on the vinculin, the elastic linker is stretched, which brings the yellow venus fluorophore away from its quencher mTFP1, such as excitation of the venus fluorophore would lead to zero excitation in mTFP1. However, as the cytoskeleton undergoes relaxation, the two fluorophores will be pulled closer together by the elastic linker, and excitation of the yellow venus fluorophore will yield a signal from the cyan mTFP1. The group then proceeded to calibrate this molecular biosensor, giving it sensitivity in the pN range. As vinculin is involved in mechanotransduction between cells, we will be able to measure the tension between cells using one such device.

Used together, these tools have been used broadly to obtain dynamic intercellular stress profiles, and when combined with modern biomolecular tools, grant us to insights into how cellular mechanics can lead to phenotypical changes in cells that facilitate collective migration.

1.2.2. Intercellular stress facilitates leading cell migration

As many studies have demonstrated the loss of traction forces in trailing cells in the cellular collective, scientists initially believed that the leading cells at the edges of these cellular collectives are solely responsible for dragging the passively-attached trailing cells along in the direction of migration. However, as more results show that this collective migration is a more efficient process compared to the independent migration of each individual cell (7, 58), it was suggested that the trailing cells may play more than a passive role in the migratory process.

One mechanical manifestation in which trailing cells play an active role in collective migration is by propagating mechanical waves within the migratory sheet(13, 52). For a migrating sheet expanding against free space on both sides, it was observed that cells in the middle undergo periodic oscillatory strains that propagates from the middle out in periodic intervals. This suggests that the cells not located at the leading front are capable generating force by themselves to grant them motility (13). Further experiments performed on a migrating sheet of epithelial cells in vitro reveal an interplay between the protein, RhoA, an upstream regulator of myosin activity, and mechanical forces in the trailing cells (14, 53). Specifically, a linear correlation was observed between RhoA activity and stresses exerted by the cells. It was observed that RhoA activity increases not only at the leading front, where the leader cells are forming lamellipodia, but also at cell-cell junctions, showing that RhoA-related contractility is responsible for the mechanical forces that exist between cells. This strongly implies that adjacent cells have the propensity to pull on the trailing cells leading up to collective migration.

1.2.3. Cellular density and contact inhibition of locomotion in collective cell migration

Emerging studies have also shown that cellular density within a cell sheet also plays a big role in the regulation of collective migration via contact inhibition of locomotion(58-60). As single migratory cells come into contact with each other, further protrusion along the direction of contact is inhibited, thereby facilitating protrusions in other directions, allowing the cell to change its course of movement in the phenomenon known as contact inhibition of locomotion (Fig. 1.3) (7). However, within a cellular sheet, where cells are constantly attached to each other on all sides, cells can become jammed as they continue to proliferate (52). This jamming induces contact inhibition of locomotion amongst the cells, which drives the leading cells to extend outwards faster, resulting in accelerated collective migration (9). The molecular mechanism behind this are the combinatory activation of rhoA at the site of cell-cell contact, which leads to contractility away from each other, and the activation of rac1 and CDC42 at sites other than the site of cell-cell contact, which leads to lamellipodia formation away from the cell-cell contact.

Furthermore, the activation of rhoA within the cellular sheet has been shown to increase the tension amongst the cells in many simulations. This tension has functions as a glue that keeps cells adhered to each other, which continues to positively feedback into the cell jamming and continue signaling for contact inhibition of locomotion.

1.2.4. Conclusion

Collective migration of cells is essential for many biological processes from wound healing to cancer metastasis. Understanding this complex process in detail will no doubt

help the medical and scientific community treat major wounds or prevent the spread of cancer. In fact, rhoA inhibitors are currently in clinical trials, having demonstrated the ability to prevent cancer proliferation and curb its metastasis in animals. While many discoveries have been made that reconcile our understanding of biomechanics with actual biological phenomena, are still many questions yet to be answered with regards to the mechanical regulations of collective migration. This is made evident in the studies showing the complex and dynamic nature of stresses exerted during collective migration, suggesting that there regulatory mechanisms that are oscillatory in nature that we are yet to be aware of. Furthermore, there is still more questions about the interplay between the leader cells and trailing cells that goes beyond differential regulation in rho and rac. In fact, the influence of contact inhibition of locomotion between the trailing cells and the leading cells seem to suggest that the migratory behavior of the leader cells is a result of signaling amongst the trailing cells themselves. Deciphering this crosstalk will reveal novel ways in which cells are communicating, which will help us find new ways to promote or prohibit the collective migration of cells.

1.3. Study of diffusion into cancer

Cancer cells have the ability grow and form tumors in places that is distant from the systemic circulation, where the transport of nutrients and oxygen into the tumor is primarily dependent on diffusion (61-64). In general, diffusion is considered a highly inefficient way of mass transfer, which points to the ability of cancer cells to survive in hypoxic and glucose deficient conditions (16, 65). This also makes tumors difficult to treat as many anti-cancer agents cannot reach the tumor via the circulatory system at sufficiently

high quantities (21, 61, 62, 66). Emerging studies now show that cancer cells may also express efflux transporters that target these molecules, to allow them actively secrete cytoplasmic anti-cancer agents back into the surroundings, minimizing intracellular damage (67-69). Taken together, this leads to sub-lethal concentrations that ultimately fail to kill the cancer cells entirely. After prolonged exposure to these lowered concentrations, surviving cancer cells gain adaptive immunity to the same drug, rendering further administration of the drug ineffective (19, 20, 70). The patient then must be treated with the next line of cancer drug, which leads to a cycle where patients are given different regiments until either one of them works, or the cancer, which was previously under growth arrest, continues to grow and eventually kill the patient. It is therefore an important consideration during the drug discovery phase to understand the diffusive properties of the drug through tissue, to grant it better accessibility, and therefore higher efficacy. To this end, a multitude of in vitro and in vivo platforms have been developed to better study the ability of drugs to penetrate into cancer tissue.

1.3.1. *in vitro* platforms for studying drug penetration into tumors

In vitro platforms play a big role in the drug discovery process, as the first of many screening steps. For anti-cancer therapeutics, multi-cellular models are often used to model solid tumors in the body (65, 71, 72). Today, the most often used tumor model is the 3-D cancer spheroid, which can be formed from a variety of methods (73, 74). Studies using these have shown that the effective drug concentration of anti-cancer drugs like paclitaxel and cisplatin in spheroids is 100-fold higher than if they were cultured in monolayers. Similar findings were reported for antibodies, siRNA and immunotoxins (75-80). Also,

drug penetration into these spheroids can be measured using the auto-fluorescence of drugs such as doxorubicin (21, 66, 81). However, the integrity of these spheroids often depends on the cancer cells that are used to generate them. Studies have shown that expression of cell-cell adhesion protein, epithelial cadherin, is vital to the maintenance of the structural integrity of the spheroid. As many cancers express this protein in different quantities, not all cancer cells can be used to form spheroids.

Another in vitro platform that is often used to model cancer are multicellular cultures within microfluidic devices (26, 82, 83). By creating pillars that are close together, a sieve can be constructed vertically that prevents cells from passing through them. This allows the fluidics device to trap and pack cells in controlled regions of the microfluidics chip. Media containing drugs can then be flowed tangential to the cell culture, allowing the drugs to diffuse into 3D packed cell culture, which can then be imaged on a microscope to determine the extent of penetration. One advantage of such systems lies in the ability to very precisely control the fluid flowing into the chip, which would allow us to alter the composition of the media temporally to mimic conditions in the body.

Multi-cellular layers are also commonly used to model in vivo cancers. These layers are formed as cells are plated onto a semipermeable membrane mounted onto a tray and grown in a bioreactor (Fig. 1.4a,b) (80). As the cancer cells grow on top of each other, a multi-layer tissue is formed, on which cancer drugs can be tested. Media containing drugs can be put on top of the multi-cellular layer, drugs will diffuse through the layer. These systems, however, cannot be imaged spontaneously in real time, and have to be removed and sectioned in order to examine the extent of drug penetration into this tissue. Tannock and colleagues have used the cell lines, HCT-8Ea, HCT-8E11, HCT-8Ra and HCT-81R1

cells to form these layers (61). Amongst these cell lines, the HCT-8Ra and HCT81R1 cell lines are capable of secreting extracellular matrix into its environment, making it their multi-cellular layers a relatively loosely packed tissue. On the other hand, the HCT-8Ea and HCT-8E11 cell lines do not secrete any extracellular matrix, resulting in a tightly packed tissue. When doxorubicin is allowed to diffuse through these tissues, results show that tightly packed tissues actually prevent the drug from penetrating into the tissue itself (Fig. 1.4c). It is suggested that this resistance to penetration is a result of the cells forming cell-cell junctions via epithelial cadherin coupling, thereby preventing doxorubicin from easily moving through the interstitial space. It is further suggested that tumors formed from cancer cells that do not form these cell-cell junctions are then more susceptible to drug penetration within them.

1.3.2. *in vivo* platforms for quantifying diffusivity

Despite the similarities that in vitro platforms share with in vivo tumors, there are still many places where in vitro platforms fall short. One such example is the vasculature that forms around the cancer is absent in many in vitro platforms. As such, in vivo animal models have also been devised to allow for the study of drug penetration into the tumor. However, once the tumor is implanted into the animal, there are few imaging methods that will allow for continual real-time monitoring of drug penetration (84, 85).

One such method is fasten a piece of glass onto the back of the animal, forming a window chamber. These chambers are often used to study angiogenesis, as the formation of blood vessels can be seen through a conventional microscope. Cancer cells, or tumor tissue can be placed or plated on the glass before it is fastened to the back of the animal,

allowing the cancer to anastomize with the animal. Anti-cancer agents introduced into the systemic circulation of the animal can then be studied as they diffuse through the cancer tissue. In a demonstration by Nugent et al. (86), a time lapse video was obtained, allowing them to estimate the diffusion of the fluorescent molecule, dextran-fluorescein thiocynate, of different molecular weights into a slurry of cancer plated on the glass window. Results here showed that dextran in neoplastic tissue have a diffusion coefficient much closer to that of an aqueous solution in comparison to normal tissue. The authors hypothesized that this could be due to the leaky blood vessels that are attracted to the cancer that causes the interstitium to contain more fluid compared to the normal tissue.

Recently, intravital imaging has also been used to study the penetration of fluorescent molecules deeper within the tissue (87, 88). This method has become a more suitable method to study fluorescence in animals due to its low invasiveness, allowing scientists to preserve the uninjured state of the tumor. It uses low energy infrared radiation that is more penetrating compared to radiation in the visible spectrum. Studies have shown that fluorescence as deep as several mm within animal tissue can be imaged. This has been used in conjunction with xenografts of cancers and fluorescent biomarkers or auto-fluorescent chemotherapeutic agents to study penetration of molecules into tumors.

1.3.3. Conclusion

Diffusivity of drugs into solid tumors remain a key factor in determining the efficacy of the drug. Methods to improve the rate of diffusion of anti-cancer drugs have garnered much attention over the past two decades. Better drug delivery methods have been devised, from the use of lysosomal delivery vehicles, to porous nanoparticles. These

generally improve the rate of diffusion by tackling two key factors: (1) increase affinity of the solute for cancer microenvironment (solvent) and (2) increase the concentration gradient across the tumor (17). However, despite the emergence of these methods, there are still a lack of application of these models in drug discovery.

1.4. Organ-on-a-chip systems

Over the past decade, organ-on-a-chip microphysiological systems have garnered much attention for their ability to recreate the higher level functions of tissues and organs outside of the human body (22, 89-91). Such devices will eventually be able to serve as a testing platform for drug discovery and development, replacing animal models as they are more predictive of how humans will respond to compounds, are less labor intensive and can potentially bring about faster results, thereby reducing the time it takes for drugs to make it to market (23, 25, 28, 90). To date, many different organ-on-a-chip systems have been developed for different organs, from some of the main organs such as the lung, liver, heart to more peripheral organs such as the placenta (22, 24, 92). In the fabrication of these devices, some groups have incorporated cells differentiated from induced pluripotent stem cells, which contain the genomic data of the donor (92, 93). Studies have shown that cells obtained from patients suffering from genetic disorders continue to exhibit these traits in the cells in the chip, allowing scientists to build disease models to better understand how such diseases develop, and how they can be treated.

However, despite the rise in attention and expertise that has developed in the field, there are only a handful of studies that have attempted to combine multiple organ-on-a-chip systems into a wholly integrated system that can not only recapitulate organ-organ

cross talk but also recreate the whole human physiologies outside of the human body. Here in this subchapter, I will highlight some landmark studies that contributed to the development of organ-on-a-chip systems, as well as a few other integrated multiple organ devices that have been developed so far.

1.4.1. Lung-on-a-chip system

As an organ, the lung is composed of many small alveolar sacs that allow oxygen to passively diffuse from the atmosphere into the blood and carbon dioxide to diffuse from the blood into the atmosphere. Cellularly, it is composed of lung epithelial cells attached to the inner wall of the alveolar sacs and endothelial cells attached to the outer wall of the alveolar sac. These cells are separated by a thin basement membrane that constitutes the acellular component of the alveolar wall. As the diaphragm at the base of the lung contracts, negative pressure in the thoraxic cavity pulls on the lung, leading to expansion of these alveolar sacs, and therefore the stretching of the cells. There have been several lung-on-a-chip devices created, all of varying complexities. Some of the more well established ones will be covered here.

In one pioneering experiment, Huh et al had created a bilayer microfluidic device capable of reconstituting organ-level function (22). In this device, the authors had created a silicone substrate with a cuboidal chamber divided horizontally by a porous silicone membrane into a top chamber and a bottom chamber. The top layer of the porous membrane was seeded with epithelial cells and the bottom layer was seeded with endothelial cells. Air was passed through the space above the epithelial cells while media containing nutrients was flowed through the space under the endothelial cells, much like in the lung.

Furthermore, isolated air channels were fabricated parallel to this chamber, to which a pneumatic pump was attached to that regulated the air pressure within. Specifically, when air was pumped out of these channels, the negative pressure in them would lead to stretching in the silicone membrane that transduced a strain to the cells attached on it (Fig. 1.6). To recreate physiological conditions, this stretch was optimized to exert an oscillatory strain of 10% at a rate of 0.2Hz to the membrane much like in the human body. Results from this experiment also showed the important role of this oscillatory stretch on cellular behavior. In the absence of the oscillatory stretch, the proinflammatory responses of the epithelial cells to silica nano particles were attenuated. The authors went onto see if they could induce an immune response in the system by first injecting bacteria into the epithelial chamber. Immune cells were flowed in together with the media in the underlying chamber. Results showed that in the presence of bacteria, the immune cells were able to attach to the underlying endothelial layer transmigrate across it and cross the porous membrane to the epithelial layer to combat the bacteria. In a follow up study, Huh et al. continued to demonstrate the propensity of this device to model diseases by creating a pulmonary edema model on this chip (94).

Since this invention, others have taken this proof-of-concept further. In a study by Stucki et al., the lung on a chip system was scaled up into an array that would be more applicable as a drug testing platform (95) (ref). Others have created new disease models via protein-induced inflammation within other similarly designed lung-on-a-chip devices (96) (ref).

1.4.2. Heart-on-a-chip systems

The heart is the workhorse of the systemic circulation, and through rapid and periodic contractions, it is able to pump the blood from its cavities to the rest of the body. One of the difficulties encountered when trying to design heart-on-a-chip systems is the lack of spontaneously beating human cell sources; there are still no methods that can be employed to make an adult cardiomyocyte beat spontaneously. As such, researchers often have to rely on to neonatal mice cardiomyocytes or human iPSC-derived cardiomyocytes, both of which have been demonstrated to beat spontaneously but are difficult to obtain, for a cell source to conduct their studies. As such, there are still few published designs for modern heart-on-a-chip systems, some of which will be covered in detail here.

In a study by Grosberg et al., neonatal rat cardiomyocytes were infused into a device containing thin long flaps of silicone (97). These cardiomyocytes self-assembled into a sheet parallel to the flaps, forming cell-cell junctions that allow for membrane potentials to be transduced across them. This is important as these membrane potentials can be transferred across cells in the sheet, allowing them to beat in synchrony. The forces exerted by these cardiac flaps can be characterized by studying the deflection in the flap by assuming cantilever mechanics (Fig. 1.7). Agarwal et al. has continued the study of these heart-on-a-chip device by testing the effect of molecules such as isoproterenol on the contractility of the cardiac flaps (98). Recently, a study conducted by Wang et al. demonstrated in the proof-of-concept study that the mitochondrial cardiomyopathy of Barth syndrome can be recapitulated in the heart-on-a-chip device using induce pluripotent stem cells (93).

More recently, studies are trying to move away from these monolayer cultures to build multi-layer tissues. One study by Healy and colleagues (99) used a chamber that is surrounded on all sides by channels that are too narrow for cells to penetrate, creating a cellular sieve within a microfluidic device. As cells are injected into this chamber, the media carrying them leaves the chamber through these sieves, filtering the cardiomyoctes within the chamber, which over time packs and self-organizes into a tissue. Fresh media is fed through the channels beyond the sieve, and the nutrients enter the diffuse by passive diffusion. This system was then tested against four different molecules, isoproterenol, verapamil, metoprolol and E4031, with the results showing consistency with human adult heart tissue.

Another approach by Aung et al was designed to measure the stresses generated by a 3D heart-on-a-chip tissue (100). This heart-on-a-chip device was made by resuspending neonatal mice cardiomyocytes in photopolymerizable hydrogel precursor solution made from gelatin. A photomask was used to filter light in specific geometries to create hydrogels of different shapes that encapsulated the cells inside. In doing so, the hydrogel substrate was then sandwiched in between thin layers of fluorescent-bead embedded polyacrylamide hydrogels substrates. Upon maturity, the spontaneous beating of the neonatal mice cardiomyocytes tugged at the underlying substrate, causing a deflection in the embedded fluorescent beads. This then allowed for the determination of the stresses exerted by the cardiomyocytes on its surrounding substrate using the principles of traction force microscopy.

1.4.3. Liver-on-a-chip systems

The liver is one of the largest organs in the body, and plays diverse metabolic roles crucial to homeostasis and survival. A non-exhaustive list includes the production of serum albumin to maintain the osmolarity of blood plasma, secretion of factors used in the blood clotting cascade to allow for recovery from injury, to metabolism of drugs and toxins in blood to prepare them for excretion from the body (101-103). Due to this, good in vitro liver models are highly sought after in the pharmaceutical industry for the study of the metabolism of many of its compounds. However, many conventional models have been utilized in limited applications due to their many drawbacks: Explant cultures can only be kept viable for short periods of time, while human hepatocytes are rare, expensive and cannot be expanded in vitro (101, 102). Liver-on-a-chip models that seek to miniaturize cultures in highly controlled environments have the potential to overcome these drawbacks. Additionally, advancements in biofabrication have made it possible to recapitulate the complex microenvironments that physically and biologically resemble human liver tissue (104, 105). Recent experiments have not only demonstrated long term viability of these platforms, but also, through the incorporation of the various cell types that are found natively in the liver, demonstrated their ability to simulate in vivo liver physiology and recapitulate many of the liver's functions (106, 107). Due to its relative importance amongst the organs, there have been quite a handful of groups that have worked on establishing their liver-on-a-chip model. Several of them are described in brief here.

Studies by Dash et al. have even shown the importance of flow in these devices, wherein hepatocytes kept in continuous flow systems exhibit an enhanced capacity to

metabolize substrates for several cytochrome P450 enzymes and the ability to transport the metabolites into the bile canaliculi (108).

In another instance, Lee et al. has tapped the potential of micro-biofabrication to create artificial liver sinusoids with a microfluidic endothelial barrier, and discovered that through cellular self-assembly, the micro tissue grown in the chip possesses mass transport properties similar to the acinus structure in the liver (109).

However, one of the biggest problems lie in the lack of suitable cell sources for hepatocytes for use in these devices. To this end, Bhatia and colleagues have devised a protocol to differentiate iPSC-derived spheroids into hepatocytes, and incorporate those into a microfluidic device (Fig. 1.8) (92). This continuing improvement in micro-fabrication technology, derivation protocols from stem cell based sources and understanding on a fundamental level of how cell-cell communication can promote overall functionality of the tissue assembled will lead to the generation of reliable liver-on-a-chip platforms for use in various drug testing applications.

1.4.4. Gut-on-a-chip systems

The gastrointestinal tract serves the important role of separating food that we consume and our body's circulatory system, carefully gating the molecules that are allowed to pass while rejecting those that are not. While there is only one type of epithelial cell that lines the insides of our intestines, they are differentiated into specialized cells with different functions, such as a proliferative basal layer of cells, mucus secreting cells, absorptive and endocrine functions. The one function of these cells combined regulate the transport of essential nutrients into our body while rejecting those that can be harmful. This is done via

the expression of influx and efflux channels on their cell surfaces allows molecules to be transported through the cells themselves. Once these compounds permeate through the epithelial layer, they can then diffuse into blood vessels through another endothelial layer, and into the systemic circulation. There have been a several studies that have designed a gut-on-a-chip system, and they are covered in depth here.

In one gut-on-a-chip developed by Kim et al, a design similar to their previous lung-on-a-chip system was used, where a two-chamber system was fabricated and separated horizontally by a porous silicone membrane (110). A human epithelial cell line, Caco-2, was used to line the top surface of the membrane and media is passed through both sides, the fluid in the epithelial layer chamber simulates nutrients from food ingested, while the fluid in the bottom simulates the blood. Upon application of both the mechanical stretch and the fluid flow, it was observed that the Caco-2 cells began expressing 4 different phenotypes found in the gut: absorptive, mucus-secretory, enteroendocrine and Paneth. They also began to form 3-D structures that resemble the basal proliferative crypt and the protrusive microvilli (Fig. 1.9) (110). On top of that, a further study demonstrated their capability to maintain the viability of intestinal microbe (Lactobacilius rhamnosus GG) without negatively affecting the epithelial cells. It was also observed that the barrier function of the epithelial layer improved with the bacteria growing with the epithelial cells. Such results have never been observed amongst other in vitro gut-models, suggesting the importance of mechanical signaling (from both the periodic stretching of the membrane and the shear stress provided by the tangential flow) on differentiation of epithelial cell types.

In another study by Esch et al., the barrier function of a gut-on-a-chip was explored using a Caco-2 cell sheet (111). Nanoparticles suspended in media were flowed across the gut-on-a-chip platform and allowed to penetrate the monolayer. Results from this experiment showed that only 9.5% of all the nanoparticles were able to penetrate this Caco-2 layer, and was upon reaching other organ-on-a-chip systems integrated with the basal fluid flow through of the Caco-2 cells, was able to demonstrate toxicity in the liver-on-a-chip platform. Specifically, HepG2 cells in the liver-on-a-chip compartment of the device released aspartate amino transferase (AST) upon exposure to the nanoparticles, indicating liver cell injury.

1.4.5. Kidney-on-a-chip systems

Another organ-on-a-chip system that has garnered much attention for potential applications in the pharmaceutical industry is the kidney-on-a-chip system (112). One of the main functions of the kidney in vivo is to filter out undesirable compounds from blood. In the body, blood enters the kidney where unwanted compounds in blood can be actively or passively removed from blood plasma and into urine, which is then stored until it can be removed from the body. These compounds have to permeate the endothelial cell wall lining the capillaries, as well as the epithelial lining in the tubules of the nephron. There have been a handful of designs for the kidney-on-a-chip system. Some studies that have been key milestones to this development is highlighted here (113).

In one study, Jang et al fabricated a PDMS device consisting of a cuboidal top and bottom chamber separated horizontally by a porous membrane (23). By utilizing human primary kidney cells plated above the membrane, the separation between the epithelial

lining and the interstitial space is then established. This became a model against which the authors tested the chemotherapy drug, cisplatin on. Results from the experiment demonstrated that the flow above the epithelial layer was able to "rescue" more of the epithelial cells in comparison to the static culture. The authors hypothesized that this could be due to the shear flow contributing to inhibition of apoptosis amongst the epithelial cells.

In another study, Mu et al created 3D tubular networks from kidney epithelial cells amid endothelial vessels by culturing them in sodium alginate, thereby recapitulating the nephron tubes and accompanying blood vessels (114). However, despite the formation of physiologically similar structures, many of the tubules are yet to function.

1.4.6. Integrated multiple organ-on-a-chip systems

The integration of multiple organ-on-a-chip systems has long been considered the goal of these studies. However, one of the biggest problems faced in this integration process is the formulation of culture conditions that can cohesively maintain both the viability and the phenotype of the cells that are within the integrated chips. To date, there has been a handful of proof-of-concept studies, each with several different organ-on-a-chip systems, that not only demonstrate viability and function in each organ system, but also organ-organ cross talk that is essentially one of the main functions of an integrated organ-on-a-chip system.

In an earlier study, Shuler and colleagues fabricated a microfluidic device that allowed for the culture of 3 different cell lines derived from three separate tissues, including cancerous tissue: HepG2/C3A hepatocarcinoma cells from the liver, HCT-116 colon carcinoma cells from colon cancer and kasumi-1 myeloid leukemia cells from the bone

marrow (Fig 1.10) (115). Reservoirs were connected on both sides of this cell culture, and placed on a rocking device such that culture media will flow from one reservoir into the other and back. One key finding of this study was how tissues culture in this manner can interact with each other via the media that they share. In this example, the cancer prodrug tegafur was placed into the reservoir, which can be metabolized by hepatocytes in the liver into its active form, 5-fluorouracil. Results have shown that the presence of a liver culture accelerates the killing of the cancer cells cultures, lowering the viability from 0.9 in 48 hours to 0.65 in 48 hours in the presence of the liver cells. Additionally, off-target sides effects could be seen in the bone marrow cell culture in the same chip.

In another demonstration of integrating multiple organs into one device, Yu and colleagues have put together a device that connects the lung in series with the liver, kidney and fat cells, which are connected in parallel (116). A549 adenocarcinomic epithelial cells were used to represent the lung, C3A hepatocarcinoma cells were used to represent the liver, HK2 transformed kidney epithelial cells to represent the kidney and the HPA adenoma cells to represent fat tissue. To create each tissue, the respective cells were packed tightly into each chamber, forming cell masses. Media is perfused around each tissue, which then allows nutrients to diffuse into the cell mass. Additionally, when transforming growth factor β was added to the circulating media, the viability of many of the tissues declined in response.

Apart from creating one chip with multiple organs, Healy and colleagues demonstrated the use of modular devices, where in different organs can be made and then joined together in series to create integrated organ-on-a-chip devices (27). In this study, cardiac chips that were designed in a separate study were linked together in series to allow

the same media to perfuse them. Results from here demonstrated continued viability over 2 days, with the cardiac cells continuing to beat over this same period.

1.5. Figures

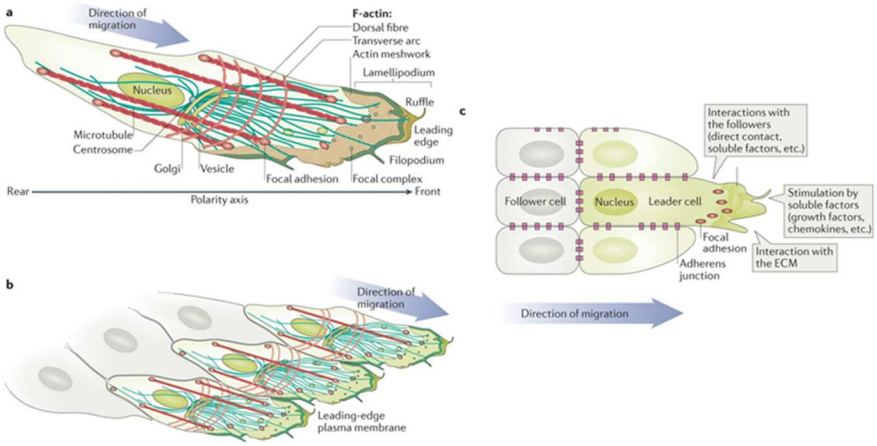

Figure 1.1: Molecular principles involved in collective invasion.

(a) During single-cell migration, the main engine for movement seems to be at the front of the cell, where active membrane protrusion occurs and the cell adheres to the extracellular matrix (ECM). As the lamellipodium extends, integrin-based nascent adhesions form; these eventually mature in focal adhesions, on which longitudinal acto-myosin cables are anchored. Mature focal adhesions are maintained during migration, until they reach the retracting edge of the cells, where they are disassembled. For clarity, only a few nascent and mature adhesions are shown. Locomotive forces applied to focal adhesions drive movement of the cell on or through the substratum. Although events at the cell leading edge provide essential forces for forward movement, the cell rear also actively participates in cell displacement by controlling detachment from the ECM and contraction of the cell body. The microtubule network and components of the intracellular membrane also organize in a polarized manner along the direction of migration. (b) Reflecting this front–rear orientation, leader cells are clearly polarized: they show an elongated morphology, polarized along the direction of migration. However, observations in vitro show that some wound-edge mammalian epithelial cells elongate more than others, and some epithelial leader cells can spread perpendicularly to the direction of migration. The increased spreading of leader cells associated with a mesenchymal phenotype reflects a transient loss or reorientation of epithelial baso-apical polarity in favor of a front–rear polarity. Leaders retain some epithelial characteristics and remain attached to their neighbours and often display dynamic actin-based protrusive structures. Although not limited to leader cells, finger-like filopodia and ruffling lamellipodia form at the front edge of the epithelial monolayer. The morphology of leader cells is associated with the expression of specific genes that promote cytoskeleton remodelling and cell migration. (c) In a cohesive cell group, the leader cells are subjected to polarized environmental cues. While the cell rear is engaged in intercellular contacts, the cell front interacts with the ECM or with non-migrating cells of the tissue. Adherens junctions restrict the localization of focal adhesions to the cell front, by locally inhibiting their formation and maintenance. F-actin, filamentous actin. Reproduced from (7).

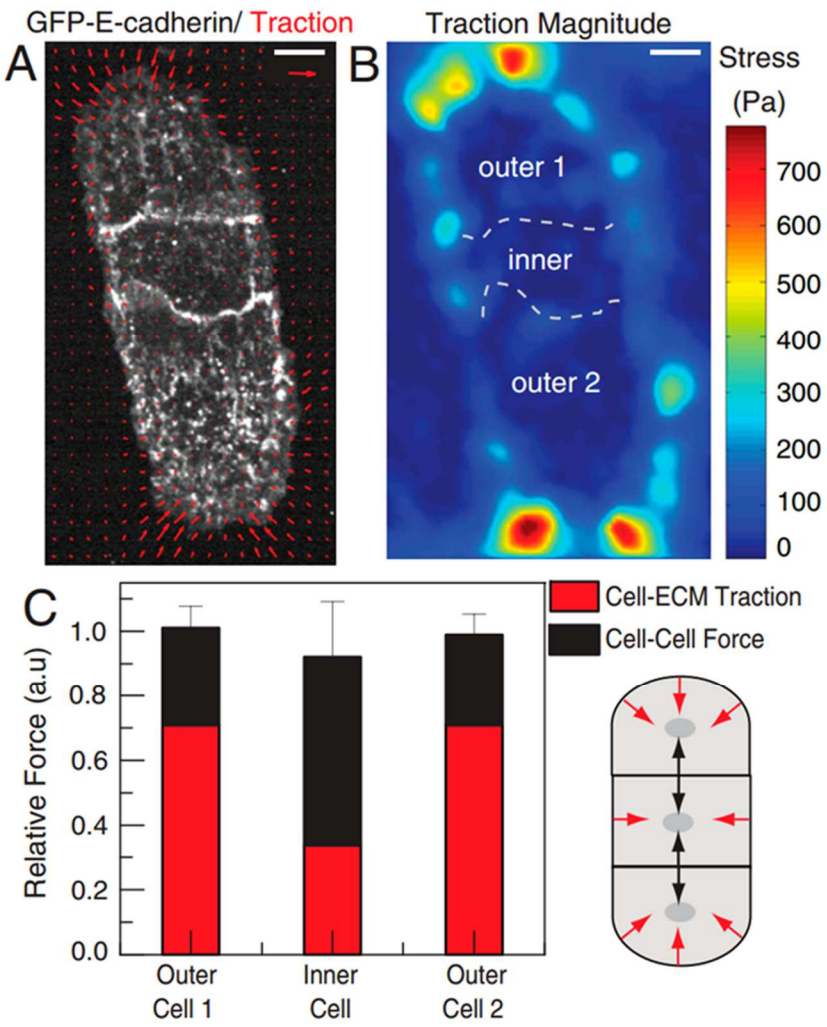

Figure 1.2: Total forces exerted on the microenvironment by individual cells in a linear three-cell island are similar.

(A) Traction stresses exerted by a linear three-cell island of MDCK cells expressing GFP-E-cadherin. Traction stress vectors are overlaid (red arrows). Reference traction vector is 1,000 Pa; scale bar indicates 10 μm. (B) Heat-scale map of the traction magnitude for the cell island shown in A. Dashed white line indicates cell–cell contacts. The three cells are indicated by text. (C) Relative total cell-ECM traction force (red) and cell–cell force (black) exerted by the three cells shown in A. Values are relative to the average between the total forces exerted by the outer cells. Schematic on the right depicts the three-cell configuration and the cell-ECM (red arrows) and cell–cell (black arrows) forces exerted by each cell. Data reflect the mean and standard deviation for n ¼ 4 cell islands with identical geometry. Reproduced from (117).

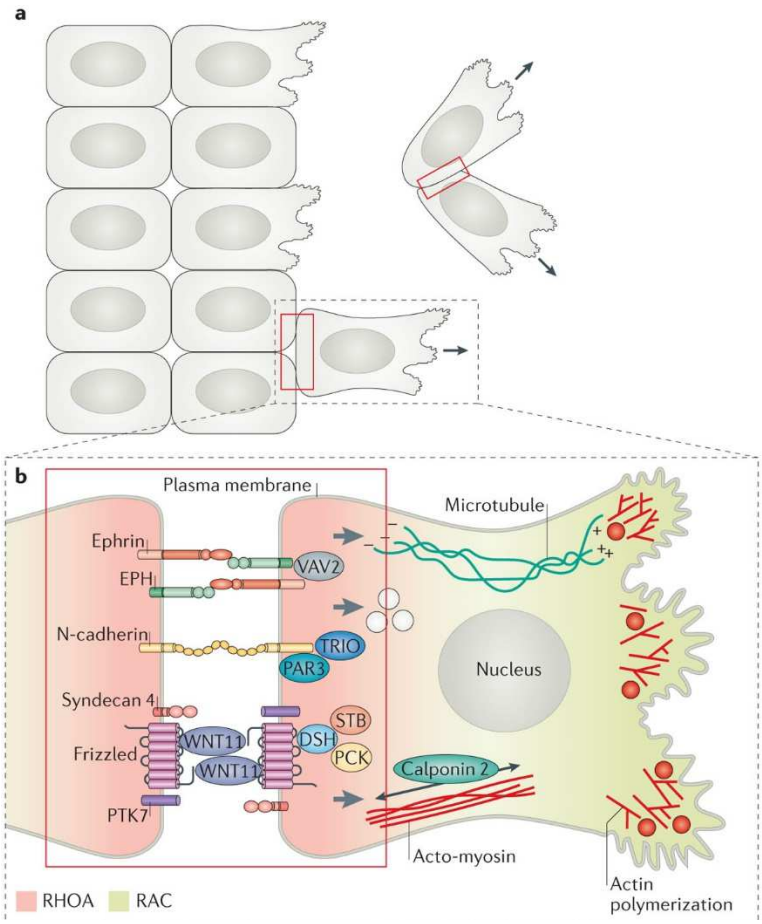

Figure 1.3: Mechanism of contact inhibition of locomotion

(a) CIL is the process by which a cell changes its direction of migration upon collision with another cell (top right), which leads to cell polarization, with protrusion formation being inhibited at the cell contact and a new protrusion being produced away from the contact. If cell density increases, a similar phenomenon of inhibition of protrusion formation at the cell contact takes place, but on a larger scale, such that only the cells that are exposed to the free edge become polarized and produce protrusions away from the cluster (left). Cell contact during CIL is indicated by a red square. (b) | Cell surface molecules interact at the site of cell–cell contact (red square), which leads to the recruitment of several other proteins and, finally, to RHOA activation and RAC inhibition at the contact. This is translated into microtubule catastrophe, disassembly of focal adhesions (white circles) and actomyosin contractility at the contact, leading to the collapse of protrusions. At the opposite end of the cell, activation of RAC leads to microtubule and microfilament polymerization and stabilization of focal adhesions (red circles), with the consequent formation of protrusions. DSH, Disheveled; EPH, ephrin receptor; PAR3, partitioning defective 3; PCK, Prickled; STB, Strabismus; TRIO, triple functional domain protein. Reproduced from (7).

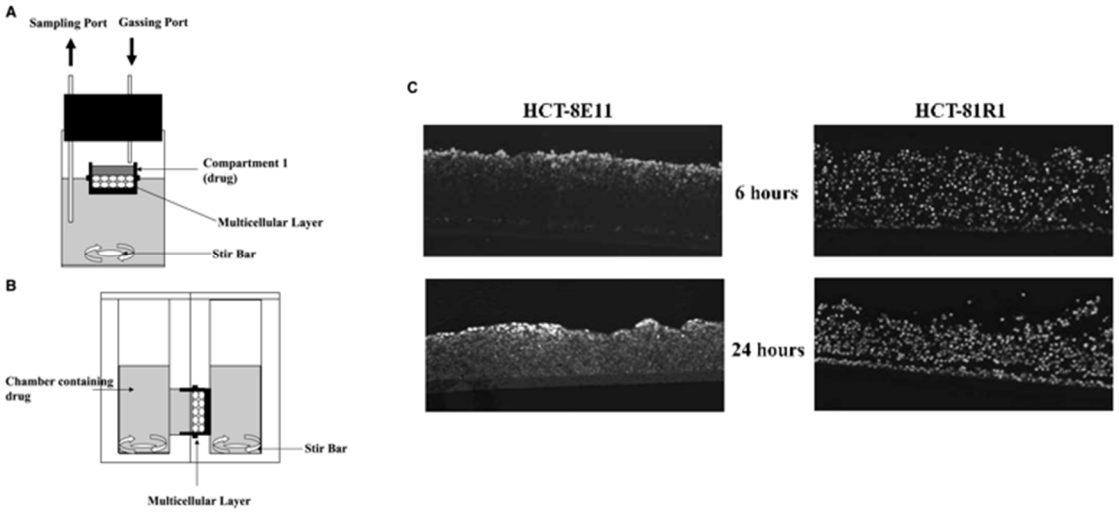

Figure 1.4: Assessment of drug penetration through a MCL

(A) the experimental chamber used to assess drug penetration through a MCL. Anticancer agents dissolved in 1% agar (to prevent convection) are added to compartment 1 and the insert containing the drug and MCL is then floated in media. Samples are obtained from compartment 2 through the sampling port while the gas port delivers a mixture of 95% air and 5% CO2. (B) the dual chamber model avoids the use of agar and facilitates the disaggregation of cells in a MCL. In this system, drug at selected concentrations was dissolved in media in the chamber adjacent to the MCL. (C) Penetration of doxorubicin through MCLs derived from E11 and 1R1 sublines after 6 and 24 hours. Doxorubicin penetration is slower through MCLs derived from the tightly packed E11 cell line with distribution of the drug largely in the proximal layers. Similar patterns were observed using Ea and Ra sublines although, at 24 hours posttreatment, less MCL disaggregation was observed for these cell lines than for the E11 and 1R1 subtypes. Reproduced from (61).

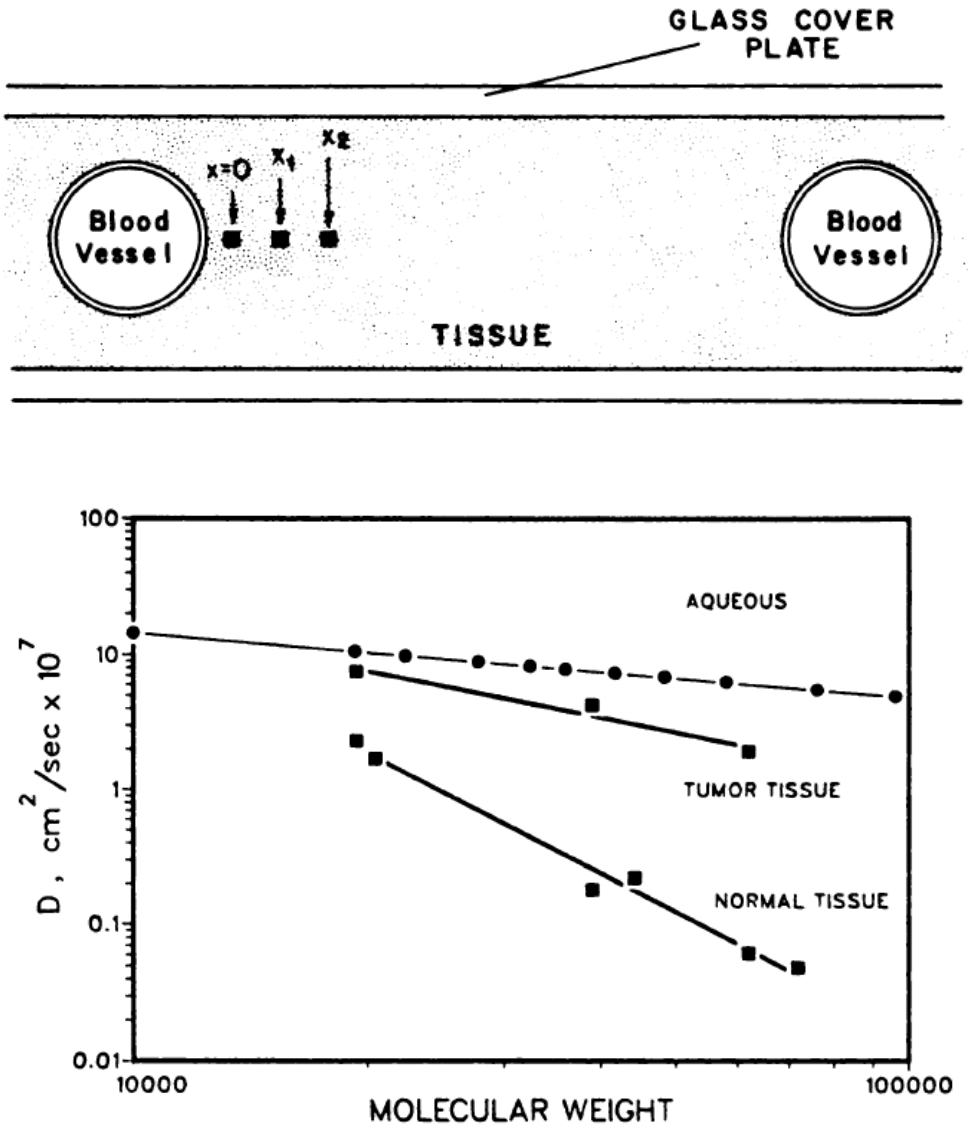

Figure 1.5: Determination of the interstitial diffusion coefficient of dextran molecules of different molecular weight

(top) Chamber design showing two blood vessels and the tissue in between them sandwiched by a glass plate. Concentrations of fluorescent molecules were measured at different points between the two blood vessels. The number of poins measured ranged from 3-6 depending on the intercapillary distance. (bottom) Dependence of the diffusion coefficient on the molecular weight of dextran used. Upper curve represents the diffusion coefficient in an aqueous solution. The middle and bottom curves represents the diffusion coefficient in neoplastic and normal tissue respectively. Reproduced from (86).

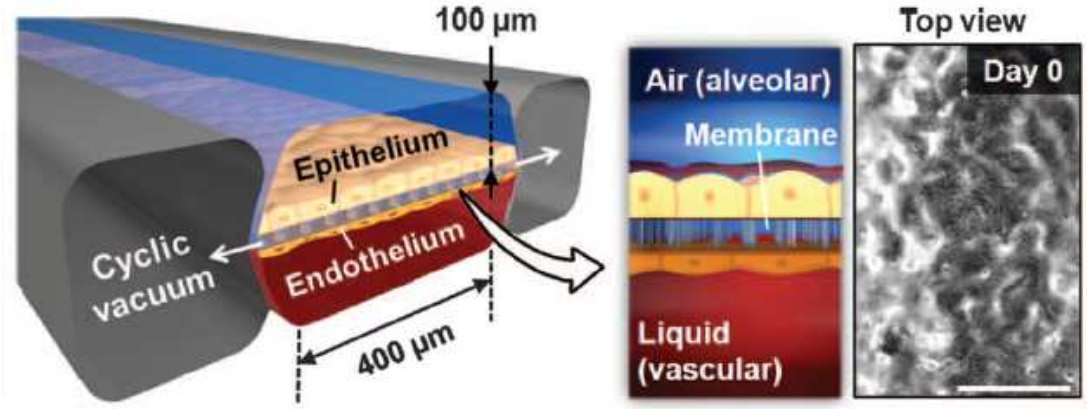

Figure 1.6: Schematic of the lung-on-a-chip

The schematic describes a lung-on-a-chip device that reproduces the lung microarchitecture and breathing-induced cyclic mechanical distortion of the alveolar-capillary interface. The top **"**air**"** portion is the alveolar channel; the bottom **"**liquid**"** portion is the vascular channel. Cyclic vacuum is used to stretch the membrane on which the epithelium and endothelium sheets are cultured. The phase-contrast image shows a top-down view of the apical surface of the alveolar epithelium maintained at an air-liquid interface in the upper microchannel. Scale bar, 200 mm. reproduced from (94).

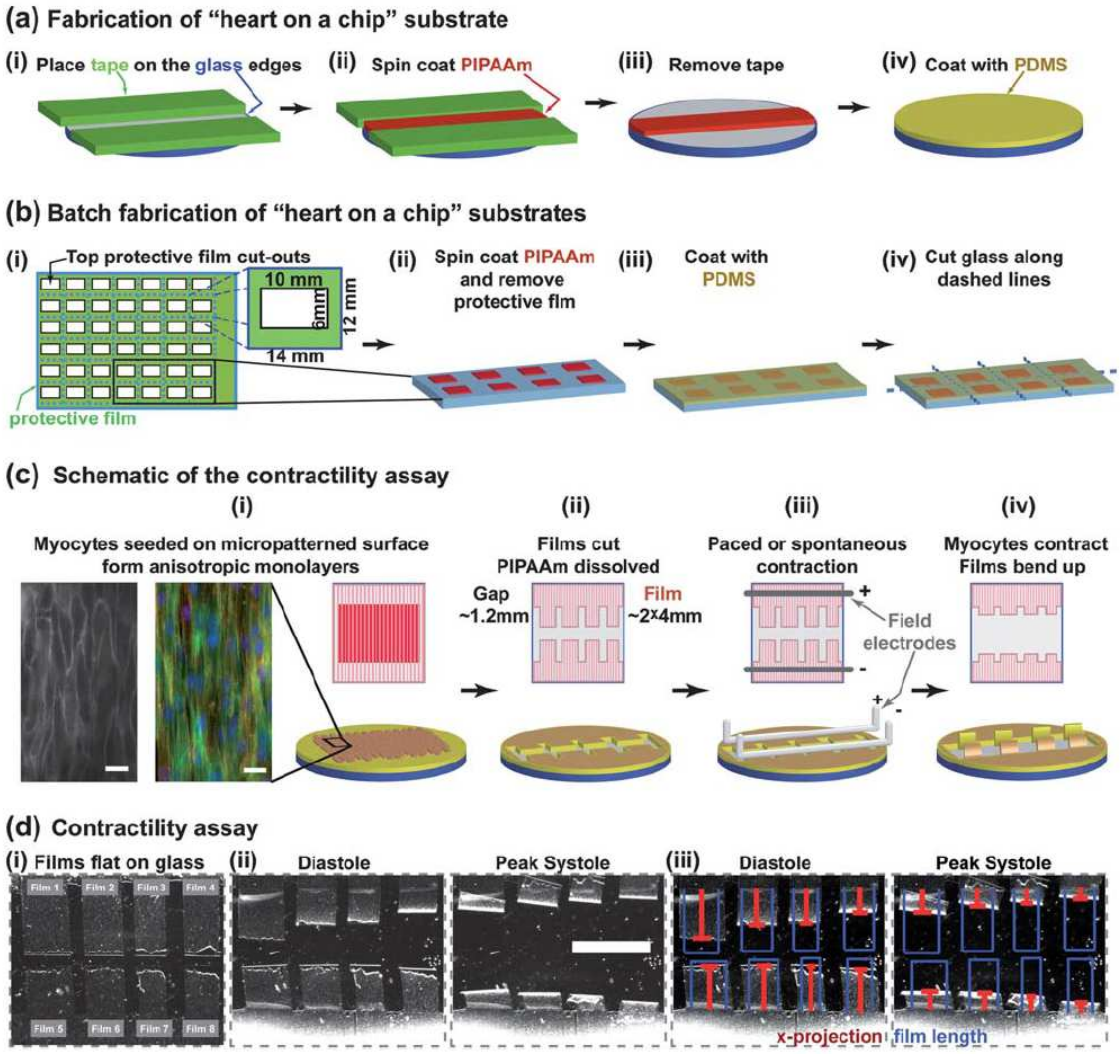

Figure 1.7: Fabrication of cardiac flaps and corresponding contractility assay

(a) Fabrication of 25 mm round substrates; (b) schematic representation of batch fabrication of substrates with large glass sections for higher throughput; (c) contractility assay is run using anisotropic layers of myocytes; bottom row shows a 3D schematic representation, top row shows the view from above; the insets in (i): RH237 membrane dye stain (left) and an immunostain of a-actinin – red, actin – green, nuclei – blue (right), scale bar 20 mm; (d) Contractility experiment (PDMS layer . 18.6 mm): (i) Brightfield images of films attached to the substrate, (ii) films bend up at diastole and peak systole, and (iii) the length of films (blue) and x-projection (red) overlaid on ‘‘heart on a chip’’ images – scale bar 5 mm. reproduced from (97).

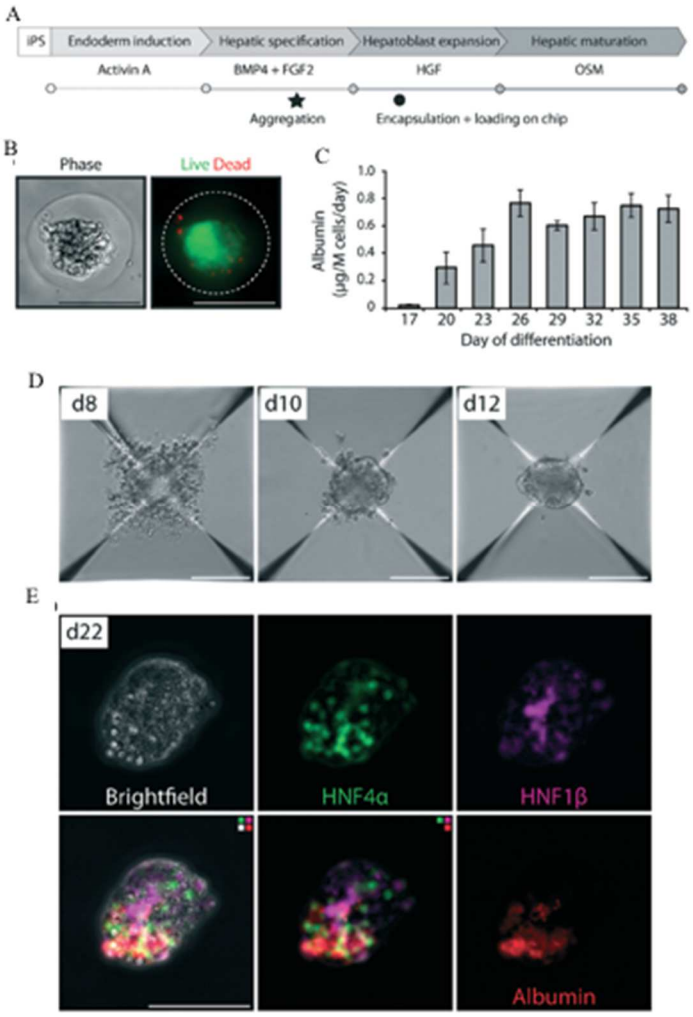

Figure 1.8: Differentiation of iPSC derived hepatic spheroids for liver-on-a-chip studies.

(A) Hepatocyte differentiation protocol. After dissociation and aggregation at day 8, iHep aggregates were encapsulated into PEG-DA hydrogels and trapped in a microfluidic device at day 12 of differentiation. (B) Encapsulated iHep aggregates were viable as shown by calcein AM (green; live) and propidium iodide (red; dead). (C) Encapsulated iPS derived hepatic microtissues show long term albumin secretion on-chip. Values represent average albumin secretion per day of three different devices, normalized tothe amount of cells. Number of cells was estimated based on the number of cells seeded in aggrewells on day 8. Error bars represent standard deviation. Scale bars represent 100 **µ**m. (D–E) When dissociated at day 8, hepatic specified iPS cells form compact aggregates in 400 µm aggrewells. (E) Aggregates at day 22 of differentiation express markers specific for hepatocytes (HNF4α, albumin) and for bile duct cells (HNF1β). Scale bars in D and E represent 100 µm. Reproduced from (92).

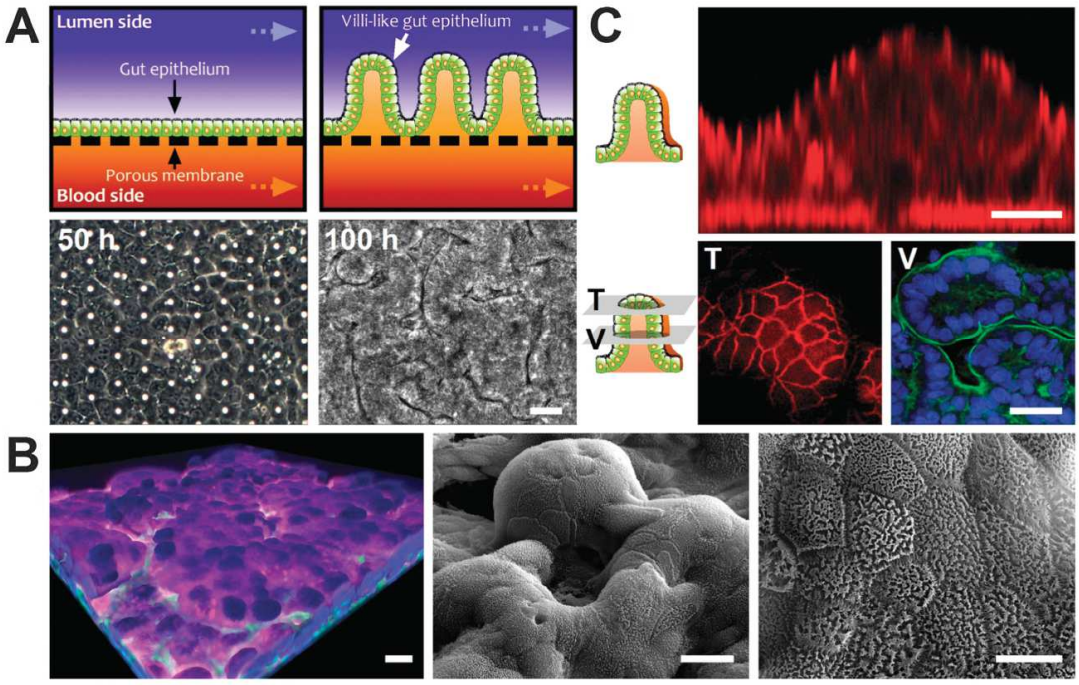

Figure 1.9: Formation of microvilli structures from a Caco-2 cellular monolayer in a gut-on-a-chip microfluidics device.

(A) Schematic showing transformation of a planar intestinal epithelium into villus structure (top) and corresponding phase contrast images of Caco-2 cells that undergo similar villus morphogenesis recorded at 50 and 100 h (bottom). (B) A 3D reconstruction of **Z**-stacked images of Caco-2 villi stained for nuclei (blue), F-actin (green), and mucin 2 (magenta) is shown at the left. SEM images of these villi are shown at the middle and right at low and high magnification, respectively. (C) Schematics showing a vertical cross section and horizontal cross sections at the tip (T) versus middle (V) of a single villus are shown at the left. Immunofluorescence confocal views of Caco-2 villi shown at the right demonstrate staining for the tight junction protein, ZO-1 (red) in vertical (top) versus horizontal **en face** sections of a Caco-2 villus (bottom left). Bottom right view shows staining for the continuous apical brush border membrane labeled for F-actin (green) overlying the well oriented intestinal cell nuclei (blue). All scale bars are 25 mm, except right SEM image (bar, 10 mm). reproduced from (110).

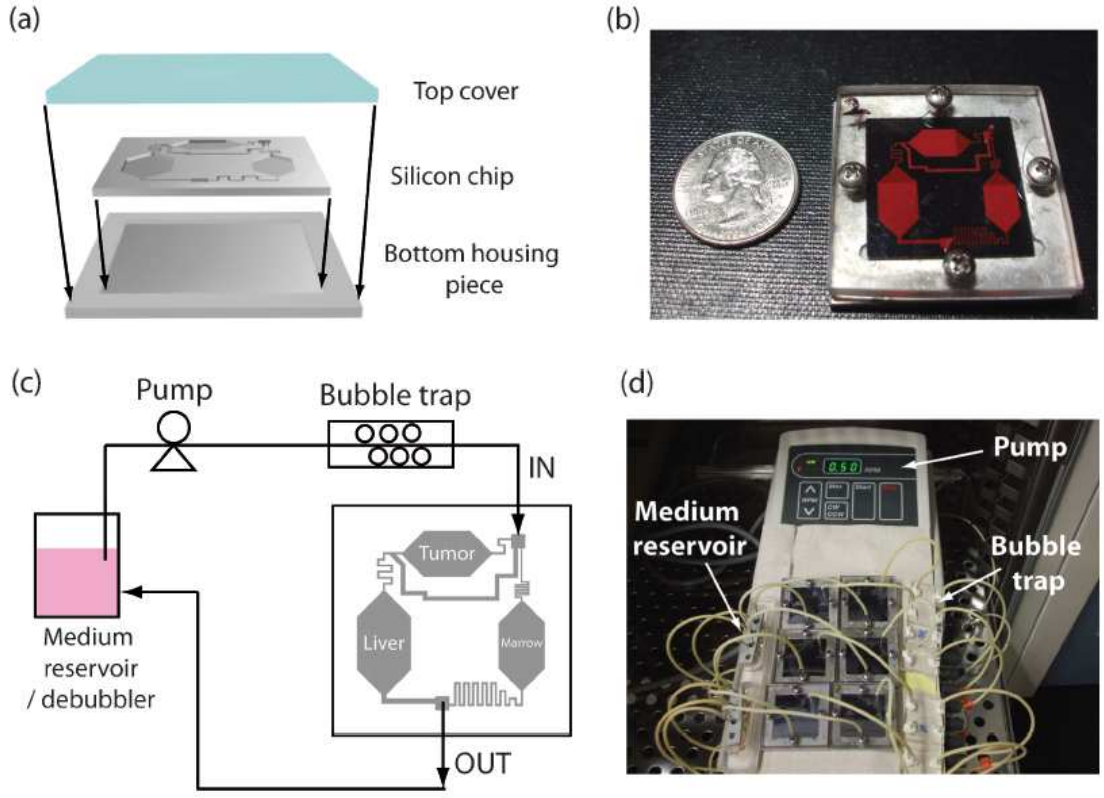

Figure 10: Schematic and Assembly of integrated organ-on-chip device

(a) Schematic diagram showing how the mCCA is assembled. The silicon mCCA chip with features on top is sandwiched between the plastic top cover and an aluminium bottom housing with a recess. The sealing is secured by screws around the edges of the housing. (b) A picture of an assembled mCCA with red dye for visualization of channels and chambers. (c) Schematic diagram of operation setup of a single mCCA with medium recirculation. Medium is withdrawn from a reservoir, which also functions as a debubbler, and goes through a bubble trap for further prevention of bubble trappinginside a mCCA. After circulating through the channels and chambers in a mCCA, medium goes back to the reservoir for recirculation. (d) Picture of themCCA system with multiple chips. Reproduced from (115)

Chapter 2: Alternating Control and Dynamic Malleability in Cell Pairs

2.1. Abstract

Studies have long suggested that individual cells within a collective use mechanical stresses to signal amongst each other. However, the interplay between forces and cellular behavior remains largely unknown. To better understand the effects of mechanical communication on cellular behavior, we developed an integrated approach involving traction force and intra- and inter- cellular stresses between the cells undergoing a collective migration. Specifically, we have studied single-file migration of a pair of cells attached front-to-back. Our results show that the role of the leading cell alternates between the two cells, as the pair migrates along the direction of the leading cell. We have also observed cooperativity between the two cells in which the trailing cell mechanically softens itself to allow the leading cell to pull it along. Together, our method demonstrated how two cells can be engaged in a mechanical "tug-of-war" where trailing cells actively adjust their mechanical malleability to facilitate the subtle movements of the cell pair.

2.2. Introduction

Traction and cellular (intra- and inter-) stresses play key roles in collective migration. Unlike traction stresses, which is generated at the outer periphery of the migrating group of cells, cellular stresses form within and between cells where they function as a mechanical "adhesive" to maintain cellular interactions and ensure that the

group moves cohesively (13, 14, 53, 118, 119). Emerging studies suggest that cellular stresses may also serve as an alternative form of communication between individual cells in the group, allowing cells to signal between one another and forge a synergistic relationship that coordinates or facilitates collective migration (120-123). Despite its importance, it has been challenging to study the stresses exerted by each cell within a group, as collective migration tends to manifest in large groups of cells and in the presence of external physical (e.g., free space (124, 125), cellular geometry (126, 127) and/or substrate rigidity (128)) or biochemical cues (e.g., growth factors (5) and serum (52)), which tend to overshadow the influence of intercellular mechanical signaling (8). Herein, we study the pairwise mechanical communication between cells without any interference from neighboring cells or extracellular morphogenic gradients by using one-dimensional migration of two conjoined cells—the smallest possible group of cells that displays the hallmarks of collective migration.

Our approach involves imaging and quantitatively analyzing the behavior of two human umbilical vein endothelial cells (HUVECs) attached front-to-end undergoing unbiased migration within a geometrically confined space by using a micro-patterned hydrogel substrate (Fig. 2.1). This choice of cell line was dictated by their ability to undergo collective migration in both 2D and 3D, and their long spindle-shaped morphology when spread, which enables them to generate large, measurable traction stresses. The hydrogels were prepared from an acrylamide monomer solution containing fluorescent beads, and patterned with laminin lines on its surface by adapting established protocols (129, 130). These protein line patterns served as “railings” for the cells, facilitating their migration in

a single direction, which greatly simplified our subsequent analyses. The cells were transduced to express mCherry fluorophores for better visualization and imaging, and were seeded on top of the hydrogel. Within hours, the cells adhered to the patterned surfaces and proximal cells attached to each other via vasoendothelial cadherins (Fig. 2.2). Pairs of cells that were attached to each other, referred to as "cell trains", were imaged using time-lapse confocal microscopy at a rate of 1 image every 2 mins. The time-lapse image stacks were imported into MATLAB and analyzed to identify the outlines of the cell trains, which were then used for building kymographs of cell movement as a function of time (Fig. 2.3). Simultaneously, we also acquired images of the fluorescent beads and used particle image velocimetry to map out the displacement (deformation) field of the hydrogel, which was then used to calculate the traction stresses exerted by the cells in accordance with established protocols (5). These stresses were used as inputs into a finite element model to estimate the cellular stresses generated by each cell within the cell train as described elsewhere (55). With these information, we were able to study the previously unknown relationship between mechanical communications among the cells and their movement patterns.

2.3. Materials and Methods

2.3.1. Cell Culture

Human umbilical vein endothelial cells (HUVECs) were purchased from Cell Applications Inc. (cat #: 200pK-05n) and expanded in HUVEC media containing 390 mL M199 media (Gibco, cat #: 11150059), 50 mL fetal bovine serum (FBS) (Gibco, cat #: 16000044), 50 mL endothelial cell growth media (Cell Applications, cat #: 500-211), 5 mL

penicillin/streptomycin (Gibco, cat #: 15140163), and 5 mL sodium pyruvate (Gibco, cat #: 11360070). HUVECs were expanded up to passage 7 before being used for the experiments. The cells were maintained at 37° C and 5 % CO2. All experiments, except for the samples used for immunofluorescent staining, used HUVECs that were transduced to express red fluorescent proteins.

2.3.2. Synthesis of protein patterned polyacrylamide (PAm) hydrogels

The micropatterned hydrogel substrates were generated through protein transfer from a patterned coverslip to PAm hydrogel surfaces as described elsewhere (129). Chemically activated confocal grade glass bottom dishes prepared as described below were used to tether the PAm hydrogels to the dish (130).

Activation of the glass bottom confocal dishes

The glass bottom dishes were first treated with 2.5M NaOH (aq) for 15 minutes, washed with DI water, and allowed to fully dry before treating with (3-aminopropyl) trimethoxysilane (silane) (Sigma-Aldrich, 281778) for 5 minutes. The silanized glass dishes were rinsed with DI water to ensure complete removal of the residual silane. The confocal dishes were then treated with 0.5% gluteraldehyde to functionalize the surface with aldehyde groups.

Protein Patterning on Glass Cover Slips

The glass coverslips were first immersed in pure ethanol for 10 minutes to clean their surfaces prior to UV-Ozone exposure for 5 minutes. The UVO irradiated surfaces

were incubated with 0.11 mg/mL poly(L-lysine)-poly(ethylene glycol) (PLL-PEG) (SuSoS AG, Zurich, Switzerland) for 30 minutes to immobilize the surfaces with PLL-PEG chains. Selected regions of the PLL-PEG coated surfaces were irradiated with deep UV via a chrome photomask to selectively eliminate the PLL-PEG coatings. The irradiated surfaces were treated with 50 μg/mL of laminin, which will bind to regions left behind by the degraded PLL-PEG, creating protein patterns on the surface of the glass cover slip.

Transfer of Protein Patterns onto PAm Hydrogel Surface

The protein patterns were transferred onto PAm hydrogels of 8.5 kPa Young's modulus by sandwiching 5 μL of the hydrogel precursor in between the micropatterned cover slip and the activated confocal dish. The precursor solution contained 4.13% wt/vol acrylamide (Sigma-Aldrich, A9099), 0.219% wt/vol N,N'-Methylenebis(acrylamide) (Sigma-Aldrich, 146072), 0.1% wt/vol ammonium persulfate (Sigma-Aldrich, A3678), and 0.1% vol/vol N,N,N',N'-Tetramethylethylenediamine (Sigma-Aldrich, T9281). Dark red fluorescent nanoparticles (ThermoFisher Scientific, F8807) of diameter ~200 nm were dispersed in the precursor solution at a concentration of 0.817% wt/vol to embed the hydrogel network with fluorescent particles. The gelation was carried out at room temperature.

2.3.3. Immunofluorescent Staining of VE-Cadherin

Rabbit vasoendothelial cadherin (VE-Cad) antibody (Cell Signaling Technologies, Cat #. D87F2) was used to stain for VE-cad. The HUVECs on the micropatterned hydrogel substrates were stained 24 hours post-seeding. The samples were rinsed in PBS, fixed with

4% paraformaldehyde (Sigma-Aldrich, cat#: 158127) for 8 minutes, and treated with blocking/permeabilizing buffer containing 0.1% Triton-X 100 (ThermoFisher Scientific, cat#: 28313) and 3% bovine serum albumin (Sigma-Aldrich, cat #5611) for an hour at room temperature. VE-cad antibody diluted in 1:100 blocking/permeabilizing buffer was used to stain the samples by incubating for 1 hour, followed by 3 sequential 10 min washes using PBS. Red fluorescent goat anti-rabbit antibody (1 to 250 dilution in blocking buffer) was used as secondary antibody. The nuclei and actin were co-stained with Hoechst 33342 (Sigma-Aldrich, Cat#: 94403) and alexa fluor 488 phalloidin (Life Technologies, Cat #: A12379) for 15 minutes and 1 hour, respectively.

2.3.4. Image acquisition and processing

Image acquisition via confocal microscopy

The single file HUVEC cells adhered to the PAm hydrogel were imaged using a spinning disk confocal microscope after 24 hours of seeding. Z-stack images (with an interval of 0.2 μm and total thickness of 1 μm) of the embedded fluorescent nanoparticles within the PAm hydrogel were captured using the far red channel at 40X (oil immersion lens). For cell trains that did not fit into a single image, multiple overlapping images were acquired along the length of the cell train in a way that would capture the entire cell train. The overlap was set to 20% on Volocity, the confocal acquisition software, to allow us to stitch these images together in post-acquisition processing. The cell train was mapped over the course of 1.5 hours at 2 minute intervals where the cells were maintained at 37°C and 5% CO2. After imaging, the HUVEC cells were trypsinized with 10X trypsin solution, which restored the hydrogel to its stress-free state. We re-acquired z-stack images of the

same region of the hydrogel to obtain the reference state of the hydrogel. Both the cellular and reference z-stack images were then compressed into 1 single stack using the extended focus function in Volocity.

Image processing and analysis

The overlapping images were imported into MATLAB for processing. Background noise was eliminated by first thresholding signals lower than the average signal of the image. Next, we used the *bwareaopen* function to remove small objects from the image. The images were stitched together by cross-correlating 20% of the left most portion of the right image with 20% of the right most portion of the left image. This procedure allowed us to determine small shifts in the images, which would enable minor adjustments, if needed, before seamlessly overlapping the two images. Each cell was then traced manually by inspection in MATLAB using the *roipoly* function, generating a binary image (hereby referred to as a mask) which was used for the next step. Masks of entire cell-trains could be generated by combining the masks of each cell. These masks could then be superimposed over the original images to obtain images of the cells in the cell train without the interference from the background. It is also from these masks that we obtain information about the left-most and right-most edges of the cell train using the *regionprops* function, as well as the coordinates of the centroid of the cell-train. These coordinates were subsequently used to determine the correlation matrix.

2.3.5. Characterization of cell movement

Correlating movement of the cells of the cell train with that of its centroid

To determine the similarities between the movements of the two cells of the cell train with that of its centroid, we determined the correlation between the trajectories of the two edges of the cell train with the trajectory of its centroid. By trajectory, we imply the set of coordinates x_e of the edges (e = left or right) and x_c of the centroid collected every 2 minutes over a period of 90 minutes, yielding 46 time frames in total. We calculated the correlation coefficient *r* using the following formula:

$$r = \frac{\sum_{i=t}^{t+\Delta t}(x_e(i) - \overline{x_e})(x_c(i) - \overline{x_c})}{\sqrt{(\sum_{i=t}^{t+\Delta t}\left(x_{e,}(i) - \overline{x_e}\right)^2)(\sum_{i=t}^{t+\Delta t}(x_c(i) - \overline{x_c})^2)}}$$

where Δt represents the number of time frames (window) over which the trajectories were correlated, t represents the index of the first time frame in window, and $\overline{x_e}$ and $\overline{x_c}$ represent the average x-coordinate of the edge and the centroid within the window t to $t + \Delta t$. We used the MATLAB *corr2* function to obtain these correlations.

Correlation coefficients were calculated across the entire period of acquisition for varying window sizes (Δt = 1, 2, 3,…, 8). Due to the nature of the formula, the smallest time window of $\Delta t = 1$ (i.e., two time frames) is not informative as it always yields a correlation of $r = +1\ or\ r = -1$. On the other hand, large window size points ($\Delta t \geq 3$)did not yield significant correlation as the trajectories started to diverge over such a large time period. We thereby deduced that the most suitable time window for calculating correlation between the trajectories to be $\Delta t = 2$ (i.e., 3 time frames spanning a 4 minute window). For a leading cell to maintain control over the cell train, it must exhibit a high correlation (r > 0.9) during this time window. The time periods when this criterion is

satisfied were assigned a positive Boolean value for that cell, indicating that the particular cell is in control.

Calculation of normalized length change of the cell train

Using the x-coordinates of each cell, we determined whether the changes in the length of the two cells, ΔL_1 and ΔL_2, were correlated. The length changes for each of the two cells of the cell train were obtained across each 2 min interval and used for calculating their normalized product, as denoted by Q, which is:

$$Q = \frac{\Delta L_1 \cdot \Delta L_2}{\sqrt{\max(\Delta L_1, \Delta L_2)^2}}$$

A negative value of the quantity *Q* indicates retraction in one of the cells accompanied by a stretch in the other cell. On the other hand, a positive value would be observed if both cells were retracting or extending at the same time.

2.3.6. 2-D Traction Force Quantification

The traction forces generated by the cells were quantified as described elsewhere. In brief, using a confocal microscope, we acquired a time-lapse video of a small z-stack images of the fluorescent particles under the cell-train. As the cell train often encompassed more than a single field of view, multiple fields were acquired with a 20% overlap and stitched together in MATLAB. The z-stack was designated to be 1 μm above and below the surface of the hydrogel at 0.2 μm z-intervals to encompass all the particles at the surface. These z-stacks were then compressed into a single focal plane using the Volocity software. The reference image was obtained by imaging the exact same region after

removal of the cells. Using Particle Image Velocimetry (PIV), 2-D displacement fields of the hydrogel surface were obtained comparing the time series images to the reference image using an interrogation window size of 20 μm.

The cell-generated traction forces were calculated by solving the elastostatics equation for a linearly elastic and isotropic solid. A block with dimensions of 800, 250, and 30 μm in the x-, y-, and z-direction was used as the finite-element domain. Here, the tethered boundary condition was imposed at the bottom surface of the domain while the 2D displacement field obtained from PIV were assigned as the x- and y- displacement conditions for the top surface. The z-direction on the top surface as well as the lateral surfaces were approximated to be stress-free. The resultant displacement solution along with a Poisson's ratio of 0.45 and Young's modulus of 8.5 kPa were used to calculate the stress tensor. Here, the τ_{xz} and τ_{yz} values from the stress tensor were designated as the cell-generated traction stresses in the x- and y- directions, respectively.

2.3.7. Finite Element Analysis for Cellular Stresses Calculations

To calculate the cellular stresses, we superimpose the mask of the cells onto the traction stress map generated via TFM analysis. From this superposition, we generated a regularly spaced mesh with stress values assigned at each node. It should be noted that the traction stress in the y-direction were neglected, as the patterned cells generated stresses predominantly along the x-direction. The cellular stresses were calculated by modifying a method previously used by Trepat and colleagues. The force equilibrium of the system dictates that the stresses within the interior of the cell must balance the traction stresses generated by the cell, as expressed by the equation below:

$$\frac{\partial \boldsymbol{\sigma_{ij}}}{\partial \boldsymbol{x_j}} = \boldsymbol{T_i},$$

where $\boldsymbol{\sigma_{ij}}$ represents the monolayer stress tensor, $\boldsymbol{x_j}$ represents each dimension in the Cartesian plane, and $\boldsymbol{T_i}$ represents the traction stresses generated by the cells.

The above equation was solved using a finite element approach where the cell pair was approximated as a linearly elastic and isotropic sheet with a Poisson's ratio of 0.5, Young's modulus of 10 kPa, and height of 10 μm. The finite element domain was designated as the area encompassed by the shape of the cell pair and a stress free boundary condition was imposed along the perimeter. This approach results in a symmetric and positive indefinite linear system of equations that was solved using a minimal residual method to obtain the cellular stresses.

2.3.8. Average Cellular Stress of the Cell Train

The area of the cell train was discretized into defined intervals to create a 2D mesh and the stress at each x-coordinate was obtained by averaging the stresses along the y-axis. This average stress calculated for each x-coordinate was further averaged along the length of the cells to obtain the overall average cellular stress (T_{ave}). To obtain a representation of cellular stress across the x-axis, we obtained a net force by summing the stresses across the cross sectional area of the cell, which we estimated using a cellular height of 10 μm and the measured width of the cell to yield the summed force. Following that, we average the summed force along the cell train in the y-axis. For this, we superimposed the mask generated during imaging over the map of the cellular stresses calculated prior. We then

summed the average forces along the y-axis, and divided that quantity by the width of the HUVEC cells to obtain an average cellular stress along the x-axis of the cell.

2.3.9. Calculation of malleability of the cell body

The dynamic stiffening and softening behavior of each cell was determined by comparing the discretized second derivative of the average cellular stress with respect to length, $\Delta^2 T_{ave}/\Delta L^2$. First, we obtained an instantaneous modulus of the cell by evaluating the quantity $\Delta T_{ave}/\Delta L$ at every time point. From this profile, we further calculated the second derivative. A negative value for the second derivative means the cell is softening whereas a positive value indicates the cell is stiffening.

2.3.10. Correlating control state of the cell with its mechanical modulus

The mechanical state of the cells (i.e., softening, stiffening, or neutral) were classified according to their control state (i.e., leading or trailing cell) which yielded 6 different scenarios: (1) fraction of trailing cells that were softening, (2) fraction of leading cells that were softening, (3) fraction of trailing cells that remained neutral, (4) fraction of leading cells that remained neutral, (5) fraction of trailing cells that were stiffening and (6) fraction of leading cells that were stiffening. To determine whether the trailing or leading cells dominate a particular mechanical state, we have subtracted the fraction of leading cells from the trailing cells for that mechanical state; thereafter this quantity is denoted as Φ. A positive value for Φ means more trailing cells at that mechanical state, and vice versa.

2.4. Results and discussion

2.4.1. Tracking cellular trajectories reveals an element of control among the cell pairs

Fig. 2.4 shows the kymograph of a representative cell-train plotted in terms of the longitudinal coordinates of the outer edges and the centroid of the cell train; The entire collection of kymographs analyzed in this study are provided in Fig. 2.5. The plots reveal time periods during which the trajectory of one of the cells resembles the trajectory of the centroid, indicating that the cell train is under the control of that cell. This finding agrees with the current understanding that collective migration of cells is a result of cumulative maneuvers of individual cells.

We further calculated the correlation between the trajectories of the individual cells and that of the centroid, and identified time windows during which close resemblance between the trajectories were observed (see Materials and Methods 2.3.5). The resulting Boolean plot (Fig. 2.6) shows the time and duration in which none, one, or both cells were in control of the cell train. The analysis reveals oscillatory behavior, where the role of the "leading" cell (the one in control) and the "trailing" cell (the other cell) alternates between the cell pair. The oscillations are interspersed with time periods where neither cell is in control and occasionally with periods where both cells are in control. We next analyzed all the kymographs to determine the fraction of time where the centroid was controlled by none, one, or both cells (Fig. 2.7). The results confirmed that the control of the cell pair lies mostly between one of the two cells and very rarely with both cells at the same time. Furthermore, this control by one cell appears to exist only half of the time. Taken together, these results demonstrate that there is limited simultaneous coordination between the two

cells, as both cells tend to only temporarily take on the role of the leading cell before falling back to becoming a trailing cell.

2.4.2. Differential cellular deformation among the cell pair during collective migration

By averaging the cellular stresses along the y-axis at each time point, we obtained a stress kymograph that describes the average cellular stress within the cell train (Fig. 2.12). This cellular stress data was further averaged along the length of the cell and compared against the cell length to assess whether the magnitude of the stress has an impact on the length of the cell (Fig. 2.13). Our results revealed a generally poor correlation between the amount of stress exerted by the cell and its length, demonstrating that there is no direct relationship between mechanical stress and the length of the cell. This suggests that the cell dynamically alters its own mechanical properties during collective migration. Such dynamic stiffening and softening behavior in the cell may be envisaged in terms of changes in the intrinsic elastic constant (modulus) of the cell. We approximated these changes in elastic constant by taking the second derivative of the cellular stress with respect to the length of the cell (see Materials and Methods 2.3.3). By comparing this quantity to the state of control in the cells obtained earlier, we find that the trailing cell is more often undergoing softening while the leading cell maintains its elastic constant (Fig 2.14). From these findings, we can infer that trailing cells within a group are more likely to soften in response to the adjacent cells pulling or tugging at them. Additionally, we examined the time-dependent changes in the lengths of the two cells and calculated their normalized product (Fig 2.8). Our results showed an overall negative value for the normalized product, which

indicates that the cells undergo opposite changes in lengths. This finding suggests that there may be a physical response to collective cellular migration, corroborating previous suggestions that there is a physical tug-of-war occurring between the cells during collective migration (131).

2.4.3. Traction force microscopy and cellular stress calculation uncover dynamic malleability in cells during collective migration

To provide a mechanical basis for these observed phenomena, we estimated the traction and cellular stresses exerted by the cell train (see Materials and Methods 2.3.6 and 2.3.7). A representative displacement field and the corresponding traction stress map generated by one such cell train during movement are shown in Fig. 2.9 and Fig 2.10 respectively. Due to the geometric confinement of the cells, the traction stresses observed in the longitudinal (x) direction were much larger than those in the other two directions. It was also observed that most of the generated traction stresses were localized to the two ends of the cell train.

The cellular stresses were estimated from finite elements analysis, based on a geometrical model of the cell train obtained from its fluorescent images and the predominant x-component of the previously obtained traction stresses as the boundary condition (see Supporting Information). A representative stress profile from one of the cell trains is shown in Fig. 2.11. We observe that the cellular stresses are quite homogenously distributed across the two cells, with peaks close to the edges of the cell trains where the traction forces also peak. These stresses are lower in the middle where the cells are joined

together, which is a direct result of trace amounts of traction stresses under each cell that are exerted in the opposite direction to the traction stresses at the edges. This could be a protective mechanism used by the cells to minimize stresses across cell-cell junctions to prevent them from being mechanically torn apart.

By averaging the cellular stresses along the y-axis at each time point, we obtained a stress kymograph that describes the average cellular stress within the cell train (Fig. 2.12). This cellular stress data was further averaged along the length of the cell and compared against the cell length to assess whether the magnitude of the stress has an impact on the length of the cell (Fig. 2.13). Our results revealed a generally poor correlation between the amount of stress exerted by the cell and its length, demonstrating that there is no direct relationship between mechanical stress and the length of the cell. This suggests that the cell dynamically alters its own mechanical properties during collective migration. Such dynamic stiffening and softening behavior in the cell may be envisaged in terms of changes in the intrinsic elastic constant (modulus) of the cell. We approximated these changes in elastic constant by taking the second derivative of the cellular stress with respect to the length of the cell (see Materials and Methods 2.3.3). By comparing this quantity to the state of control in the cells obtained earlier, we find that the trailing cell is more often undergoing softening while the leading cell maintains its elastic constant (Fig 2.14). From these findings, we can infer that trailing cells within a group are more likely to soften in response to the adjacent cells pulling or tugging at them. Additionally, we examined the time-dependent changes in the lengths of the two cells and calculated their normalized product (Fig 2.8). Our results showed an overall negative value for the normalized product, which indicates that the cells undergo opposite changes in lengths. This finding suggests that

there may be a physical response to collective cellular migration, corroborating previous suggestions that there is a physical tug-of-war occurring between the cells during collective migration.

2.5. Conclusion

In summary, we have examined the subtle mechanical signals cells use to communicate with each other to induce changes in each other's mechanical properties. By imaging and analyzing conjoined pairs of cells, we observed that the two cells take alternate turns in assuming control over the movement of the cell train. Another observation is the antagonistic change in the length of the two cells, where the lengthening of one cell is often accompanied by the shortening of the other cell. Together, this suggests that there is a physical tug of war rather than cooperation between the two cells, which inadvertently ends up preventing the cell train from making significant progress in migration. Further analysis of the traction and cellular stresses in each cell train allowed us to probe the mechanical basis for the observed tug-of-war behavior. Interestingly, the magnitude of these stresses showed little correlation with cell length, suggesting that each cell dynamically modifies its own intrinsic modulus to soften or stiffen its own body over time. Relating the occurrence of such softening or stiffening events to temporal variations in control state of the cells revealed that softening events were more likely to occur in trailing cells. These results suggest that trailing cells responding to mechanical cues soften their own cellular bodies to ease the load of leading cells to pull them along in the direction of migration.

2.6. Acknowledgements

The authors would like to thank all members of the Varghese lab at UCSD for their suggestions and fruitful discussions. We would also like to acknowledge Jennifer Santini for assistance with microscopy and image analyses and UCSD as the primary source of funding.

Chapter 2, in full, is a reprint of the material that has been submitted to Biotechnology Journal. “Alternating Control and Dynamic Malleability in Cell Pairs”. Lim, Han L.; Aung, Aereas; Arya, Gaurav; Varghese, Shyni. The dissertation author was the primary investigator and author of this paper.

2.7. Figures

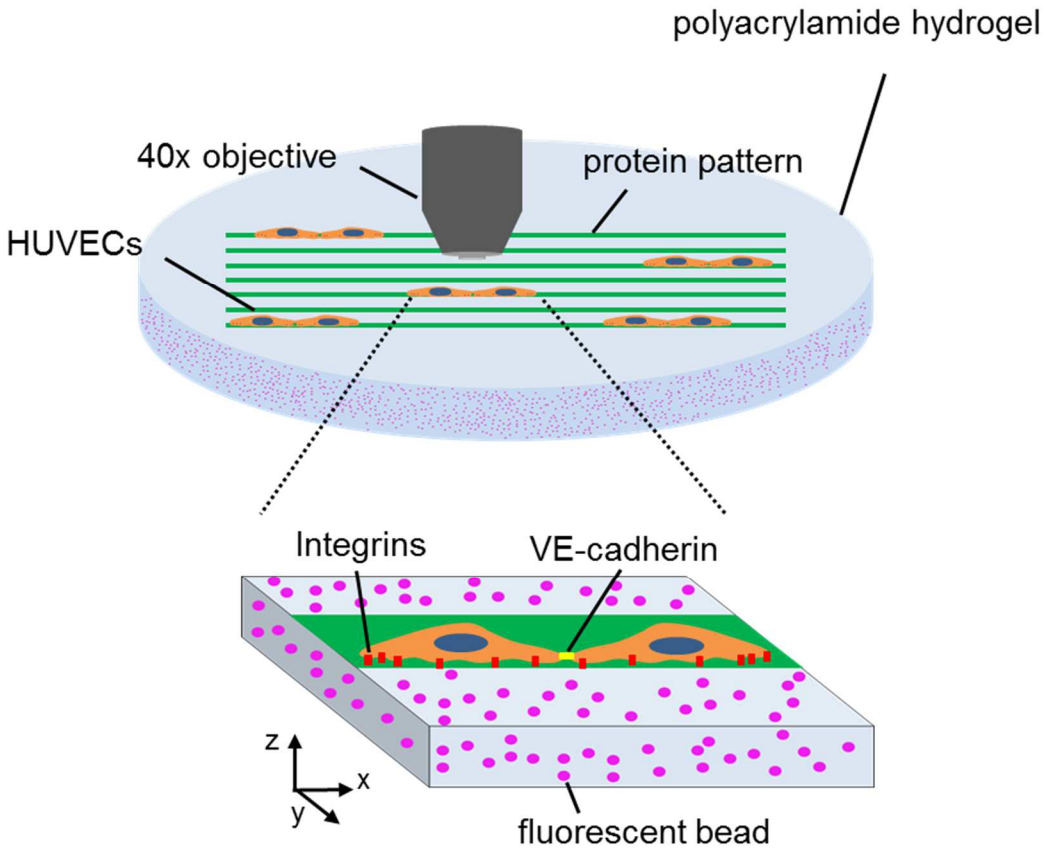

Figure 2.1: Schematic of cell trains on a hydrogel substrate with protein line patterns.

Top schematic shows pairs of human umbilical vein endothelial cells (HUVECs) conforming to protein line patterns on top of a polyacrylamide hydrogel. The hydrogel is seeded with fluorescent beads that we can image to obtain the deformations that the cells are applying onto the substrate. A 40x objective is used to image these cells. Bottom schematic shows a zoomed in a version of one such cell-pair attached to the substrate via integrins and attached to each other via vaso-endothelial cadherins (VE-cadherin).

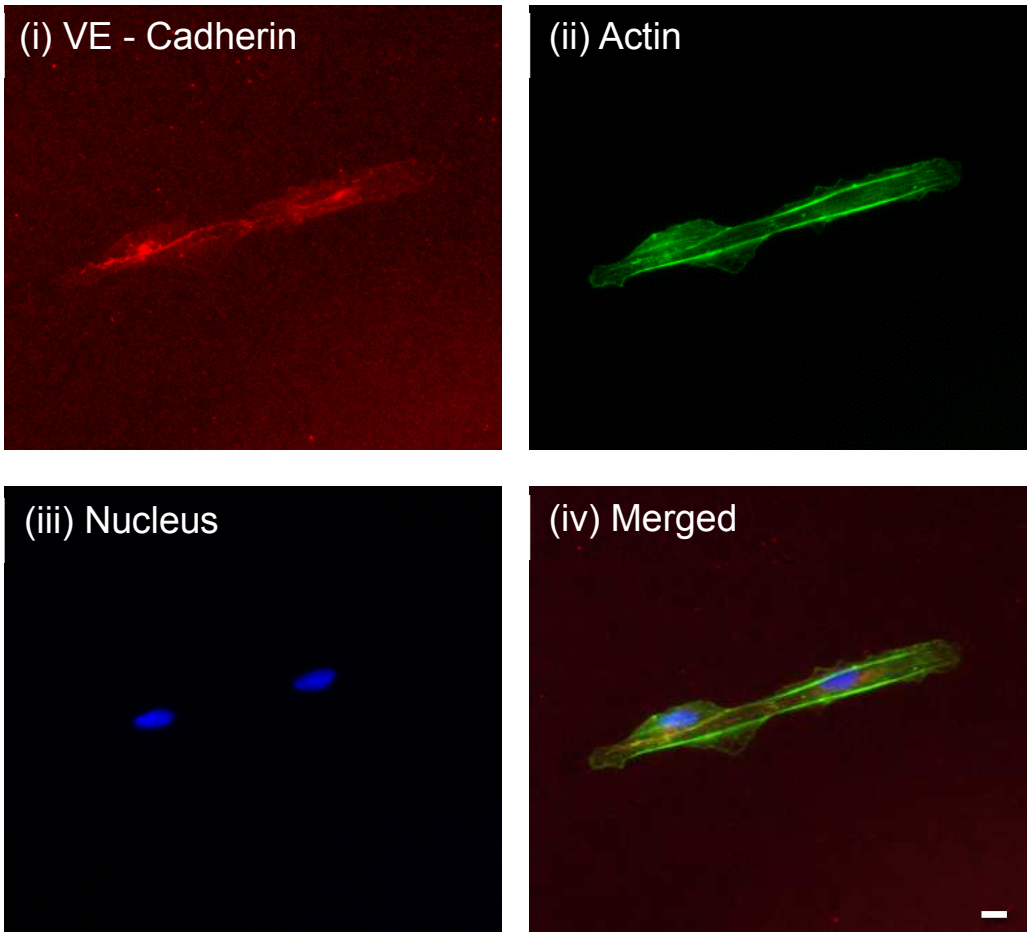

Figure 2.2: Immunofluorescent staining images of pairs of cells on hydrogel substrate.

Immunofluorescent images of the cells pairs showing (i) VE-cadherin, (ii) actin, (iii) nucleus, and (iv) merged. The HUVECs clearly express VE-cadherin at the cell-cell junction, signifying their physical attachment to each other. This will allow them to interact physically and mechanically with each other as they move along the straight protein pattern. Scale bar: 20 μm.

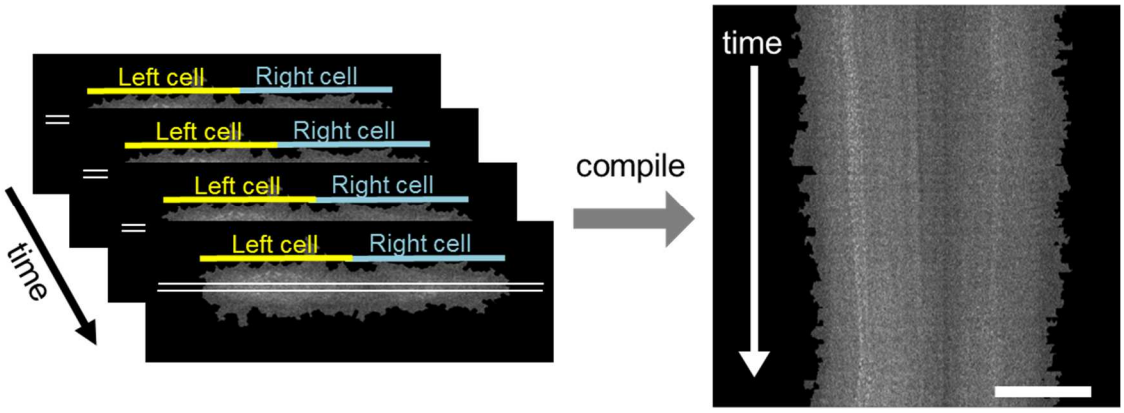

Figure 2.3: Compiling a kymograph from individual cell pair images.

The kymograph of the cell train over 90 min (right) is constructed from time-lapse image of the cell train taken at 2 min intervals (left). White lines denote the stripe-like portion of each image used for building the kymograph. Scale bar: 50 μm.

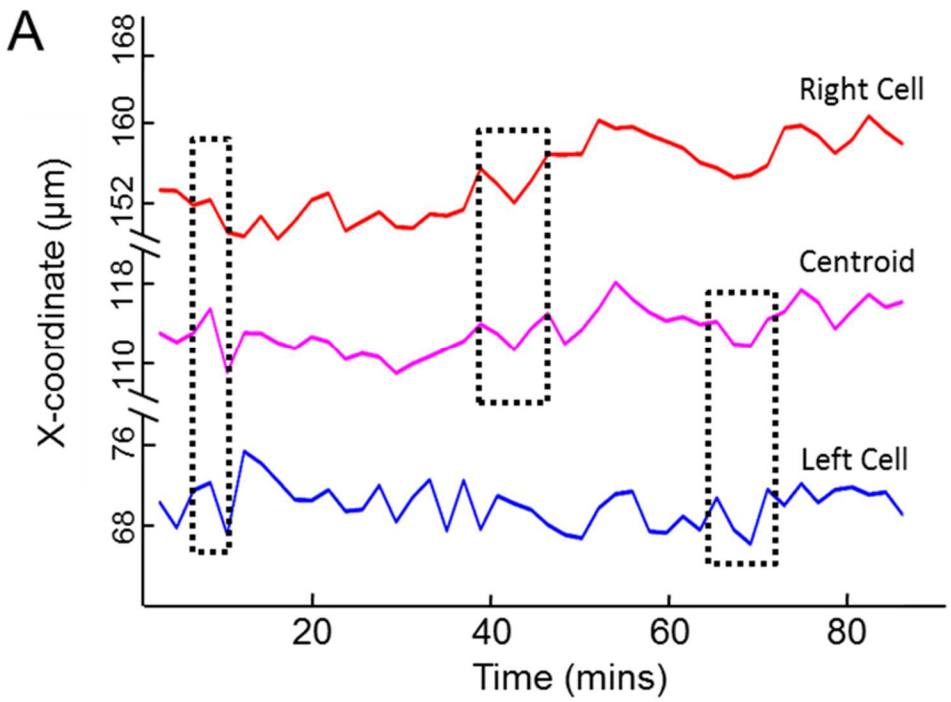

Figure 2.4: Trajectories of the right and left edges, as well as the centroid for one representative cell train.

Time-dependent positions of the outer edges of the two cells and of their centroid for a representative cell train are plotted in Fig 2.4. Areas of high correlation between movements of either of the two cells with those of the centroid are indicated in dashed boxes

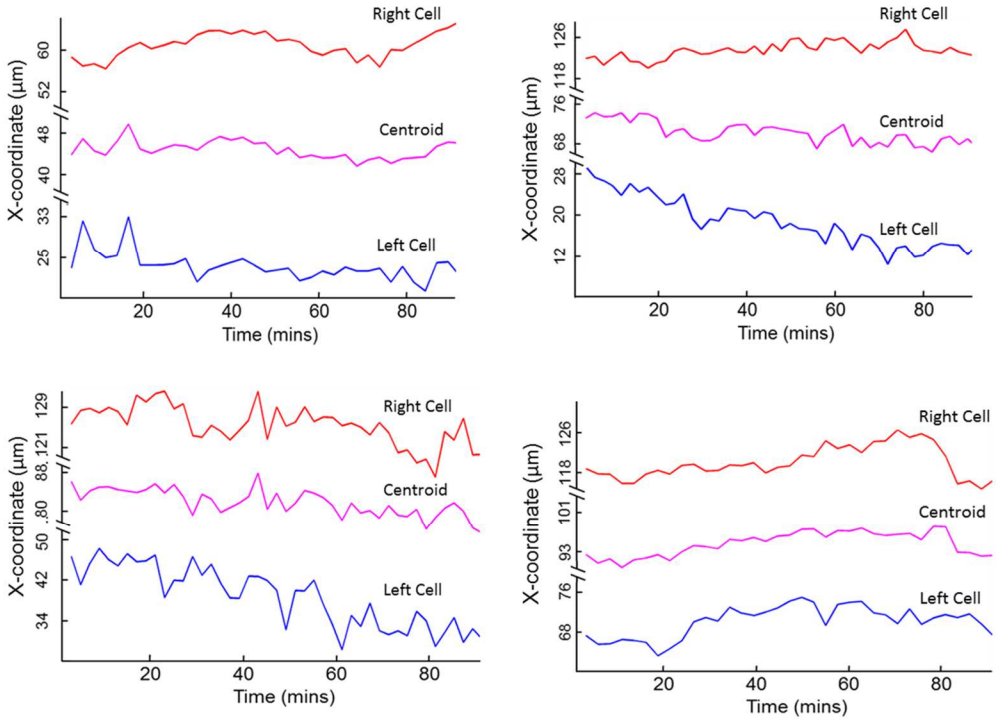

Figure 2.5: Trajectories of the right and left edges, as well as the centroid for the remaining four cell trains.

Time-dependent positions of the outer edges of the two cells and of their centroid for the remaining four analyzed cell train.

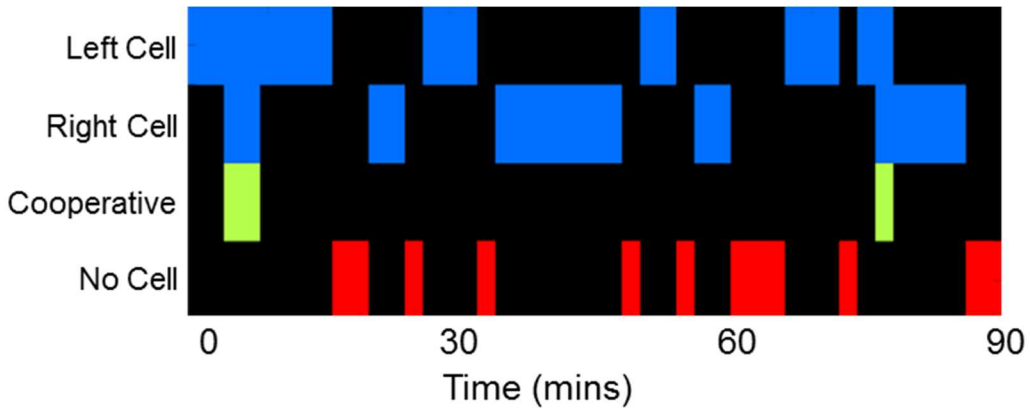

Figure 2.6: Time periods of high correlation between the left and right cell and the centroid.

Time windows during which the movement of either of the two cells (blue), or simultaneously both cells (green), exhibit high correlation with the movement of the centroid for the representative trajectories shown in Fig. 2.4. Also shown are time durations when none of the cells exhibit any correlation (red).

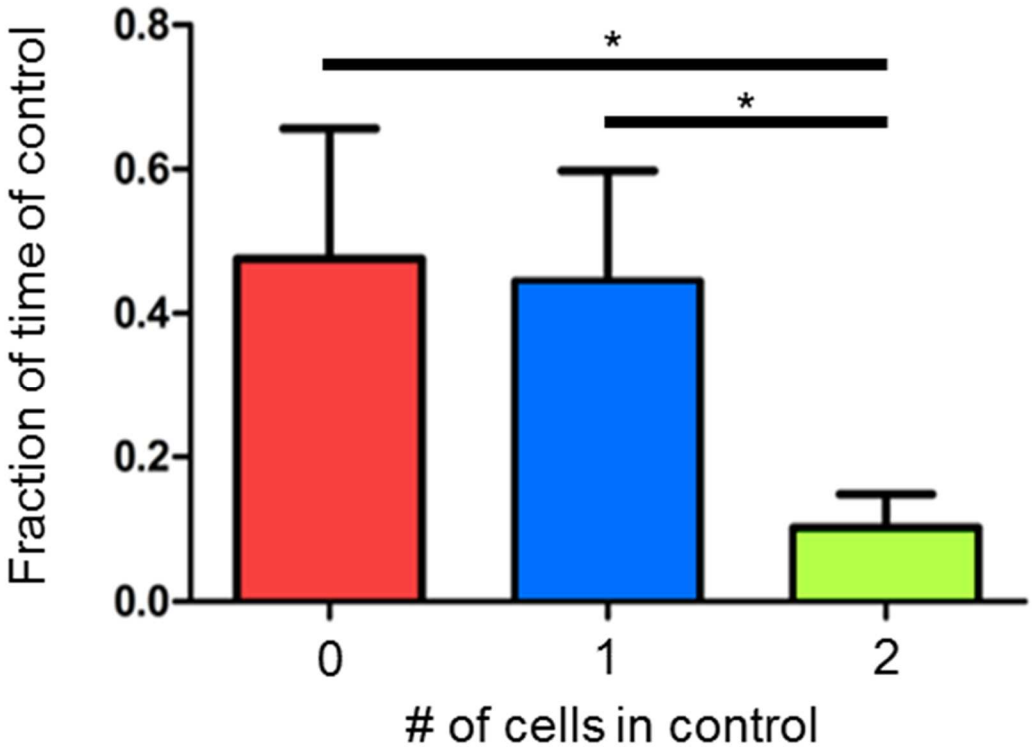

Figure 2.7: Fraction of time of Control over the centroid.

Fraction of time when the control of the centroid is not with any cell (red), with only one of the cells (blue), and with both the cells (green), averaged over all recorded cell trains (n=5).

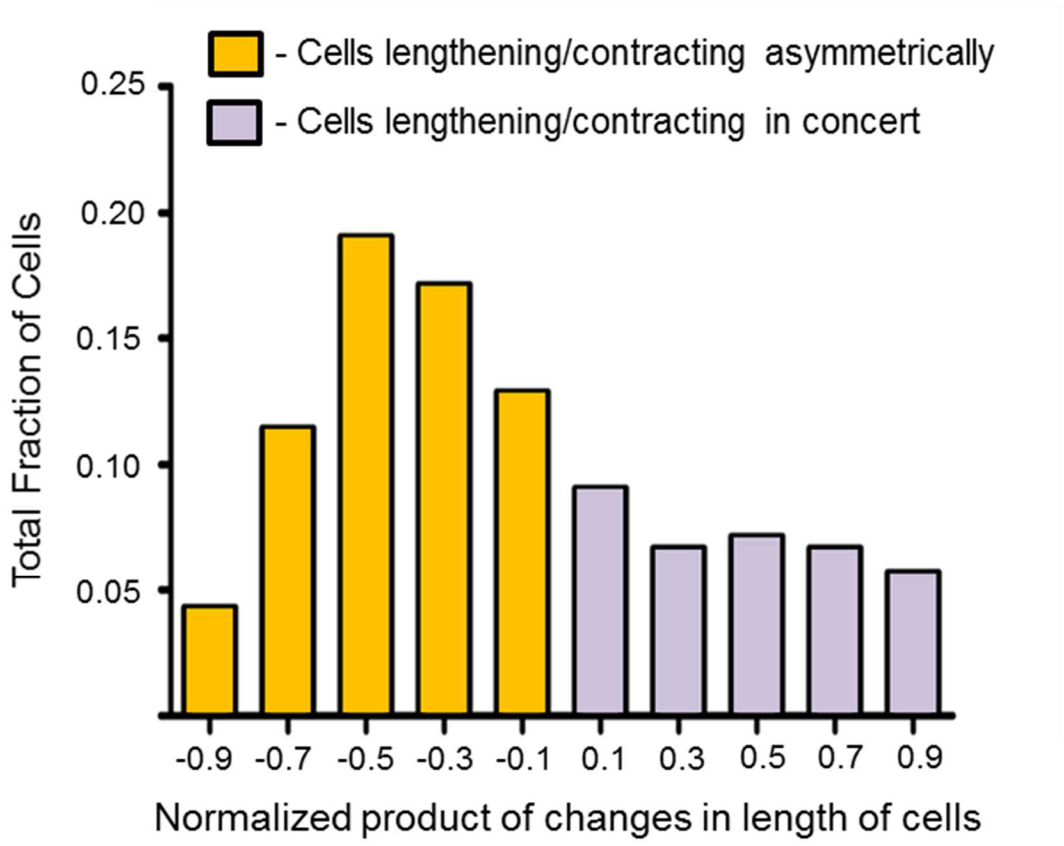

Figure 2.8: Normalized product of length change in both cells.

Distribution of the normalized product of length changes in both cells averaged over all cell trains. Negative values (in orange) represent contradicting cellular movements (extension in one cell and contraction in the other) while the positive values (in purple) represent similar cellular movements (both cells contracting or extending).

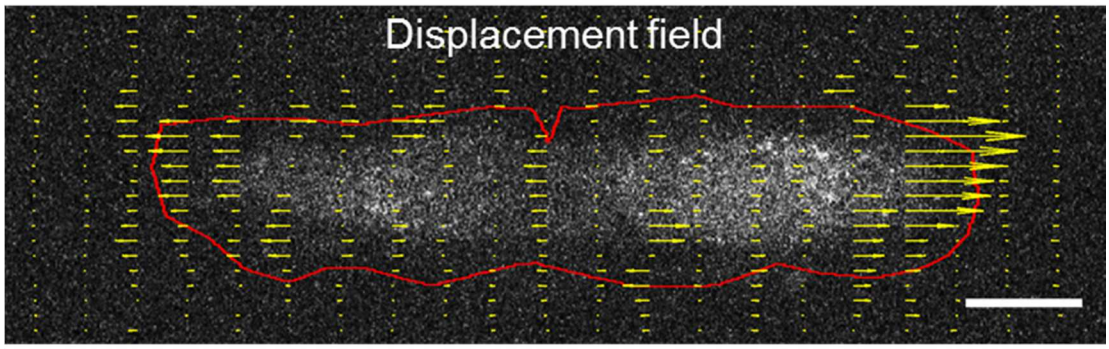

Figure 2.9: Displacement field of the hydrogel substrate under two cells

Map of the displacement field (yellow) overlaid with a fluorescent image of the 2-cell train for a representative image acquired during time lapse. Scale bar denotes 40 μm.

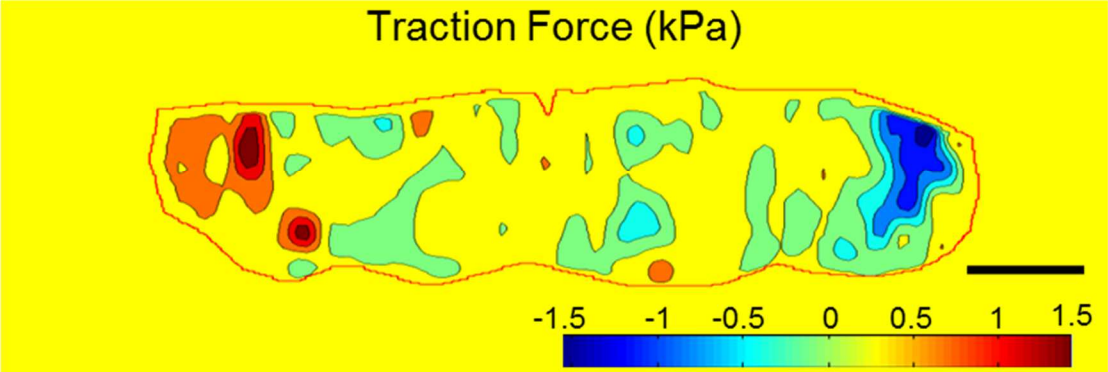

Figure 2.10: Traction stresses exerted by the two cells

Traction force profile of the same 2-cell train shown as a contour map. Red implies that that traction force is pulling towards the right while the blue represents that the traction force is pulling towards the left. The outline of the cell is traced in a red line around the traction map. Scale bar denotes 40 μm.

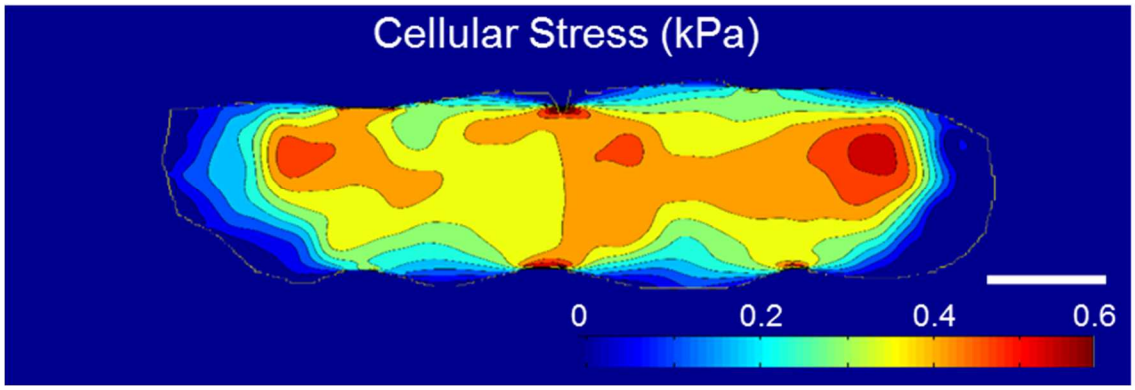

Figure 2.11: Cellular (inter- and intra-) stresses within the two cells

The cellular stress profile for the same 2-cell train also shown as a contour map. The 2-cell trains are outlined in yellow. Scale bar denotes 40 μm.

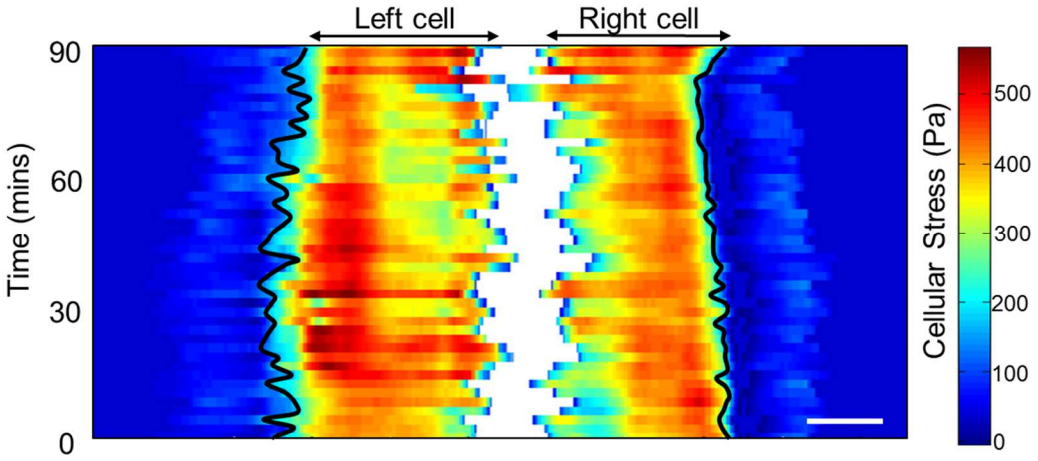

Figure 2.12: Mechanical kymograph of the cell pair over time

Representative kymograph of cellular stresses within each cell across the entire imaging time period of a cell train. White gap is placed in the middle to indicate two separate cells, and the edges of the cell train are denoted with a black line. Scale bar: 40 μm.

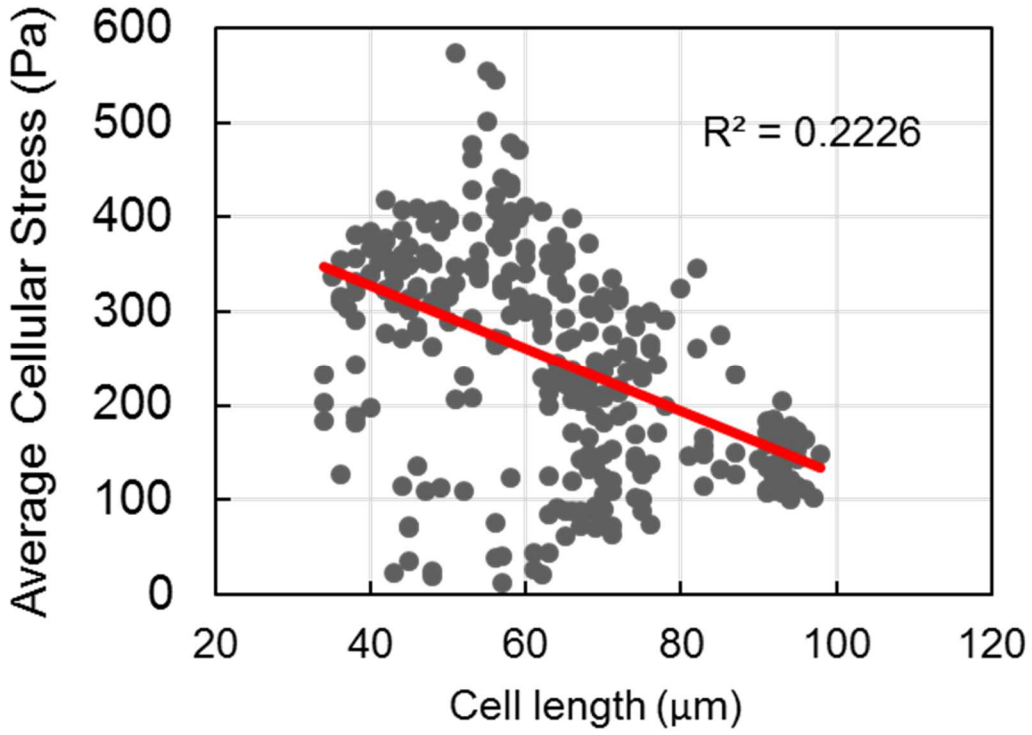

Figure 2.13. Average cellular stress against cell length

Scatter plot of the average cellular stress versus length of the cell at that time. A linear regression of data yields an R^2 value of 0.2226, yielding low correlation between stress and length of the cell.

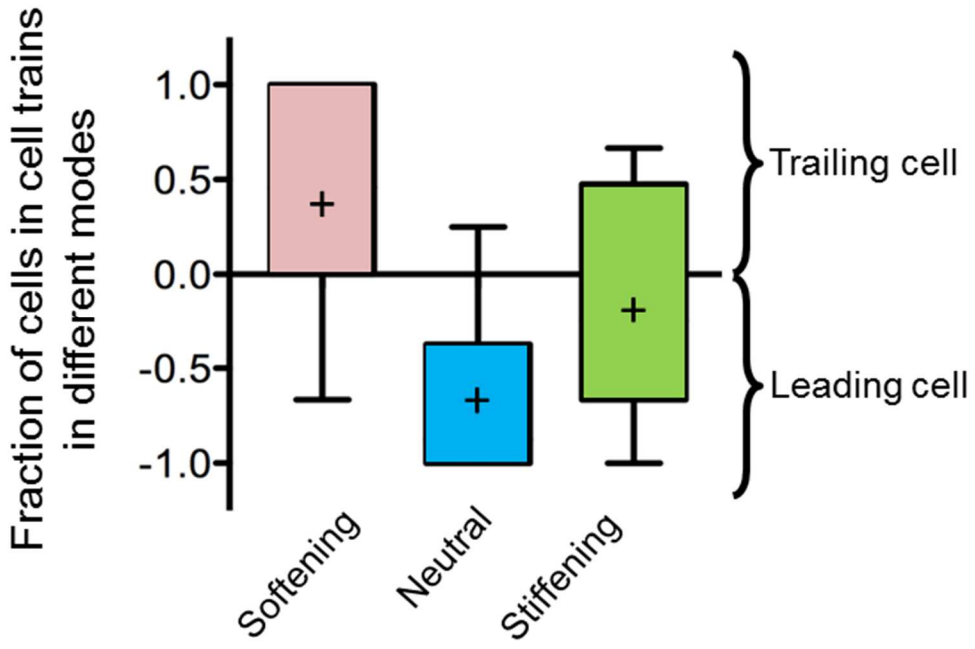

Figure 2.14: Fractions of cells within cell trains at different mechanical states

Fractions of cellular populations observed to be in the softening (pink), neutral (blue), and stiffening modes (green). Amongst neutral cells, a large proportion of them tend to remain at a neutral mechanical state, while amongst the softening cells, many of them tend to be trailing behind the leader cell.

Chapter 3: Quantifying Diffusivity amongst Cancer Spheroids Cultured in Matrices of Different Stiffnesses

3.1. Abstract

One of the problems faced in the pharmacologic treatment of solid tumors is the cancer cells' ability to grow and form tumors in sites distant from the circulatory system (61-64, 86). This leads to exposure of the tumor to drastically lower concentrations of therapeutic molecules, which may, over time lead to the rise of adaptive drug resistance within the tumor (19, 20, 66, 70, 132). As such, one major consideration to consider during the drug discovery phase is the diffusive properties of the compound. While there have been methods that characterize the diffusivity of a compound within solid tumors, many of these methods consider the diffusivity within the tumor to be homogenous in nature despite the heterogeneous nature within tumors due to conditions like hypoxia deep within the tumor (86). To better characterize diffusivity within solid tumors, we have devised a novel method that can be used to quantify the diffusion coefficient in different regions within a tumor. As other studies have shown that physical factors in the tumor microenvironment can affect the expressed phenotype of the tumor, we applied our method on cancer cell spheroids encapsulated within hydrogels of different rigidities. Our results show that there is a statistical difference in the diffusivity at the core of the spheroids when they are encapsulated in hydrogels of different rigidities. This implies that the intercellular stresses that the cells experience as a result of their proliferation could affect the diffusivity of the core of the spheroid.

3.2. Introduction

One of the many challenges in the pharmacologic treatment of cancer is the cancer cells' ability to form and grow in sites distant from the circulatory system, thereby limiting the transport of therapeutic molecules to the tumor via convective mass transfer (61-64, 86). As such, most of the transport of molecular agents into the tumor is driven by diffusion, which is a much slower process. Over time, cancer cells exposed to sub-lethal concentrations of the molecule develop adaptive drug resistance, rendering further administration of the same drug ineffective (19, 20, 66, 70, 132). This highlights the need to better understand the diffusive properties of a molecule through solid tumors before administration as it can be a key differentiator of effectiveness for drugs in vivo.

To date, many groups have characterized the diffusion of different therapeutic agents in various *in vitro* models for cancer. These models are often derived from growing cancer spheroids or other forms of multicellular aggregates (71, 72, 74), from which an average diffusion coefficient is calculated after exposure to a fixed concentration of the therapeutic agent (86). Results from these studies also led to the observation that different cancer phenotypes can lead to drastically different diffusive properties in tumors. For example, loosely packed tumors created from cancer cells that secrete large amounts of extracellular matrix have lower resistances to diffusion than their more tightly packed counterparts (61). In another instance, tumors formed from cancer cells that express higher quantities of epithelial-cadherin exhibited a greater resistance to diffusion, due to their ability to form more tight junctions between the cancer cells (133). The observations made in these studies have addressed how different cancer cell phenotypes can directly influence the efficacy of different drugs by affecting the molecular penetration into the tumor.

However, many of these studies make the over-generalizing assumption that diffusion within these tissues is homogenous in nature, when it could change spatially within the tumor due to different biological conditions, like hypoxia deep in the tissue. Recognizing that there are few methods out there that directly and mathematically address the diffusivity of a molecule within sub-regions of a tumor, we devised a novel method that can be used to calculate the diffusion coefficient of a molecule within a cancer spheroid.

In applying our method, we have chosen to test our method against cancer spheroids encapsulated within gelatin methacrylate (GelMA) hydrogels, which not only holds the cancer spheroid in place, but also serves as a simple tumor microenvironment. As many other studies have shown that the physical and mechanical properties of the tumor microenvironment often play an important role in determining the phenotype of the cancer within, we tested our method against these spheroids encapsulated within hydrogels of different rigidities. Our results show that the matrix rigidity has an effect only in the most inner core of the spheroid, where we determined that the spheroid encapsulated within the hydrogel with the softest rigidity had diffusion coefficient that was higher than those encapsulated in the stiffer hydrogels

3.3. Materials and Methods

3.3.1. Gelatin Methacrylate (GelMA) Synthesis

Methacrylate functional groups were added to gelatin using the protocol described elsewhere (100). In brief, 10.0g of bovine skin gelatin (Sigma Aldrich, St. Louis, MO, USA) was added to 100mL of phosphate buffered saline (PBS) at 60 °C with vigorous stirring to achieve complete solvation. The solution was then lowered to 50 °C, and 8mL

of methacrylic anhydride (cat no.: 276685; Sigma Aldrich) was added to the solution dropwise while maintaining vigorous stirring. This solution was further kept for an hour at 50 °C with vigorous stirring after complete addition of methacrylic anhydride, after which, 200mL of PBS was added to quench the reaction. The solution was then dialyzed in MilliQ water using 12-14 kDa cutoff dialysis tubing (Spectrum Laboratories, Rancho Dominguez, CA, USA) for 1 week with 2 changes of water daily at 45°C to remove trace contaminants. Lastly, the GelMA solution is flash frozen in liquid nitrogen and lyophilized in a freeze dryer for 5 days before being stored at −20 °C. The GelMA was used within 2 months of its synthesis

3.3.2. Compression testing of GelMA hydrogels

The rigidity of hydrogels of different monomer concentrations was measured using Instron 3342 Universal Testing System (Instron, Norwood, MA, USA) equipped with a Model 2519-104 force transducer. Briefly, GelMA hydrogels of 7.5%, 10.0% and 12.5% monomer concentration were allowed to reach their equilibrium swollen state by submerging for 48 hours in PBS. These gels were then subject to a maximum force load set to 450 N at a crosshead speed of 10mm/min. The data acquisition was performed with BlueHill software, and the compressive moduli of the different hydrogels were determined by calculating the slope of the initial linear region of the stress-strain curve. Three samples were used to estimate the mechanical properties for each experimental group.

3.3.3. Fabrication of Silicon Mold

Micropatterned silicon molds were fabricated according to the protocol as described previously. In brief, microfluidic channels were photolithographically defined using NR9-1500PY negative photoresist (Futurrex, Frankling, NJ, USA) on a 4-inch diameter Si wafer. The Si wafer with the photoresist defined was then etched using the deep reactive ion etching (DRIE) process. In the DRIE process, SF6 gas was flowed at 100 sccm throughout the 11 seconds of reaction time, followed by a passivation cycle when C4F8 gas was flowed at 80 sccm for 7 s. A 75 μm of etching depth was achieved under the etching rate of about 0.7 μm per cycle. After the DRIE process, the NR9-1500PY photoresist was removed by immersing in acetone for 4 hours before rinsing with methanol, isopropanol, and deionized water. The Si mold was then dried under compressed nitrogen gas and silanized by vapor deposition of trichlorosilane (TCI Inc, Portland, OR, USA) to facilitate PDMS molding and removal.

3.3.4. Fabrication of Microfluidic Device

The microfluidic device was fabricated with minor modifications from a previous protocol (100). Once assembled, the device will contain a trilayer hydrogel system where cancer spheroid-laden GelMA hydrogels are sandwiched between thin polyacrylamide (pAm) hydrogel sheets. The fabrication and assembly is described as follows:

Methacrylation of cover glass

Cover glass on which thin pAm hydrogels were synthesized were functionalized with methacrylate groups to allow for chemical tethering of hydrogels containing vinyl

groups. This was achieved by treating cover slips with a silanizing solution comprised 1.9mL ethanol, 60 µL of 10% glacial acetic acid and 40µL of 3-(Trimethoxysilyl)propyl methacrylate (cat no.: 440159; Sigma Aldrich) for 5 minutes at room temperature. The surface modified cover slips were then washed by submerging into pure ethanol with gentle stirring for 10 minutes several times before drying at 50 °C for 5 minutes. The cover slips were then used immediately.

pAm hydrogel formation

Thin sheets of pAm hydrogels were formed on 24x50 mm rectangular and 12 mm diameter round methacrylate-functionalized cover slips. This was done by first mixing a pAm hydrogel precursor solution comprising 4% (w/v) acrylamide (cat no.: A3553; Sigma Aldrich), 0.2% (w/v) bis-acrylamide (cat no.: 146072; Sigma Aldrich), 0.1% (w/v) ammonium persulfate (APS) (cat no.: A3678; Sigma Aldrich), and 0.1% (v/v) N,N,N',N'-Tetramethylethylenediamine (cat no.: T9281; Sigma Aldrich) in PBS. 5 µL of this solution was then immediately pipetted onto the middle of the 24x50 mm rectangular cover slip and covered immediately with an untreated 12 mm diameter cover slip. The resulting coverslip containing the hydrogel forms the base onto which the polydimethylsiloxane (PDMS) device can be bonded on. Similarly, 5 µL of this solution was also immediately pipetted onto the middle of the 22x22 mm untreated square cover slip and covered immediately with the methacrylated 12 mm diameter cover slip. Both pAm hydrogels were left to form for 30 minutes at room temperature in a humidity chamber before removal of the untreated cover slips, leaving only pAm hydrogel disks tethered to the methacrylated surfaces of the cover slips.

PDMS molding and bonding

A 5 μL droplet of DI water was first pipetted on the circular region of the fabricated silicon mold before the pAm hydrogel-tethered cover slip was placed on it, with the hydrogel surface down. PDMS (Sylgard 184, Ellsworth Adhesives) polymer solution was mixed with its curing agent at a ratio of 10:1 by mass and degassed under vacuum to remove bubbles from the mixture. The PDMS solution was then slowly poured onto the wafer containing the cover slips and baked at 55 °C for 2 hours. The cured PDMS is then detached from the wafer, along with the hydrogel-tethered cover slip embedded on the inner surface. This PDMS is then bonded to the pAm hydrogel tethered rectangular cover slip at 80 °C overnight following UV-ozone treatment. Following the bonding of PDMS to the glass cover slip, we obtain a perfusable microfluidic chamber whereby the top and bottom of the chamber is covered with thin pAm hydrogels.

3.3.5. Synthesis of lithium phenyl-2,4,6-trimethylbenzoylphosphinate (LAP) as a photoinitiator

LAP was used as a photo initiator for the polymerization of GelMA hydrogels used in the study. The synthesis of LAP was done in accordance with protocols described elsewhere. In brief, 2,4,6-trimethylbenzoyl chloride (cat no.: 682519; Sigma Aldrich) was added dropwise to an equimolar quantity of dimethyl phenylphosphonite (cat no.: 149470; Sigma Aldrich) at room temperature under argon while stirring. The two reagents were allowed to react for the next 18 hours. Afterwards, the temperature of the mixture was raised to 50 °C and 4 molar excess of lithium bromide (cat no.: 213225; Sigma Aldrich)

mixed with 2-butanone (cat no.: 360473; Sigma Aldrich) was added. Precipitation was observed within 10 minutes. Next, the temperature was cooled back down to room temperature and allowed to rest for 4 hours. Next, to remove excess lithium bromide, the precipitate was filtered and washed 3 times with 2-butanone. Lastly, the product was dried under vacuum to removed remaining 2-butanone.

3.3.6. Synthesis of acellular GelMA hydrogels in device

The algorithm used to solve for the diffusion equation in our simulations were tested against experimental data obtained from tracking the diffusion of fluorescein isothiocynate (FITC)-dextran (40kDa) (cat no.: 53379; Sigma Aldrich) into GelMA hydrogel disks of different concentrations in the device. To synthesize these disks, GelMA was first dissolved in PBS in concentrations of 7.5%, 10.0% and 12.5% wt/vol. LAP was used as a photoinitiator at a concentration of 2mM, while ascorbic acid (cat no.: A4403; Sigma Aldrich), an antioxidant that was used in cellular experiments, was added to a concentration of 0.01% (wt/vol).

The solution was then infused into the microfluidic device, exposed to collimated UV light through a 320 μm pinhole on a transparency photomask (CAD/Art, Coos County, Oregon, USA.) for 12 seconds, allowing for the GelMA to polymerize. Following polymerization, PBS is flushed into the device to remove unreacted GelMA solution. Fresh PBS is infused into the device to allow the GelMA structures to reach equilibrium swelling overnight.

3.3.7. Formulation of the algorithm determining the diffusion coefficient

The algorithm was formulated based on the integral form of the diffusion equation,

$$\iiint_V \frac{dc}{dt}\, dV = -\iint_S \boldsymbol{j} \cdot dS$$

Where the left hand side represents the cumulative sum of the time differential of the concentration, c, within an arbitrary control volume, V, and the right hand side represents the total flux, j into the surface area, S, of the control volume. Given that Fick's law of diffusion states:

$$\iiint_V \frac{dc}{dt}\, dV = -D_c \iint_S \boldsymbol{\nabla c} \cdot dS$$

Where Dc represents the diffusion coefficient, while $\triangledown$c represents the gradient of c. We can then make the substitution, while applying the assumption that D_c is constant to yield:

$$\iiint_V \frac{dc}{dt}\, dV = -D_c \iint_S \boldsymbol{\nabla c} \cdot dS$$

On the left hand side, determination of dc/dt was performed by first averaging the concentration within each control volume to minimize the impact of noise, prior to obtaining the time dependent changes in the average concentration using 2nd order central finite difference scheme. The integral was then computed by summing up within the control volume. For the right hand side of the equation, determination of ∇c was achieved by taking a change in average concentration between the control volume and the average concentration of control volumes adjacent to the designated region. This difference was then multiplied into the surface area of the control volume of interest to quantify the

theoretical average flux into the region of interest. In this form, we are able to solve for D_c by isolating it on one side, expressing it as a ratio of the volume to the surface integral.

3.3.8. Determination of diffusivity using a simulated concentration profile generated from COMSOL.

Non-steady state concentration profiles were simulated using COMSOL v4.2 for use as a data set to test our method for the determination of the diffusion coefficient. Specifically, we simulated diffusion of a compound of fixed concentration into a 600 μm diameter circular structure with known diffusion coefficients. Three different control volumes were constructed within the structure along a radius at regular intervals where the concentration was determined. The diffusivity within the structure was fixed at a constant 1.0*10-9. The concentrations were obtained from each control volume resulting from the simulation and analyzed using our algorithm.

3.3.9. Optimization of size of control volumes.

To minimize the error associated with averaging a wide field of view, we varied the size of the control volumes to optimize an appropriate size that we can extend for use in the acellular and cellular situations. Normalizing all distances to the diameter of the circle (D), we ranged the length of the square control volume between 0.05D to 0.4D, while we varied the width of the adjacent control volumes between 0.0125D to 0.05D. The diffusion coefficients obtained using each control volume length, coupled with different the adjacent control volume widths at the inner most and outer most regions were normalized against

the original diffusion coefficient to yield an error between our simulation and the calculated value

3.3.10. Confocal microscopy and data processing of FITC-dextran (40kDa) diffusion into acellular GelMA of different rigidities.

A laser scanning confocal microscope was used to image the diffusion of FITC-dextran (40kDA) into the acellular GelMA hydrogels of 320 μm diameter. The hydrogels of varying concentrations of GelMA were used in this experiment (7.5%, 10.0% and 12.5%). FITC-Dextran was dissolved in PBS at 1mg/mL and infused into the device as the time lapse acquisition begun. The highest rate of capture (1 frame/2.1 sec) was used to acquire the fluorescent image of 1 z-plane, while the FITC-dextran diffused into the GelMA hydrogel. The acquisition was stopped upon reaching of equilibrium. A control volume with an xy-plane area measuring roughly 32x32 μm2 was constructed in the middle of the hydrogel, where the concentration profile was tracked over time. The average diffusion coefficient within this control volume was determined using the concentration data corresponding between when the concentration falls between 0.25 and 0.75 fold of the equilibrium concentration. This was done to minimize the influence of noise in the data at the beginning and end of the acquisition process.

3.3.11. Cell culture and spheroid formation

MCF7 cells were cultured on tissue culture plates in growth media containing high glucose Dubecco media with L-glutamine (Hyclone), 10% fetal bovine serum (FBS) (Gibco) and 1% Penicillin/Streptomycin (100U/mL) (Gibco). Culture media was changed

every other day and the cells were passaged using 0.25% trypsin-EDTA upon reaching 80% confluency.

To form spheroids, MCF7 cells were trypsinized and seeded into a non-cell-adherent petridish at a density of 250,000 cells/mL. They were then immediately placed onto a shaker with a rotation speed of 57 rpm in an incubator maintained at 37 °C and 5% CO2 for 663 days before use

3.3.12. Cell encapsulation and growth in GelMA

Spheroids cultured for 3 days on the shaker were filtered sequentially using cell strainers to retain the spheroids that ranged between 40-100 μm in diameter. These spheroids were then gently centrifuged at 50g for 4 mins to pellet them down, and then resuspended in GelMA solutions of different concentrations (7.5% - 12.5% wt/vol) containing 0.01% wt/vol ascorbic acid and 2 mM LAP. The spheroid-GelMA suspension was then infused into the microfluidic device, and a microscope was used to visualize the spheroid through a 320 μm diameter pinhole in a transparency photomask. Using the microscope stage, the spheroid was positioned in the center of the pinhole, and the GelMA solution was exposed to 12 seconds of collimated UV light. This resulted in the polymerizing of the GelMA in a 320 μm diameter column around the spheroid, thus encapsulating it. 3 spheroids were encapsulated for each device (Fig. 3.1). Unpolymerized GelMA-monomer was then rinsed out with infusion of growth media into the device. The device is then connected to a syringe through polytetrafluoroethylene (PTFE) tubing (cat no.: SWTT-26, Zeus) mounted to a syringe pump (Harvard apparatus model 55) delivering a maintenance flow rate of 40 μL/hour. Brightfield images of the spheroids were taken

daily for 7 days. ImageJ software was used to measure the area of the spheroid and quantify its growth. Spheroids encapsulated for 3 days were used in the packing density and diffusion imaging experiments.

3.3.13. Packing density analysis

3 days after encapsulation, the spheroids were used for analysis of the packing density of the spheroid. CellTracker Green (C7025, ThermoFisher Scientific) dye and Hoechst 33342 (14533, Sigma-Aldrich) was added to Opti-MEM (31985070, Gibco) to a working concentration of 14.8 μM and 2 μg/mL respectively. This solution was then infused into the device, and allowed to incubate for 45 minutes before washing with DMEM. Z-stack fluorescent images with 1 μm intervals of the dyed spheroids in the device were then acquired using the sectioning mode on the Keyence BZ-710 microscope. The image was then imported into MATLAB for further calculations. The channel stained with CellTracker Green would be summed to yield entire volume of the spheroid, while the channel stained with Hoechst would be summed to yield the volume occupied by the nuclei. The packing density would be obtained by dividing the volume occupied by the nuclei over the entire spheroid's volume.

3.3.14. Imaging of celltracker diffusion in MCF7 spheroid

The diffusion of a fluorescent dye, CellTracker, was infused into the device and the fluorescent signal was tracked using time lapse confocal microscopy at the highest frequency of acquisition. CellTracker dye was diluted to a working concentration of 14.8 μM in OptiMEM and introduced into the device as the time lapse acquisition was initiated.

Fluorescent images of a single plane of the spheroid was acquired every 2.1 seconds for a total duration of 20 minutes at which steady state concentration of CellTracker was reached in the spheroid.

3.3.15. Data analysis of CellTracker diffusion in spheroid

Concentrations of CellTracker were tracked and averaged in two equal sized control volumes with an xy-plane area measuring roughly 10x10 μm2; one in the middle of the cancer spheroid, and another roughly 10 μm from the edge of the spheroid. Concentrations from these two regions are then averaged and normalized to the highest intensities throughout the time lapse. The average concentration within these control volumes over time are then further fitted to a polynomial to obtain a smoother function for further analysis. This data was then analyzed as described using our algorithm.

3.4. Results

3.4.1. Characterization of 3D GelMA structures within the microfluidics device

The device, as described, yielded an inner chamber of height 80 μm (Fig. 3.2), as can be seen from the empty spacing between fluorescent beads embedded on the surface of the pAm hydrogels taken in the XZ projection of the chamber within the device. This distance would become the height of any of the GelMA hydrogels that were polymerized within the chamber. The external mechanical testing yielded the compressive moduli for the GelMA of different rigidities. The moduli were 7.7 kPa, 12.7 kPa and 18.6 kPa for the 7.5%, 10.0% and 12.5% GelMA concentrations respectively.

3.4.2. Simulation Results

The simulated COMSOL time dependent concentration profile using a region of constant diffusivity shows a radial inward increase in concentration over time as the molecule is diffusing in (Fig. 3.3 A-B). Based on an initial control volume width of 0.1D, and a adjacent control volume width of 0.1D, we obtained concentration profiles from which we took a temporal derivative to yield the rate of change of average concentration in each region, which is then plotted in Fig. 3.3C. Following that, the diffusion coefficient calculated for each time, and plotted in Fig 3.3D. From this, we can see that the diffusion coefficient eventually converged at 9.5*10-10. This average diffusion coefficient was then compared against the known coefficient, and the error associated with each calculation was determined. Our results show that our formulation for calculating the diffusion coefficient would be within a 5% error.

To further reduce this error, we ranged the central control volume between 5% to 80% of the diameter of the circle, as well as the size of the adjacent control volumes were varied, and the errors were recalculated using the same analysis. We found that the error was at a minimum when we used a control volume length of 0.1L and an adjacent flux window of 0.05L (Fig. 3.4, 3.5)

3.4.3. Spheroid growth within encapsulation of GelMA

From the brightfield images, we were able to track the growth of the spheroids over a period of 7 days (Fig 3.6), with the daily area of the spheroid plotted in Fig 3.7. Our results show that there was no effect of the rigidity of the matrix on the growth rate of the MCF7 cancer spheroid.

3.4.4. Packing Density

The packing density values of our spheroids were also determined by taking the ratio of the volume occupied by the nuclei of the cells to the volume occupied by the entire spheroid (Fig. 3.8) as is defined elsewhere (61). The initial packing density value of the spheroid obtained prior to encapsulation was 49.8%, while the other spheroids' packing densities post encapsulation ranged between 43% to 52% between day 2 and day 7. Overall, our results indicate that there is no statistical difference in the packing density of the spheroid over the different culture times (Fig 3.9).

3.4.5. Diffusion of FITC-dextran into acellular GelMA hydrogels

A series of pictures representative of the time lapse of FITC-dextran diffusion into the hydrogels are shown in Fig. 3.10. The average normalized concentration of FITC-dextran within an arbitrary control volume in the middle of the hydrogels is presented in Fig 4B. FITC-dextran permeated the softest 7.7 kPa GelMA hydrogel at a much higher concentration than the other 2 more rigid hydrogels. The concentration profile over time is presented in Fig. 3.11, where it is worth noting that the curve is less smooth in comparison to the data obtained from simulations. The average diffusion coefficient calculated is presented in fig 4C, and a clear observable statistical difference can be drawn between the softest 7.7kPa GelMA and the most rigid 18.6 kPa GelMA, with the % GelMA in between both.

3.4.6. Diffusion of Celltracker Dye into MCF7 Cancer Spheroid.

Representative images from the time lapse of CellTracker diffusion into the cancer spheroid is presented in Fig 3.13, showing the diffusion of CellTracker into the center of the spheroid over time. Using the average normalized concentration of CellTracker, we analyzed the diffusion coefficient at 3 regions similar to that of the simulation (Fig 3.14). In all 3 regions, the diffusivity is always highest for the spheroid encapsulated in the softest GelMA, though we only see a statistical difference in the coefficient in the core of the spheroid.

3.5. Discussion

Results obtained from testing of the algorithm against concentration profiles obtained in simulations suggested that there is an optimal control volume size with which an accurate value for the diffusion coefficient can be determined. In the first simulation, using a constant diffusion coefficient, it was observed that the bigger the control volume, the more accurate our algorithm was at predicting the diffusion coefficient. Furthermore, in this case, we did not observe any significant drawbacks with increasing control volume size. However, this trend was not reproducible in the second simulation. For a material of heterogeneous diffusivity, in this case, a material characterized by a linearly increasing diffusion coefficient, it was reported that our calculations using smaller control volumes tend to underestimate the actual diffusion coefficient while results determined with larger control volumes tend to overestimate the diffusion coefficient. Here, a control volume with a length of 0.1D appeared to be accurate in predicting the diffusion coefficient, yielding an error margin of no more than 20% in all cases tested. Considering that cancer cells are more

likely to be a material of heterogeneous diffusivity, we proceeded with the following steps using a control volume with a length of 0.1 in the xy-plane.

Spheroids encapsulated within the GelMA hydrogels exhibit a relatively linear growth trend in the first 7 days, with the spheroid in the softer 7.5% GelMA capable of growing slightly faster than its counter parts cultured in the 10% and 12.5% GelMA hydrogels. This is possibly due to the increased rigidity of the extracellular matrix, which could by mechanically resisting the growth of the spheroid. As there are slight disparities in the growth of the spheroids, we next investigated if the growth of the spheroids would impact the packing density of the cancer cells, as studies have shown that more tightly packed 3D cancer models have higher resistances towards diffusion. However, our results have shown that there are almost no differences between the packing density of the spheroids cultured in the softer GelMA and the packing density of the spheroid cultured in the more rigid GelMA.

The first application of our algorithm was done in experiments observing the diffusion of 40kDa FITC-Dextran into acellular GelMA hydrogels of different rigidities. We observed a predictable trend where the more concentrated GelMA hydrogels corresponded to a lower diffusion coefficient. It is also worth noting, as can be seen from the concentration curve, that the concentration of 40kDa FITC-dextran in the hydrogel at equilibrium decreases as the concentration/rigidity of the GelMA increases. This is due to the decreasing volume of free space within the hydrogel with increasing GelMA concentration, leading to a lower partition coefficient within the more rigid hydrogels.

CellTracker was used in our cellular experiments as a method of tracking diffusion of molecules through the spheroid due to its low cytotoxicity, high fluorescent signal

retention over time and its biochemical properties; It permeates the cell membrane readily, and the ester groups within the rings are hydrolyzed rapidly by esterases in the cytosol to yield fluorescein, which is similar in molecular weight to the CellTracker precursor. This was important as significant changes in molecular weight would alter the diffusion coefficient of the molecule. Thus, by utilizing a molecule where the hydrolyzed fluorescent product was of a similar molecular weight, we were able to make the assumption that both reactant and product had similar diffusion coefficients. However, by using CellTracker in accordance with the manufacturer's protocol, and with the use of low powered lasers on the confocal microscope to minimize the cellular exposure to damaging radiation, our results contained a significant amount of noise. To resolve this, the average concentration profile over time was fitted to a polynomial curve, of which the polynomial projection was analyzed using our algorithm. The goodness-of-fit was calculated with the R-squared value, and the high values (>0.9) was indicative of a good fit.

The results of our cellular experiments have determined that the difference between the diffusivities of the spheroid is spatially dependent. Like in our simulations, we chose 3 different regions, right in the center of the spheroid (r0), halfway between the center and the radius of the spheroid (r1) and at the radius of the spheroid (r2) for determining the diffusivity. The diffusivity between the rigidities is not statistically different at the regions r1 and r2, but it was significantly higher right in the center of the softer spheroid in comparison with the two stiffer spheroids. However, we do not see the general trend of an increasing diffusivity as we approach the center of the spheroid in the other 2 spheroids encapsulated in stiffer environments, which eliminates the possibility that this increase in diffusivity is hypoxia linked. One possibility is that despite not seeing a difference in the

growth rates of the spheroids, nor any changes in the packing density, the intercellular stress experienced by the spheroid encapsulated in the softest GelMA hydrogel is lower than that experienced by the other spheroids encapsulated in the GelMA hydrogels of higher rigidity. One of the effects of this lower stress could manifest as a higher diffusion coefficient in the spheroid encapsulated in this hydrogel.

3.6. Acknowledgements

The authors would like to thank all members of the Varghese lab at UCSD for their suggestions and fruitful discussions. We would also like to thank Anamik Jhunjhunwala for his help with the experiments. We would also like to acknowledge Jennifer Santini for assistance with microscopy and image analyses and UCSD as the primary source of funding.

Chapter 3, in full, is a reprint of the material is in preparation for submission to a scientific journal. “Quantifying Diffusivity amongst Cancer Spheroids Cultured in Matrices of Different Stiffnesses”. Lim, Han L.; Aung, Aereas; Varghese, Shyni. The dissertation author will be the primary investigator and author of this paper.

3.7. Conclusion

In conclusion, we have formulated and characterized a novel way of determining the diffusion coefficient of fluorescent molecules within cancer spheroids. This method was then tested against simulations generated using the COMSOL Multiphysics FEM package to optimize the resolution of the calculations by modifying the size of the control volumes in which the average diffusion coefficients can be obtained. Additionally, we

showed its utility in diffusion amongst acellular hydrogels and further tested it in the diffusion of CellTracker fluorescent dye in MCF7 spheroids cultured in GelMA hydrogels of different rigidities. In doing so, we have not only discovered that there is a difference in the diffusivity even within the spheroid, but we have also determined that the extracellular matrix plays a key role in modulating the diffusivity within the cancer spheroid. Such methods may be utilized in drug design as novel drugs are being discovered to help understand their transport capabilities within *in vitro* cancer platforms.

3.8. Figures

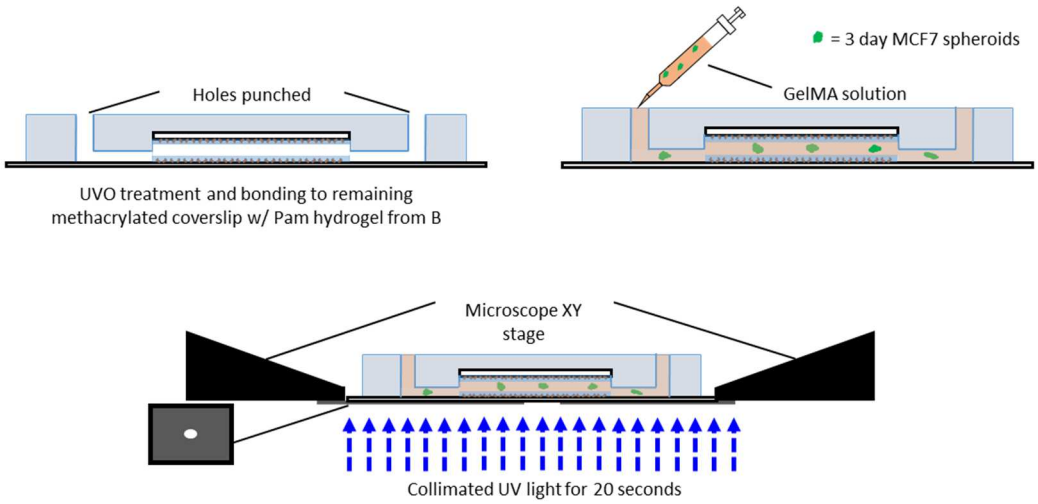

Figure 3.1: Schematic of the encapsulation of MCF7 Spheroids in the microfluidic device.

Starting with the fabricated microfluidic device, we infused a suspension of MCF7 spheroids in GelMA solution into its main chamber using a syringe connected to some tubing. The device is then mounted onto a microscope stage where we can visualize singular spheroids through a hole in a photomask through the lens of the microscope. Upon finding an isolated spheroid, collimated UV light is projected through the hole to polymerize the GelMA solution around the spheroid, thereby trapping it.

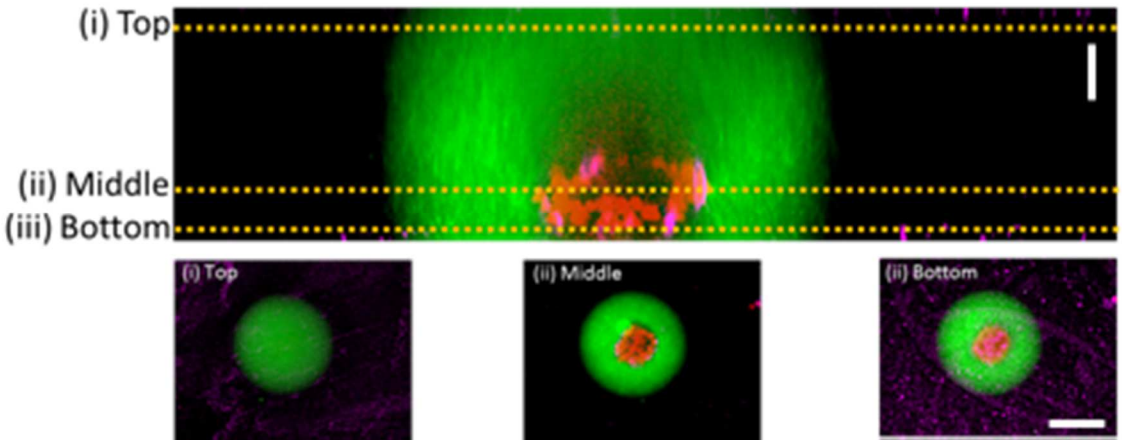

Figure 3.2: Z-stack image of the encapsulated spheroid

A z-stack image of the encapsulated spheroid is presented in the figure on top. An x-y plane of the figure along the dotted lines is presented in the bottom row. The left most figure represents the top x-y plane, the middle figure represents the middle of the gel and the right most figure represents the lowest dotted line. Vertical scale bar: 20 μm. Horizontal scale bar: 200 μm.

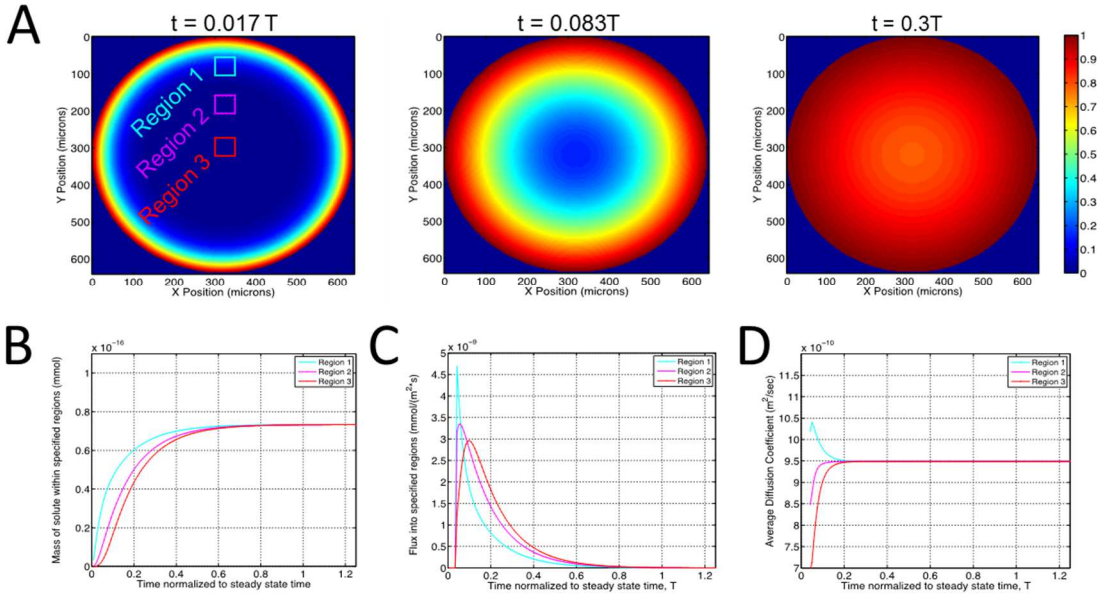

Figure 3.3: Simulation of diffusion within a disk

(A, top row) Time lapse of a simulated concentration profile of a known molecule throughout the disk for which D = 1e-9. Letting T be the time when steady state is reached, the top row shows the concentration profile at 0.017T, 0.083T and 0.3T respectively. In the top left, 3 boxed regions along the radius of the disk highlight regions of which we are trying to determine the diffusion coefficient for. (B) Total concentration profiles for each region. The cyan line represents region 1, the purple line represents region 2 and the red line represents region 3. (B) The total flux into each of the regions, with the cyan line representing region 1, the purple line representing region 2 and the red line representing region 3. (C) Determination of the diffusivity in the disk. Here we were able to obtain the values with a 95% percent accuracy, yielding a value of 9.5e-10 in comparison to the assigned value of 1e-9.

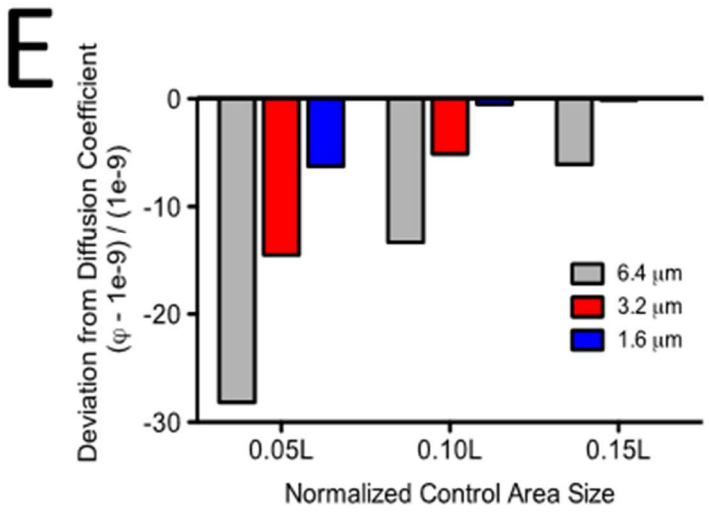

Figure 3.4: Determination of optimal region size while keeping the flux regions the same size.

We ranged the sizes of all 3 regions (region 1 in blue, region 2 in red and region 3 in grey) in which we determine the diffusivity for. The length of the region where we perform the calculation for is normalized to the diameter of the spheroid, denoted L. For a region box length of 0.05L, we see large errors in our predicted value, ranging from 5% in the inner core to 30% in the most radially distal region. As the region size is increased to 10% of the diameter, we see the error half, with the most external region around 15%, with the error in the core with a value of ~1%. The error values further diminished as we increased the region size to 0.15L, with region 1 and 2 with >1% error, and ~5% error in the most distal region 3.

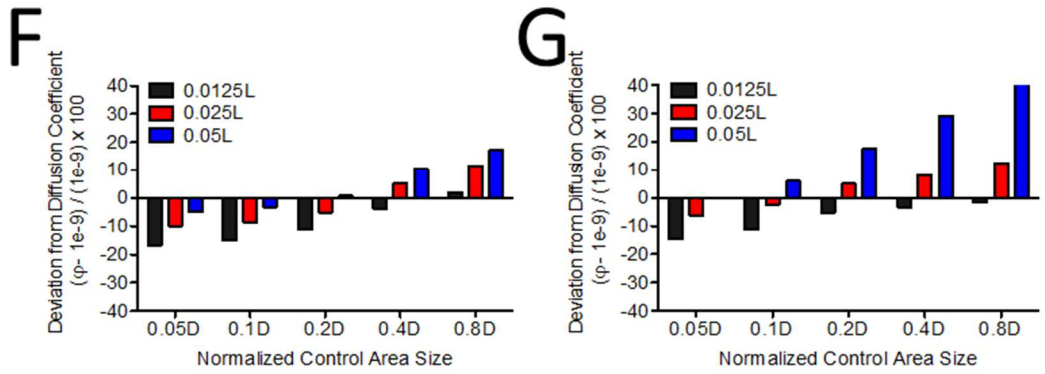

Figure 3.5: Determination of optimal region size for the control volume and flux windows.

(F) The error associated with our calculation of the diffusion coefficient in region 1. The control area size ranges from 0.05D to 0.8D, while the length of the flux window ranges from 0.0125L to 0.05L. (G) the error associated with our calculation of the diffusion coefficient in region3. The control area size ranges from 0.05D to 0.8D, while the length of the flux window ranges from 0.0125L to 0.05L.

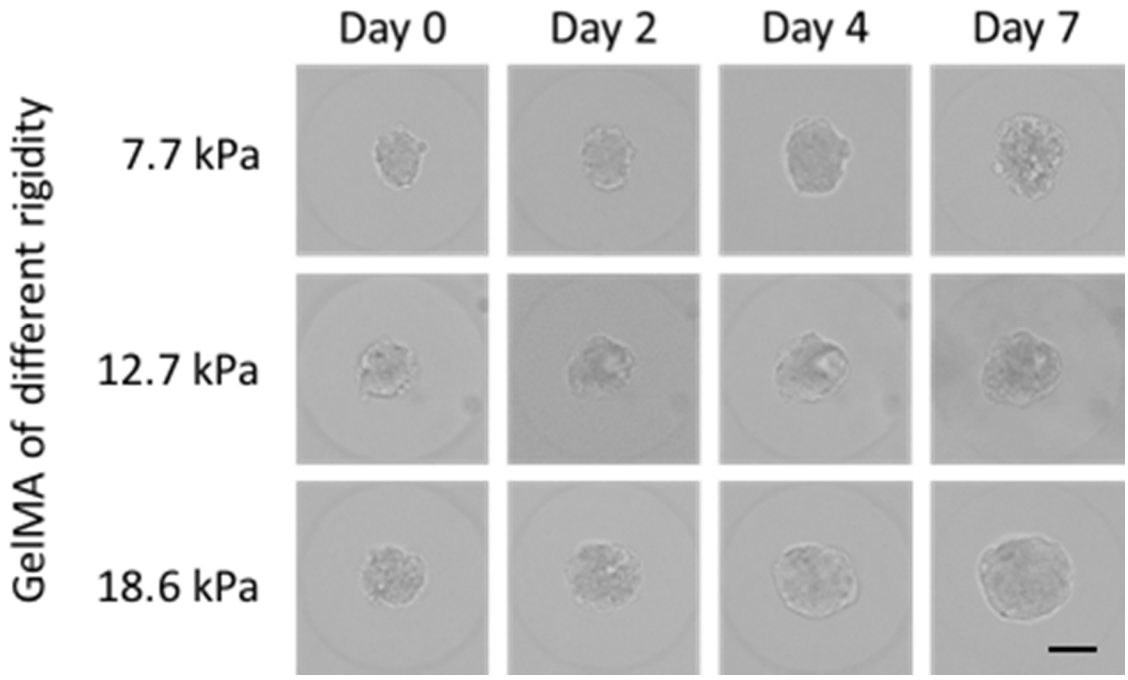

Figure 3.6: Brightfield images of the MCF7 cancer spheroid over 7 days in GelMA matrices of different stiffnesses.

MCF7 cancer spheroid growing in GelMA of different stiffnesses: 7.7 kPa GelMA (top row), 12.7 kPa GelMA (middle row) and 18.6 kPa GelMA (bottom row) from day 0 to day 7. Scalebar denotes 100 μm.

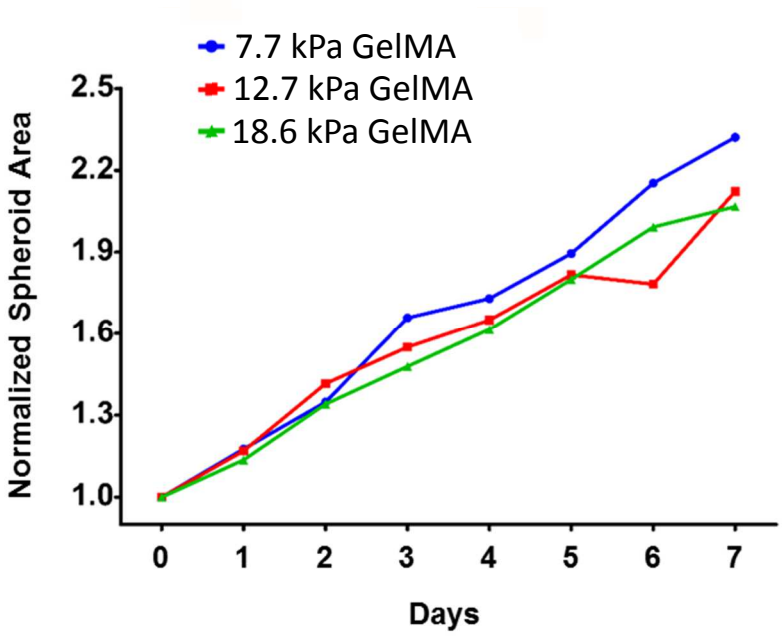

Figure 3.7: Normalized spheroid area from day 0 to day 7 in GelMA matrices of different stiffnesses

The graph plots the area of MCF7 spheroids normalized to the day 0 size when encapsulated over 7 days in 7.5% (blue), 10.0% (red) and 12.5% (green) GelMA.

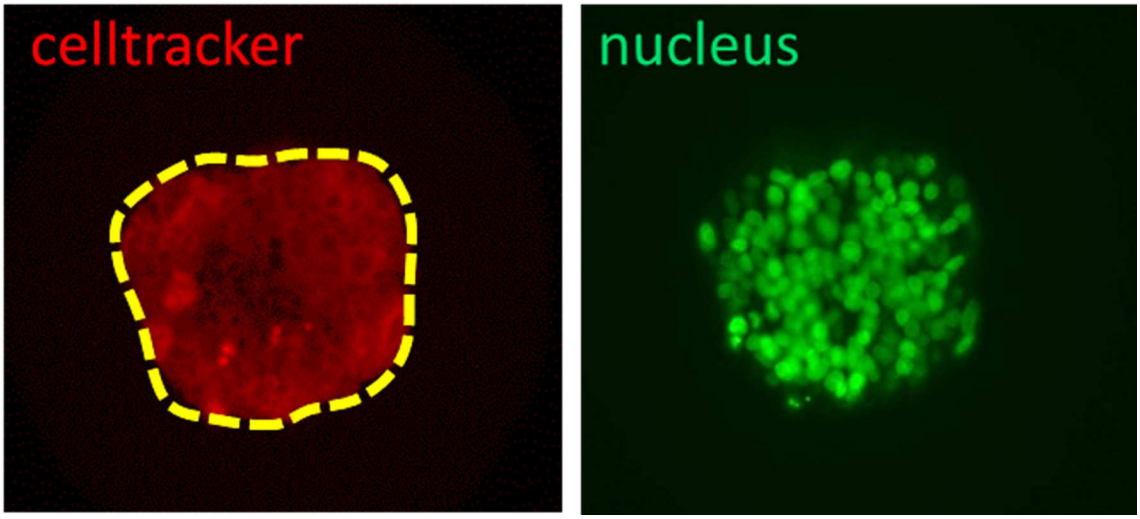

Figure 3.8: Celltracker and hoescht dye permeating into the spheroid

(left) Celltracker dye permeating into the MCF7 cancer spheroid. The outline of the spheroid is denoted with the dotted line. (right) Hoescht nuclear dye permeating into the same MCF7 spheroid.

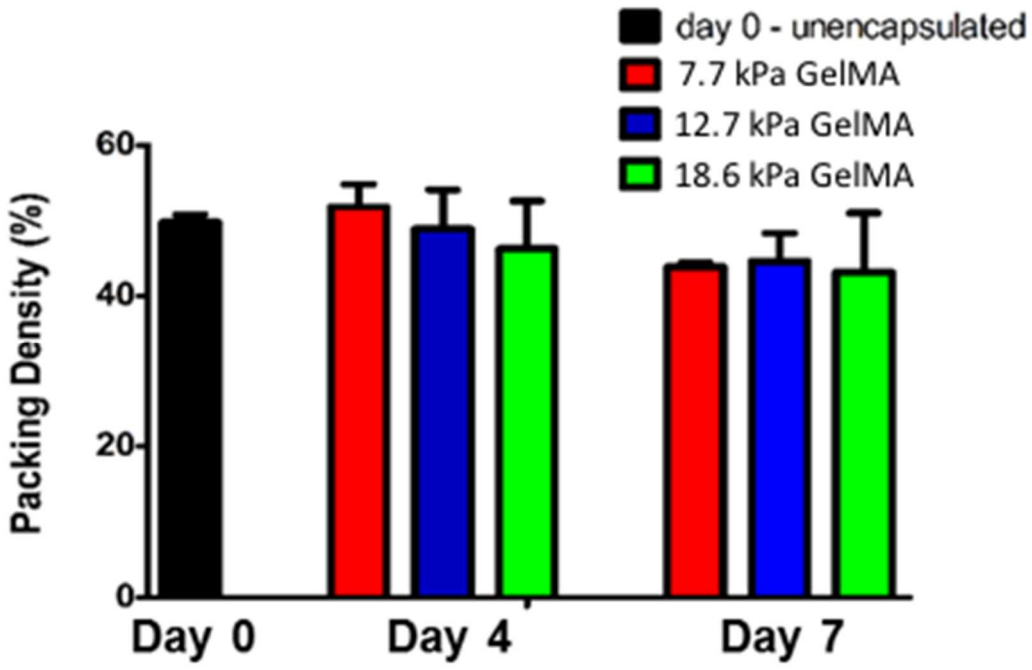

Figure 3.9: Determination of packing density in spheroids encapsulated at different GelMA concentrations.

The packing density of the MCF7 cancer spheroids at different GelMA concentrations remains statistically unchanged over time despite differences in the stiffness of the GelMA around it.

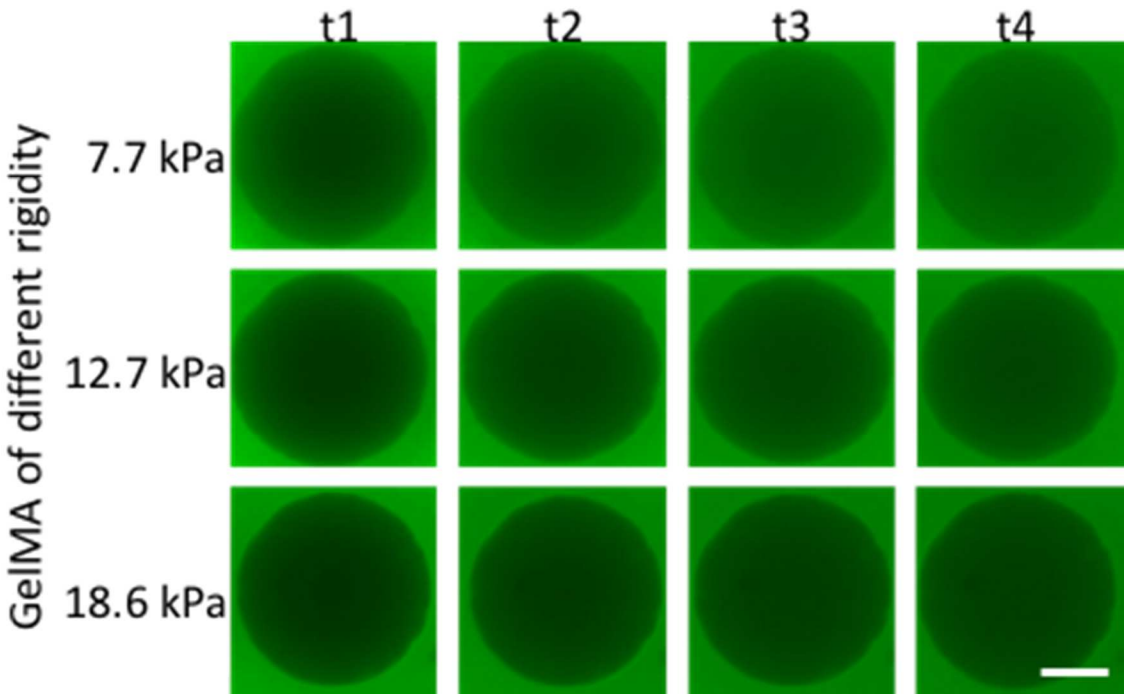

Figure 3.10: Diffusion of 40kDa FITC-dextran into acellular GelMA gels.

Diffusion of fluorescent 40kDa dextran molecules into acellular GelMA matrices of different stiffnesses (7.7 kPa - top, 12.7 kPa - middle, 18.6 kPa - bottom). Scalebar denotes 100 μm.

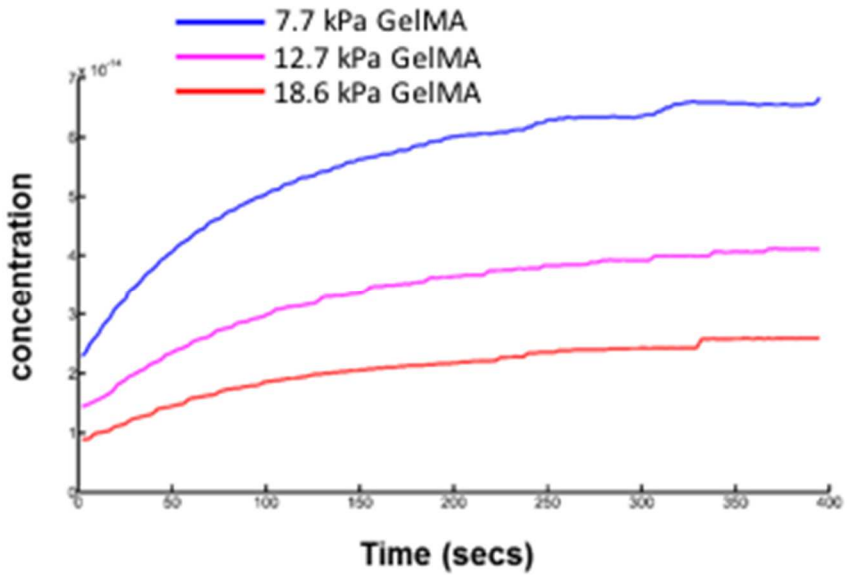

Figure 3.11: The concentration profile of FITC-dextran over time for the middle of the GelMA matrices of different concentrations.

The concentration profile of FITC-dextran was obtained by tracking the intensity of the fluorescence in the center of GelMA hydrogels of different stiffnesses over time (7.5% GelMA – blue, 10.0% GelMA – purple, 12.5% GelMA – red)

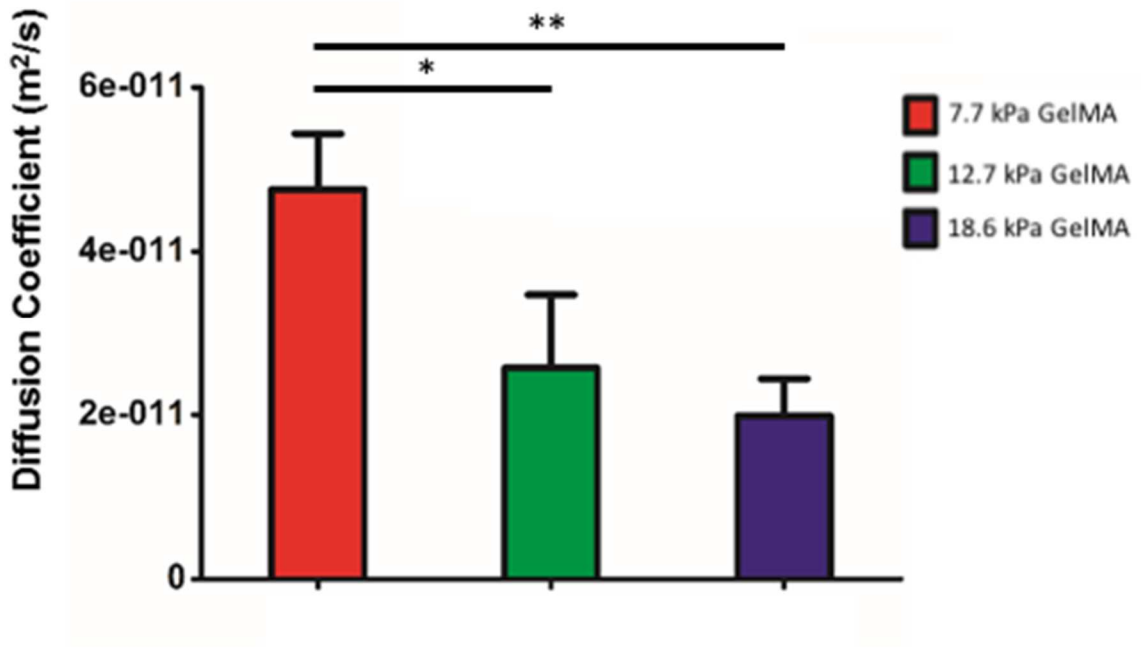

Figure 3.12: Determined diffusion coefficient of each hydrogel.

We determined the diffusion coefficient of each hydrogel using the same method as applied in the simulation. The diffusivity of FITC-dextran within the hydrogels of different stiffnesses decreases with increasing stiffness.

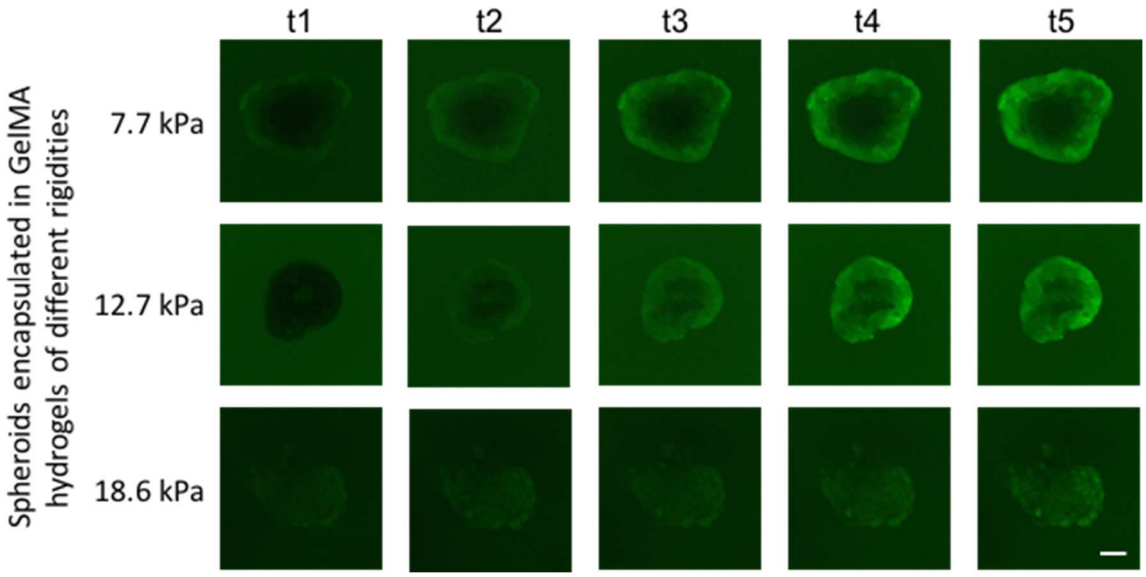

Figure 3.13: Celltracker diffusion into spheroids encapsulated in GelMA hydrogels of different rigidities.

The diffusion of celltracker into the spheroid slows down as the rigidity of the GelMA increases. Representative images were obtained at the same time points for spheroids in each rigidity. Scalebar denotes 40 μm.

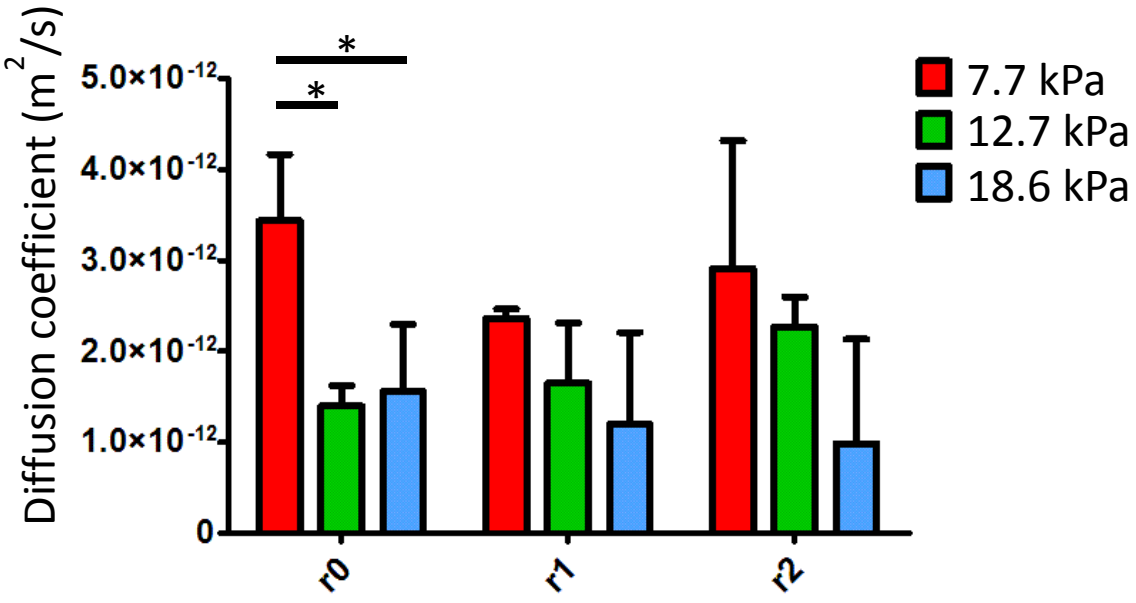

Figure 3.14: Diffusion coefficient of the spheroid at each region of interest.

The diffusion coefficient for each rigidity at different regions were calculated (r0 = center, r1 = 0.5 radius and r2 = at the outer radius of the spheroid). The diffusion coefficients for the spheroid grown softest 7.7 kPa gel appeared to be higher than the others, though it was only statistically significant in the most inner core of the spheroid.

Chapter 4: The development of an integrated multi-organ organ-on-a-chip platform

4.1. Abstract

Over the years, organ-on-a-chip technology has attracted much attention for its ability to recapitulate basic functions of organs within small microfluidic chips, making them excellent test beds for novel drug compounds (23, 25, 89, 99, 106, 107). Furthermore, they have the potential to be integrated together to allow the same media to perfuse through different types of organ-on-a-chip platforms, effectively mimicking systemic circulation in the body, and overall allowing us to recreate whole human physiologies *in vitro* (23, 94, 99, 104, 107, 110). However, only a handful of studies have combined multiple organ-on-a-chip platforms together due to inherent difficulties such as conflicting media conditions, etc (115, 116, 134). To this end, we demonstrate a proof-of-concept integrated organ-on-a-chip device can be linked together and ongoing viability over the short term of 7 days. Furthermore, we show each tissue retaining their characteristic function: Liver – metabolism and albumin secretion, cardiac – beating, muscle – myotube formation and cancer – continual growth, in this integrated system. To demonstrate how patient specific cells can be used in these systems, we have differentiated beating cardiomyocytes from induced pluripotent stem cells that possess the same genomic library as the person it was isolated from. As more organ-chips are created from patient derived cell sources, we will be able to integrate them to create "you-on-a-chip" – a multi-organ patient-specific *in vitro* platform to completely reflect the patient's own physiology.

4.2. Introduction

In the past decade, scientists have worked on *in vitro* microphysiological systems that transcend 2-D cell culture by integrating material science, mechanical and chemical engineering to recapitulate higher order functions exhibited by tissues and organs (22, 90, 94, 104). These systems have been touted to succeed animal models in drug testing, as they may be proven to be more relevant to human physiology, considering that their cell sources come from humans (23, 94, 110). Additionally, such microphysiological platforms allow us to circumvent diffusion limitations seen in larger tissue samples due to its smaller size, and also use less volume to achieve the same effect, thereby saving reagents and money in the long run.

One such example is the lung-on-a-chip system where Ingber and colleagues have elegantly incorporated the mechanical aspects of the expansion of the lung with the dual layer cell culture reflecting alveolar epithelial cells on one side and blood vessel endothelial cells on another (22, 94). They have also demonstrated that these cells can interact even with immune cells that is flowed through the device as bacteria is introduced into the "alveolar region". These immune cells injected into the device from the "blood vessel" layer can attach themselves onto the endothelial wall lining and transmigrate through the different layers to kill the bacteria.

These organ-on-a-chip devices can even be built using induced pluripotent derived cells, such as Healy and colleagues' heart-on-a-chip model, where iPSC derived cardiomyocytes were cultured for 3 days in the device and exhibited continual beating (99). Another prominent example is the liver on a chip device designed by Schepers et al. where iPSC derived hepatocytes were injected into a microfluidic platform (92). Such platforms

may eventually find use in personalized medicine where a patient's own cells can be biopsied, made pluripotent, expanded and then differentiated into many different types of cells that contain his own genomic data (25, 90, 107, 116). Drugs tested on these patient specific platforms have been suggest to reflect the patient's own response to different compounds, and hence can be used as an indicator for drug toxicity or efficacy.

However, despite the emergence of many such platforms, few have attempted to integrate multiple organ-on-a-chip systems to examine organ-organ cross talk (115, 116, 134). One big challenge to such integration experiments is the vastly different culture conditions that each organ needs to be subject to in order for the cells to function as they should . In one instance, Shuler and colleagues have devised a multiple-organ-on-a-chip platform that creates different types of tissues in different wells perfused by the same media. Within this platform he plated cell lines originating from liver hepatocarcinoma, bone marrow myeloid cancer and colon cancer, which are cells with common culture conditions. Cross-talk between the liver cells and the cancer was observed as Tegafur, an prodrug form of 5-fluorouracil was introduced into the culture (115).

Here in this chapter, I will go over the first steps to successfully integrating multiple organ-on-a-chip platforms together to achieve a culture condition that allows for cohesive viability amongst the cells. In this study, we have integrated organ-on-a-chip platforms with tissues belonging to heart, muscle, cancer and liver. We further characterize the functionality of each tissue, such as albumin secretion in the liver, cardiac beating in the heart. We also demonstrate how induced pluripotent stem cells (iPSCs) can be integrated, by using iPSC derived cardiomyocytes for our heart-on-a-chip platform.

4.3 Materials and Methods

4.3.1. Fabrication of Silicon Mold

Micropatterned silicon molds were fabricated according to the protocol as described previously. In brief, microfluidic channels were photolithographically defined using NR9-1500PY negative photoresist (Futurrex, Frankling, NJ, USA) on a 4-inch diameter Si wafer. The Si wafer with the photoresist defined was then etched using the deep reactive ion etching (DRIE) process. In the DRIE process, SF6 gas was flowed at 100 sccm throughout the 11 seconds of reaction time, followed by a passivation cycle when C4F8 gas was flowed at 80 sccm for 7 s. A 75 μm of etching depth was achieved under the etching rate of about 0.7 μm per cycle. After the DRIE process, the NR9-1500PY photoresist was removed by immersing in acetone for 4 hours before rinsing with methanol, isopropanol, and deionized water. The Si mold was then dried under compressed nitrogen gas and silanized by vapor deposition of trichlorosilane (TCI Inc, Portland, OR, USA) to facilitate PDMS molding and removal.

4.3.2. Fabrication of the Microfluidic Device

The microfluidic device was fabricated with minor modifications from a previous protocol (100). Once assembled, the device will contain a trilayer hydrogel system where cancer spheroid-laden GelMA hydrogels are sandwiched between thin polyacrylamide (pAm) hydrogel sheets. The fabrication and assembly is described as follows:

Methacrylation of cover glass

Cover glass on which thin pAm hydrogels were synthesized were functionalized with methacrylate groups to allow for chemical tethering of hydrogels containing vinyl groups. This was achieved by treating cover slips with a silanizing solution comprised 1.9mL ethanol, 60 µL of 10% glacial acetic acid and 40µL of 3-(Trimethoxysilyl)propyl methacrylate (cat no.: 440159; Sigma Aldrich) for 5 minutes at room temperature. The surface modified cover slips were then washed by submerging into pure ethanol with gentle stirring for 10 minutes several times before drying at 50 °C for 5 minutes. The cover slips were then used immediately.

pAm hydrogel formation

Thin sheets of pAm hydrogels were formed on 24x50 mm rectangular and 12 mm diameter round methacrylate-functionalized cover slips. This was done by first mixing a pAm hydrogel precursor solution comprising 4% (w/v) acrylamide (cat no.: A3553; Sigma Aldrich), 0.2% (w/v) bis-acrylamide (cat no.: 146072; Sigma Aldrich), 0.1% (w/v) ammonium persulfate (APS) (cat no.: A3678; Sigma Aldrich), and 0.1% (v/v) N,N,N',N'-Tetramethylethylenediamine (cat no.: T9281; Sigma Aldrich) in PBS. 5 µL of this solution was then immediately pipetted onto the middle of the 24x50 mm rectangular cover slip and covered immediately with an untreated 12 mm diameter cover slip. The resulting coverslip containing the hydrogel forms the base onto which the polydimethylsiloxane (PDMS) device can be bonded on. Similarly, 5 µL of this solution was also immediately pipetted onto the middle of the 22x22 mm untreated square cover slip and covered immediately with the methacrylated 12 mm diameter cover slip. Both pAm hydrogels were left to form

for 30 minutes at room temperature in a humidity chamber before removal of the untreated cover slips, leaving only pAm hydrogel disks tethered to the methacrylated surfaces of the cover slips.

PDMS molding and bonding

A 5 μL droplet of DI water was first pipetted on the circular region of the fabricated silicon mold before the pAm hydrogel-tethered cover slip was placed on it, with the hydrogel surface down. PDMS (Sylgard 184, Ellsworth Adhesives) polymer solution was mixed with its curing agent at a ratio of 10:1 by mass and degassed under vacuum to remove bubbles from the mixture. The PDMS solution was then slowly poured onto the wafer containing the cover slips and baked at 55 °C for 2 hours. The cured PDMS is then detached from the wafer, along with the hydrogel-tethered cover slip embedded on the inner surface.

Bonding of PDMS to glass coverslip

The PDMS obtained from the previous step and the methacrylated glass coverslip with a polyacrylamide hydrogel synthesized on it is submerged in 2-propanol and placed in a sonicating bath for 5 minutes to remove dust and other particles that may have attached to the surface. After sonicating, remaining 2-propanol on the surface of the PDMS and the glass cover slip is dried under compressed air and placed in a 80 °C oven for 5 minutes to remove remaining trace 2-propanol. After drying, the PDMS is then bonded to the pAm hydrogel tethered rectangular cover slip at 110 °C for 2 hours following UV-ozone treatment. Following the bonding of PDMS to the glass cover slip, we obtain a perfusable

microfluidic chamber whereby the top and bottom of the chamber is covered with thin pAm hydrogels.

4.3.3. MCF7, Huh7 and C2C12 Cell culture

MCF7, Huh7 and C2C12 cells were cultured on tissue culture plates in growth media containing high glucose Dubecco media with L-glutamine (Hyclone), 10% fetal bovine serum (FBS) (Gibco) and 1% Penicillin/Streptomycin (100U/mL) (Gibco). Culture media was changed every other day and the cells were passaged using 0.25% trypsin-EDTA upon reaching 80% confluency.

4.3.4. Spheroid Formation from MCF7 Cells

To form spheroids, MCF7 cells were trypsinized and seeded into a non-cell-adherent petridish at a density of 100,000 cells/mL. They were then immediately placed onto a shaker with a rotation speed of 57 rpm in an incubator maintained at 37 °C and 5% CO2 for 3 days before use

4.3.5. iPSC cell culture

Human induced-pluripotent stem cells (hiPSCs) were generously provided by Dr. Joe Wu and the Stanford Cardiovascular Institute. A 6-well plate was coated with Matrigel (Corning) overnight to make the substrate suitable for hiPSC attachment under feeder-free conditions. The cells were then plated in clusters and grown in mTeSR-1 (StemCell Technologies), a feeder-free maintenance medium. To ensure the cells retained pluripotency prior to differentiation, the hiPSC were split and re-plated several times. To

prepare for differentiation, hiPSCs were dissociated into single cells using a 15-minute treatment with 0.5mM EDTA in PBS. The cells were plated into a Matrigel-coated 12-well dish at a density of 150000 cells/well, then cultured in mTeSR-1 medium until the start of differentiation

4.3.6. Differentiation of iPSCs to beating myocardial precursors

Human iPSC were differentiated into myocardial precursors using a three-step protocol (135). The hiPSC were grown to 90-95% confluency before starting differentiation. The basal cardiac differentiation media consisted of 500µg/mL Albumax I Lipid-rich BSA (ThermoFisher) and 213µg/mL L-ascorbic acid (Sigma) in RPMI 1640 (11875, Gibco). Medium was changed every other day, within 1 hour deviation from the time of media change of the previous step. For day 0 – day 2, the medium was supplemented with 6µM CHIR99021 (Selleck Chemicals). On day 2, medium was changed to CDM3 supplemented with 2µM Wnt C-59 (Selleck Chemicals). From day 4 onwards, medium was changed to basal media every other day. Spontaneously contracting cells were noted around day 7, and by day 10 most of the well contained contracting myocytes.

4.3.7. Synthesis of lithium phenyl-2,4,6-trimethylbenzoylphosphinate (LAP) as a photoinitiator

To synthesize LAP, first, 2,4,6-trimethylbenzoyl chloride was added drop wise to an equal molar quantity of dimethyl phenylphosphonite under argon while stirring at room temperature. This mixture was allowed to react for 18 hours. Next, the temperature of the reaction mixture was increased to 50 °C while 4 molar excess of lithium bromide mixed

with 2-butanone was added to the reaction mixture. resulting in precipitation to form within 10 minutes. After precipitation, the temperature was cooled to room temperature and allowed to rest for 4 hours. Next, to ensure complete removal of excess lithium bromide, the precipitate was collected by filtration and washed three times using 2-butanone. Finally, the product was dried using a vacuum to remove excess 2-butanone, yielding LAP.

4.3.8. Synthesis of Gelatin Methacrylate (GelMA)

Gelatin was methacrylated in accordance with the protocol described elsewhere . In brief, 10g of bovine skin gelatin (Sigma Aldrich, St. Louis, MO, USA) was dissolved in 100 mL of PBS and stirred at 60 °C for roughly 1 hour to achieve complete solvation. Next the solution was lowered to 50°C, after which, 8mL of methacrylic anhydride (cat no.: 276685; Sigma Aldrich) was added to the solution drop wise with vigorous stirring. The solution was kept at 50°C with vigorous stirring for an hour after the addition was complete, after which, it is quenched with 2x the volume of PBS (200 mL). The solution was then dialyzed against milliQ water using 12–14 kDa cutoff dialysis tubing (Spectrum Laboratories, Rancho Dominguez, CA, USA) for one week (3 times per day water change) at 40 °C to remove trace contaminants. Next, the GelMA solution was frozen in liquid nitrogen and lyophilized in a freeze dryer for 4 days before being stored at −20 °C until usage.

4.3.9. MCF7 spheroid encapsulation encapsulation in microfluidic device

Spheroids cultured for 3 days on the shaker were filtered sequentially using cell strainers to retain the spheroids that ranged between 40-100 μm in diameter. These spheroids were

then gently centrifuged at 50g for 4 mins to pellet them down, and then resuspended in 10.0% (wt/vol) GelMA solutions containing 0.01% wt/vol ascorbic acid and 2 mM LAP. The spheroid-GelMA suspension was then infused into the microfluidic device, and a microscope was used to visualize the spheroid through a 320 μm diameter pinhole in a transparency photomask. Using the microscope stage, the spheroid was positioned in the center of the pinhole, and the GelMA solution was exposed to 12 seconds of collimated UV light. This resulted in the polymerizing of the GelMA in a 320 μm diameter column around the spheroid, thus encapsulating it. >3 spheroids were encapsulated for each device. Unpolymerized GelMA-monomer was then rinsed out with infusion of growth media into the device. The device is then connected to a syringe through polytetrafluoroethylene (PTFE) tubing (cat no.: SWTT-26, Zeus) mounted to a syringe pump (Harvard apparatus model 55) delivering a maintenance flow rate of 40 μL/hour for a day before integration with other organ-on-a-chip systems.

4.3.10. Huh7 encapsulation in microfluidic device

Huh7 cells were trypsinized from the tissue culture dishes and resuspended in 10.0% (wt/vol) GelMA solutions containing 0.01% wt/vol ascorbic acid and 2 mM LAP at a concentration of 2 million cells/ 100 μL GelMA. The cell-GelMA suspension was then slowly infused into the microfluidic device, after which UV light was shone through a photomask containing pinholes of 500 by 100 ellipses for 15 seconds. This resulted in the polymerizing of an array of GelMA ellipses. Unpolymerized GelMA-monomer was then rinsed out with infusion of growth media into the device. The device is then connected to a syringe through polytetrafluoroethylene (PTFE) tubing (cat no.: SWTT-26, Zeus)

mounted to a syringe pump (Harvard apparatus model 55) delivering a maintenance flow rate of 40 µL/hour for a day before integration with other organ-on-a-chip systems.

4.3.11. Formation of PAm mold patterns for cardiac and skeletal muscle tissues

To induce directional alignment of muscle tissues, polyacrylamide was used to create pillars (for skeletal muscle) and linear walls (for cardiac muscle). To do so, we employed a 3D photopatterning method described previously (Ref Shruti/Aereas paper). First, a precursor solution composed of 10% PEG-DA in PBS was prepared. The photoinitiator, LAP, was added at a concentration of 2mM, and the solution was perfused into the device. For linear walls, a transparency photomask with line patterns of 200µm width and 500µm separation was obtained and mounted onto the stage of a fluorescence microscope, centered over an open spot in the lens turret. The device was positioned on top of the pattern of the photomask, exposed to collimated UV light of approximately 365 ± 40nm excitation wavelength for 30 seconds. The regions of the hydrogel precursor solution exposed to the UV light polymerized, resulting in lines, which would act as “walls” to confine the cells longitudinally. Unreacted solution was removed by repeatedly washing with PBS. For pillars, the process was repeated using a transparency photomask with circular patterns of 200µm and inter-pillar distance of 500µm. Thus, the complete device was constructed with PEG-DA hydrogel walls and pillars for the two muscle tissues. The device was sterilized under UV light for 1 hour prior to cell encapsulation.

4.3.12. Encapsulation of C2C12 cells in microfluidic device

The C2C12 mouse murine myoblast cell line was obtained from ATCC. The cells were cultured in growth medium (GM), composed of Dulbecco's Modified Eagle's high glucose medium (Hyclone) supplemented with 10% fetal bovine serum (FBS, Gibco) and 1% penicillin/streptomycin (Gibco). The cells were grown to 70% confluency and passaged prior to usage in the experiments.

A 7% (wt/v) GelMA solution in PBS was prepared by dissolving the GelMA powder in PBS at 60°C for 30 minutes. This solution was syringe filtered with 0.22μm to remove contaminants and insoluble components. C2C12 cells were mixed into the GelMA solution at a cell density of 15 million cells/mL before adding 0.01% ascorbic acid (Sigma Aldrich), a free-radical scavenger, and 2mM LAP, a photoinitiator.

The cell-laden hydrogel solution was injected into the fluidics device with a syringe. A transparency photomask containing a capsule pattern was placed onto the fluorescence microscope as described previously. The device was mounted on the photomask and manually positioned to locate two pillars within the capsule shape using the microscope eyepiece under brightfield illumination. This region was exposed to UV light for 12-15 seconds to photopolymerize the GelMA solution containing the C2C12 cells. This process was repeated several times within one device to obtain up to 10 samples. Unreacted monomer solution and cells were washed away with sterile PBS. Thus, the 3D skeletal muscle-on-a-chip with cells patterned between and around anchoring pillars was created.

The samples were cultured in growth media for 24 hours, then switched to differentiation media, composed of Dulbecco's Modified Eagle's high glucose medium

(Hyclone) supplemented with 2% horse serum (HS, Omega Scientific) and 2% penicillin/streptomycin (Gibco), to induce cell differentiation and fusion. Media was supplied to the cells within the device through a syringe pump (Harvard Apparatus) at a constant flow rate of 40μL/hour in an incubator set at 37°C and 10% CO2.

4.3.13. Encapsulation of iPSC derived myocardiac cells in microfluidic device

Differentiated hiPSC were seeded into the microfluidics device. First, the UV sterilized device containing PEG-DA hydrogel walls was perfused with Matrigel and incubated for at least 2 hours to prepare the glass surface for cell attachment. Differentiated hiPSC-cardiomyocytes between day 12-18 of differentiation were dissociated with TrypLE solution (Gibco) for 15 minutes, then strained through a 70μm cell strainer to remove excess extracellular matrix. Cells were packed at a high density of 40 million cells/mL and infused into the Matrigel-coated device, then incubated at 37°C for 1 hour to allow for cell attachment. After hiPSC-cardiomyocytes had attached to the glass, unattached cells were washed away with multiple washes with both PBS and media. Samples were cultured in basal cardiac media supplemented with ROCK inhibitor at 2μM (Thiazovivin, Selleck Chemicals) and 30% knockout serum replacement (Gibco) for the first 2 days after cell seeding, after which the media was changed to basal cardiac media. Media was supplied to the cells within the device through a syringe pump (Harvard Apparatus) at a constant flow rate of 40μL/hour in an incubator set at 37°C and 10% CO_2.

4.3.14. Integrating different organ-on-a-chip devices with a peristaltic pump

A 3-inch long segment of platinum cured silicone tubing (ID 0.025", cat. no: 51845K67, McMaster-Carr) is autoclaved alongside other segments of PTFE tubing (26 gauge), and a PDMS disk with 2 1-mm holes punched through it (1 cm diameter, 0.5cm thickness). After the autoclave step, all components were stored under a germicidal UV lamp in the biosafety cabinet for further sterilization.

To integrate multiple organ-on-a-chip devices using the tubing, the stiffer PTFE tubing was inserted into the silicone tubing to join both segments of tubing together. This junction was sealed further with paraffin (parafilm, cat. no.: EF9896A). The elastic silicone was then looped tightly around the wheel of the peristaltic pump (cat. no.: EW-73160-30, Cole-Parmer) with the outlet tubing connected to a series of organ-on-a-chip microfluidic devices and the inlet tubing connected to a reservoir of media. As the peristaltic pump cycles, it draws up the media from the reservoir to inject it into the microfluidic devices, which is connected to the reservoir at the outlet so that fluid injected into through the microfluidic devices drains back into the reservoir to keep its volume constant. We connected the organ-on-a-chip devices in the order from the liver-on-a-chip, to the heart-on-a-chip, to the cancer-on-a-chip to the muscle-on-a-chip and then cycling the media back to the reservoir (Fig 4.1 – 4.3).

4.3.15. Characterization of flow through an integrated system

Characterization of the bulk flow rate across multiple chips

To determine the bulk flow rate of media through different numbers of chips, we connected a different number of chips (2, 3, 4 and 5) to the peristaltic pump, and varied the

settings on the peristaltic pump from 5 to 99. For each setting and number of chips, we collected the outflow from the series of chips for 5 minutes, to obtain an average flow rate in μL/min.

Time lapse capture of the peristaltic flow in each chip

For characterization of the peristaltic nature of the flow in each chip, we perfused fluorescent nanoparticles (FluoSpheres, cat. no.: F8811, ThermoFisher Scientific) suspended in DI water at 0.5% vol/vol through a series of 5 microfluidic devices. We next took turns mounting each device on a microscope with time-lapse capabilities and obtained a video of the flow.

Analysis of the peristaltic flow

The video obtained during the time lapse capture is then analyzed using a MATLAB script written in-house. First, the video is recompiled into a z-stack image, and converted into a binary image using a threshold of 2.5 times the average intensity of every pixel in the image; every pixel below the threshold was assign a value of 0 while every pixel above the threshold was assigned a value of 1. We next cleaned the image up using the built-in MATLAB function *bwareaopen*, to remove objects smaller than 10 pixels in the image, leaving us with a sparse number of objects left in each image in the z-stack.

To determine the displacement of these objects between each image in the z-stack, we used the built-in MATLAB function, *xcorr2*, to compare the current image with the very next image. This result yielded the shift in the x-y plane between the first and second

image, which we were able to use to obtain displacements between every 2 frames in the z-stack.

4.3.16. Growth analysis for the cancer-on-a-chip

Brightfield pictures of each cancer spheroid encapsulated within its GelMA hydrogel in the cancer-on-a-chip device was captured at every 24 hour intervals starting from day 0. From these images, the cross-sectional area of the cancer spheroid was obtained by tracing around the spheroid using ImageJ. Each cross sectional area was then normalized to the area obtained on day 0.

4.3.17. Albumin Assay

Sandwich enzyme linked immunosorbent assay (ELISA) was performed to assess the daily liver function by monitoring the secreted human albumin concentration over a 7 day period. In short, 1 ml of media was collected daily from the reservoir and frozen at -80°C for use in subsequent analysis. After 7 days of media collection, liver function was assessed via measurement of human albumin concentrations using the Human Albumin ELISA Quantitation Set (Bethyl Labs, Catalogue no. E80-129) according to the manufacturer's protocol.

4.3.18. Beating frequency and analysis

A time lapse video of iPSC derived cardiomyocyte beating was captured at 20 Hz everyday and analyzed in MATLAB to study its beating frequency. One of the frames during which the cardiomyocytes are in its relaxed state is used as a reference frame, with

which every other frame in the z-stack is compared to. To simplify this comparison, we summed the absolute value of the difference between the reference stack and the current stack. Using this method, images during which the cardiomyocyte sheet is relaxed would more closely resemble the reference stack would yield a sum that is closer to 0 in comparison with the contracted tense images. We then proceed to plot this summed value for the time span of the video.

4.3.19. Immunofluorescent staining for myosin heavy chain in myotube bundles and α-actinin and connexin 43 in the iPSC derived cardiomyocytes

To demonstrate the continual expression of tissue specific proteins after integrating multiple organ-on-a-chip platforms, we used immunofluorescent staining to get a qualitative conformation of the presence of these markers. For the muscle-on-a-chip device, we stained for myosin heavy chain (MF20), while for the heart-on-a-chip device, we stained for cardiomyocyte-specific α-actinin, as well as connexin 43 to indicate the presence of gap junctions through which membrane potentials are transferred. For this, PBS was injected through the device to rinse off remaining before before 4% paraformaldehyde (Sigma-Aldrich, cat#: 158127) was injected and incubated for 8 minutes. After that, blocking/permeabilizing buffer containing 0.1% Triton-X 100 (ThermoFisher Scientific, cat#: 28313) and 3% bovine serum albumin (Sigma-Aldrich, cat #5611) was injected into both devices for an hour at room temperature. After blocking, immunofluorescent antibodies, myosin heavy chain (MF20, Developmental Studies Hybridoma Bank) for the muscle-on-a-chip, and α-actinin and connexin 32 antibodies were diluted 1:100 in blocking buffer, and injected into each device. The antibody solution was

allowed to incubate for an hour at room temperature, before rinsing out with additional blocking buffer. Fluorescently labelled secondary antibodies that target the primary antibodies are then diluted 1:250 in blocking buffer and injected into each device, and allowed to incubate for an additional hour at room temperature before rinsing out with additional blocking buffer. The devices are then imaged under a fluorescent microscope to visualize the presence of the respective tissue specific markers

4.3.20. Live/dead assay for viability

To demonstrate viability in each chip, the Live/Dead assay for mammalian cells (cat. no.: L3224, ThermoFisher Scientific) was used, where upon staining, live cells will be labelled fluorescent green while dead cells would be labelled with fluorescent red. In brief, live/dead solution containing 1 μL of the EthD-1 stock solution and 0.25 μL of the calcein AM stock solution diluted up to 0.5 mL with Opti-MEM was prepared in accordance with the manufacturer's protocol. The chips to be stained were first injected with PBS to rinse of remaining media before the live/dead solution was injected into the device and allowed to incubate at 37 °C for 30 minutes to ensure complete permeabilizing into the tissue. After incubating, the remaining solution was rinsed off with an injection of PBS, and then imaged using a fluorescent microscope.

4.4. Results and Discussion

4.4.1. Acellular characterization of flow through the organ-on-a-chip platforms

Bulk flow characterization results

The overall flow rate for our set up ranges between 1 to 15 μL/min, which converts to 60 to 900 μL/hr (Fig. 4.4). As we increase the number of chips, in general, the flow rate decreases due to the increased resistance in the channels due to the additional length, except when the setting is set to the fastest pump rate of 99, where there is no difference regardless of the number of chips is placed in the loop. Since we have optimized our previous studies to utilize a flow-through rate of 40 μL/hr, we ran the peristaltic pump setup at a rate of 5.

Characterization of flow velocity

Our characterization of the flow velocity within each chip showed us that in the first chip, the flow velocity would spike at regular intervals to 7 μm/s within the first chip, in sync with when the peristaltic pump would inject a bolus of media into it. From the second chip on, we can see that the flow profile becomes smoother, and the oscillations become progressively more attenuated, slowly settling down to a smooth constant velocity flow rate of approximately 3 μm/s in the 4^{th} and 5^{th} chips in the chain (Fig. 4.5).

4.4.2. Viability and functionality of the liver-on-a-chip device after 7 days of integrated co-culture

In the first few days of the integration, many of the Huh7 cells migrated from within the GelMA hydrogel to the edge, lining the construct's perimeter. The cells then continue to grow in the hydrogel to form multicellular masses (Fig. 4.6). The structural integrity of the GelMA hydrogel was also visibly weakened, possibly in response to degradation by the Huh7 cells to accommodate its growth and migration. The device had ~95% viability after the same time of co-culture in the integrated device (Fig. 4.7), with dead cells

dispersed throughout each construct. We hypothesize that this cell death is due to starvation, as it would be difficult for the nutrients to diffuse in high concentrations into the middle of the multicellular spheroids.

4.4.3. Viability and functionality of the heart-on-a-chip device after 7 days of integrated co-culture

The heart-on-a-chip device was assembled using cells differentiated on 12-well plates, and was only integrated with the other devices after contraction was observed in a singular flow through device. After 7 days of integrated culture, the iPSC-derived cardiomyocytes remain confined to their strips in 2-D (Fig. 4.8). It was difficult to determine if the cells had proliferated, as the cell strips were already confluent before integrating with the other devices. However, the viability of the cells in the cell strip was poorer in the cardiomyocyte device in comparison to the cells from other devices (~85-90%) (Fig. 4.9), with the death cells homogenously distributed throughout the tissue. We hypothesize that this is due to the increased sensitivity of the iPSC derived cardiomyocytes to the culture conditions, in comparison to the other cell lines. By integrating the iPSC derived cardiomyocytes with other cells, the other cells are dynamically changing the components of the media, which may inadvertently affect the viability of the cardiomyocytes.

We also assessed the persistence of the differentiation of the iPSC cardiomyocytes through immunofluorescent staining. After 7 days of integrated co-culture, the cardiomyocyte strips stained positive for α-actinin, a marker for cardiomyocytes, connexin-43, a marker for the formation of gap-junctions through which ionic currents can flow

through to synchronize the contractions of the cells in the strip (Fig, 4.10). This attests that the integration of the heart-on-a-chip system does not negatively influence the phenotype of the differentiated cardiomyocytes over the culture period of 7 days.

Spontaneous contraction of the cell strip was also observed throughout the integrated co-culture period. We expressed this in terms of an average deviation from the relaxed state, which was plotted in Fig. 4.11. The beating frequency for each of the 7 days were obtained, which is then presented in Fig. 4.12. Before integrating into the device, the beating frequency was higher than in the integrated device. Immediately after integration, the measured frequency fell to 0.3 Hz at 24 hours and was undetectable at 48 hours. However, between day 3 to day 7, contraction of the cardiac strip resumed and stabilized around 0.5 Hz, which is still lower than before the integration. This suggests that the integration itself has an adverse effect on the beating, which can be affected by the culture media composition as well. We hypothesize that the co-culture in the integrated system would lead to a nutrient depletion overtime, which then resulted in the lower beating frequency of the cardiomyocytes observed here.

4.4.4. Viability and functionality of the cancer-on-a-chip device after 7 days of integrated co-culture

After encapsulation, the MCF7 spheroids showed continual growth within the device even after integration (Fig. 4.13). The cancer-on-a-chip retained the highest viability across the devices, with the viability close to 100% across all samples (Fig. 4.14). This growth is plotted in Fig. 4.15.

4.4.5. Viability and functionality of the muscle-on-a-chip device after 7 days of integrated co-culture

Like the heart-on-a-chip device, the cells in the muscle-on-a-chip device were first differentiated in flow-through device (known as the differentiation phase) before integrating into the co-culture with the other devices (hereby referred to as the integration phase). The differentiation phase lasted 14 days, where c2c12 cells were cultured with myogenic induction media, which led to the condensation of cells around the pillars, and the formation of cell masses that are dense and opaque (Fig. 4.16). The device is then integrated with the other devices in the second integration phase, which is the same 7 days as the rest of the device. After 7 days of co-culture, it was observed that the condensation is reduced, accompanied by the formation of some myotubes across the two pillars. This reversal of condensation of the c2c12 cells could be due to the change in culture condition, as the integrative media used was not myogenic induction media, but rather cardiomyocyte differentiation media.

At the end of the integration phase, a live/dead assay was performed, showing high viability (~95%) of the cells in the muscle tissue, with few dead cell interspersed across the construct. Successful differentiation of the c2c12 cells was also confirmed with positive immunofluorescent staining of desmin and MF20, both of which are muscle markers. Additionally, we also observed the formation of multi-nucleated myotubes, denoting that the c2c12 cells fused to form functional myotubes.

4.5. Acknowledgements

The authors would like to thank all members of the Varghese lab at UCSD for their suggestions and fruitful discussions.

Chapter 4, in full, is a reprint of the material is in preparation for submission to a scientific journal. "The development of an integrated multi-organ organ-on-a-chip platform". Lim, Han L.; Agrawal, Gaurav; Varghese, Shyni. The dissertation author will be the primary investigator and author of this paper.

4.6. Conclusions

Here we show the integration of many organ-on-a-chip systems in a modular fashion is viable for short periods of time. Each organ-on-a-chip system, after integration, continues to maintain its phenotype throughout this period of time. We also show that such systems can not only be used as connected separate bioreactors, but also as a platform on which migration, proliferation and differentiation of cells can be studied. Such systems can also be used to probe organ-organ communication, or study the effects of systemic conditions such as inflammation on many organs. This can also be used to study cancer metastasis, to see how cancer cells can migrate from tissue and then anchor themselves onto substrates for other tissues and form a secondary tumor at distant sites. In the future, these devices can even be used to promote personalized medicine, allowing us to tailor drug regiments to individuals to provide better healthcare.

4.7. Figures

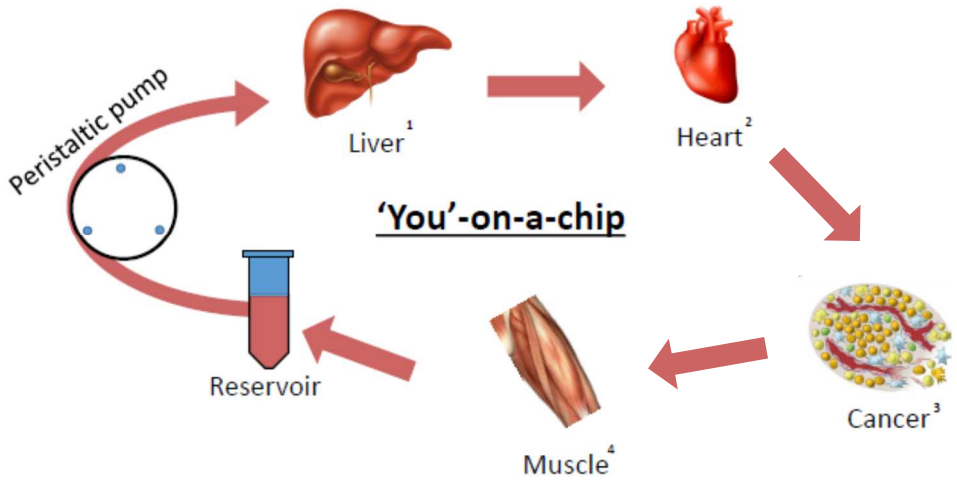

Figure 4.1: Schematic for integrating multiple organ-on-a-chip devices

In our setup, media is drawn in from a reservoir by a peristaltic pump and channeled firstly through the liver, following by the heart, cancer, and muscle in that order, before finally getting cycled back into the reservoir.

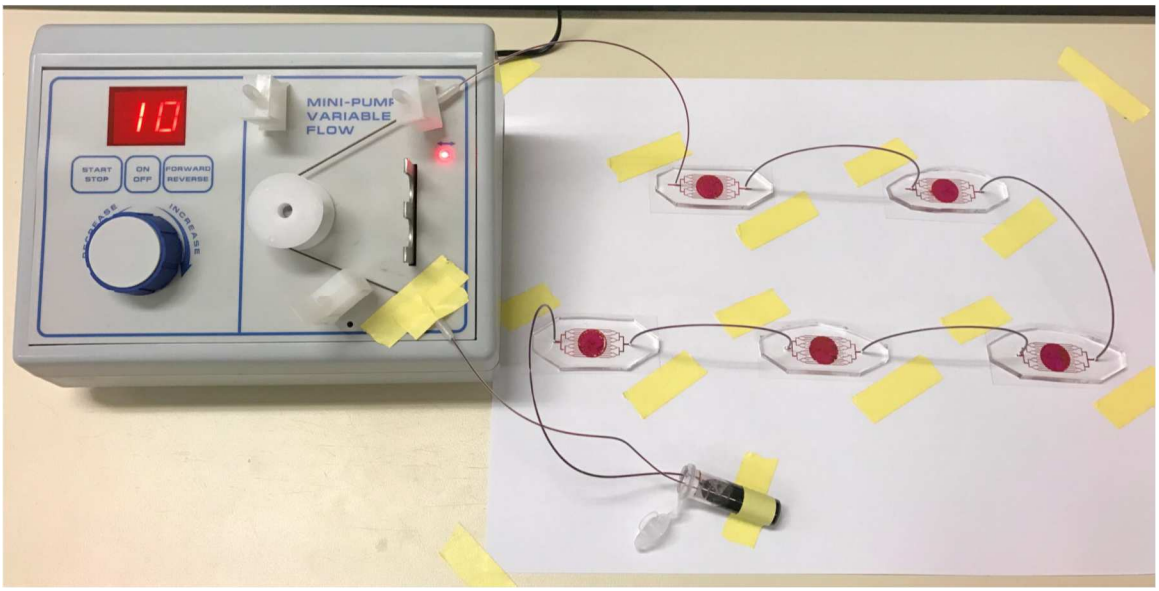

Figure 4.2: Actual set up of the integrated system

The actual set up mirrors our schematic, where media is drawn out from the reservoir and then pumped into a series of chips before it is being cycled back into the reservoir again.

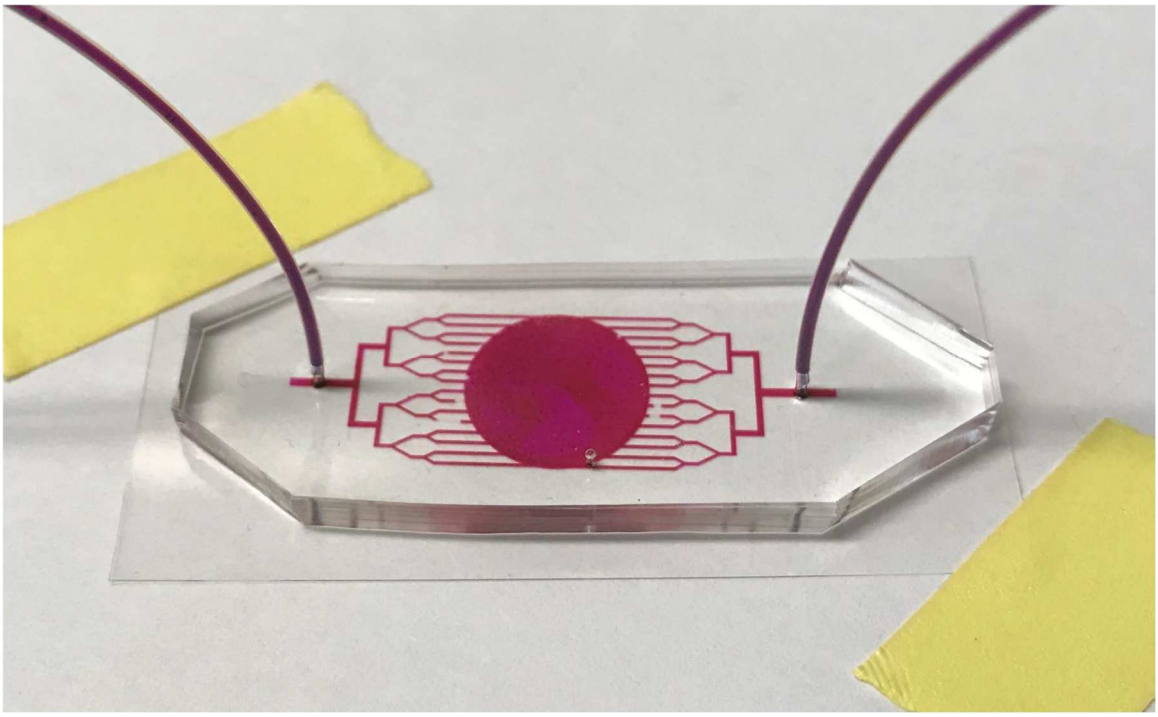

Figure 4.3: Close-up of one of the organ-on-a-chip devices within the series of devices

A close up, magnified picture of the organ-on-a-chip device. Each device measures 75 x 25mm, with a cylindrical culture chamber measuring 1.2 cm wide, 80 μm tall. The space of the whole chip occupies a volume of approximately 5-10 μL.

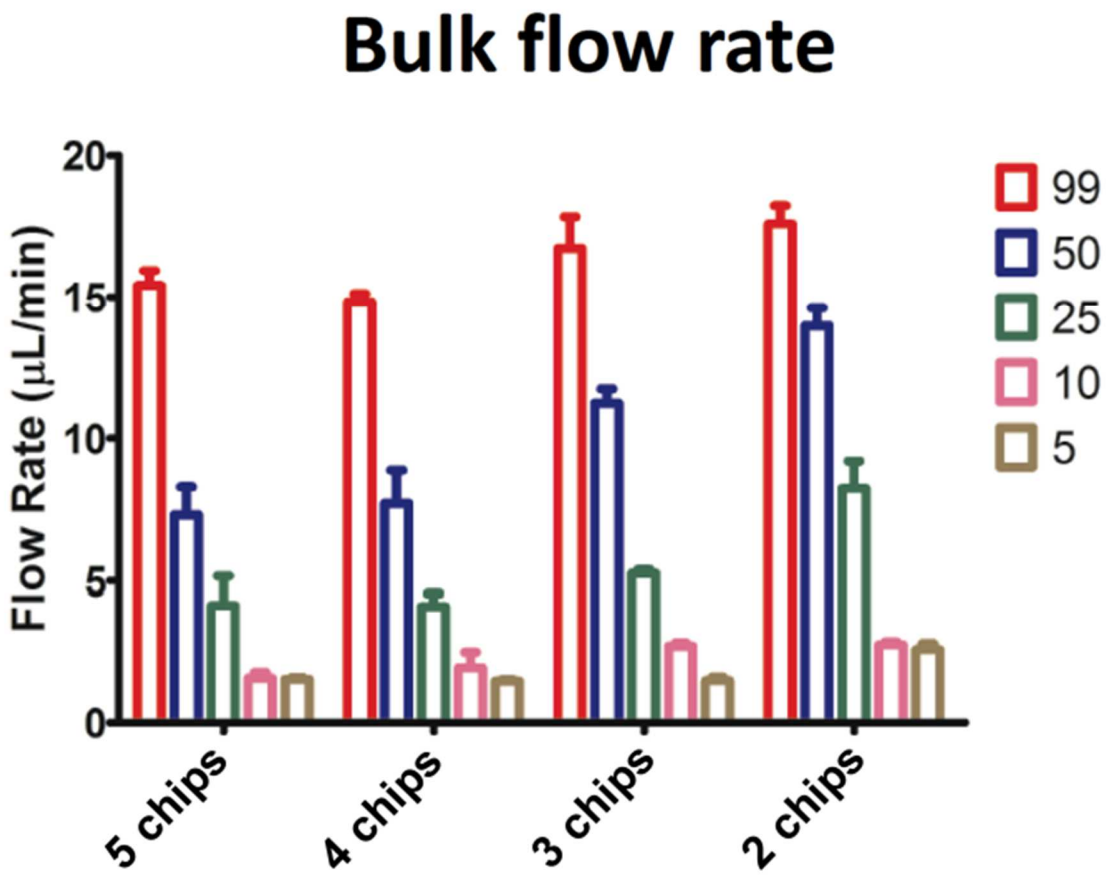

Figure 4.4: Bulk flow rate within the device

The flow rate of the chips ranges between 1-20 µL/min depending on how many chips were used and the setting on the peristaltic pump. As the number of chips increases, the total flow rate across all the chips decreases due to the increased resistance to the fluid flow. There was also no qualitative difference for settings less than 10 on the peristaltic pump.

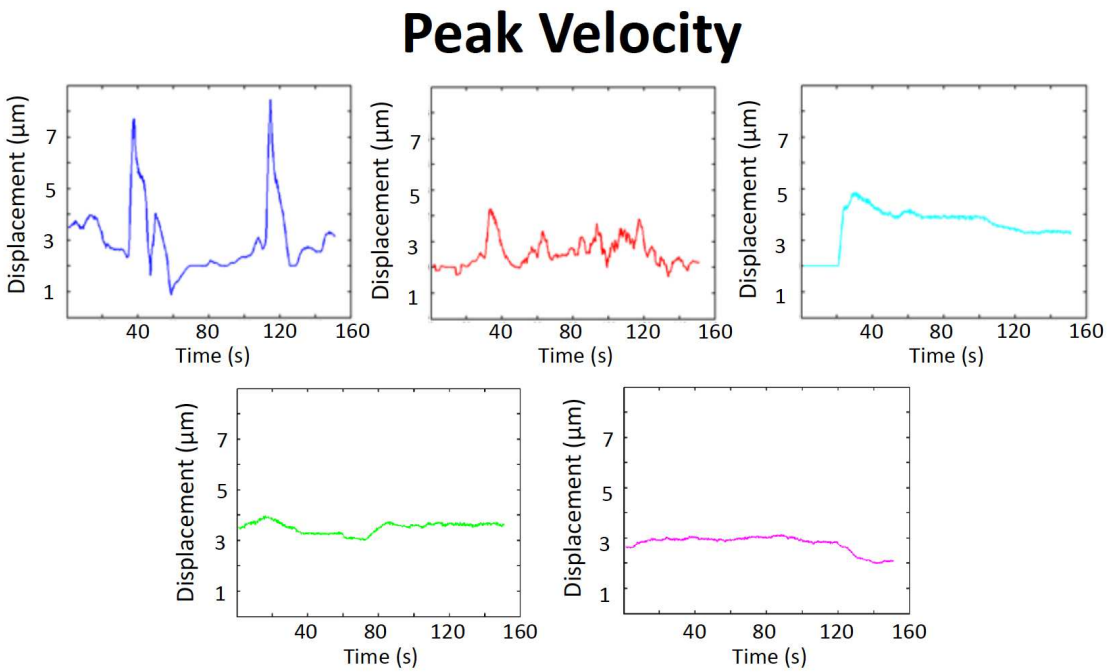

Figure 4.5: Velocity profile of the flow as determined by PIV

The velocity flow profile within each of the 5 chips, for when 5 chips are connected in series to the peristaltic pump. Due to the nature of the pump, there are large fluctuations in the velocity of the fluid in the first chip, that synchronizes with the rate at which the pump is cycling. As the fluid flows through the rest of the chips, the fluctuations become more attenuated and by chip 4 and 5, become almost a straight line.

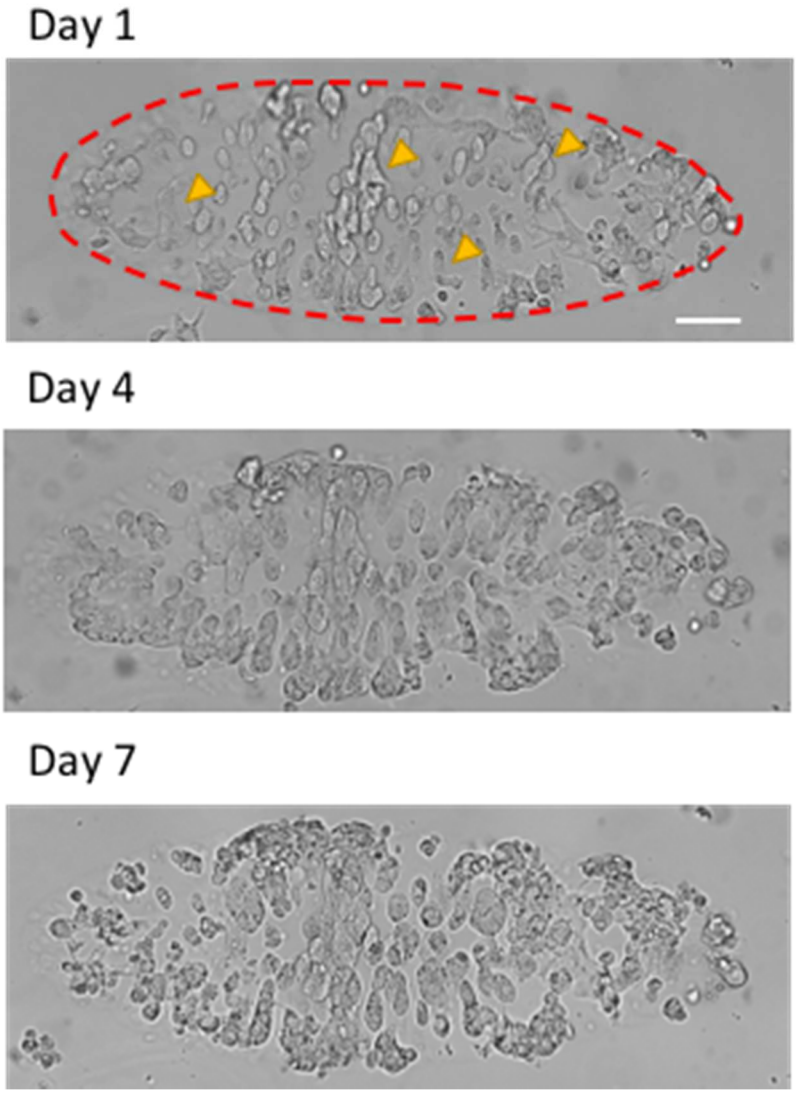

Figure 4.6: Brightfield images of encapsulated Huh7 cells growing for 7 days in the integrated device

Huh7 cells were observed to be lengthening width-wise and migrating to the edge of the GelMA hydrogel (indicated using red dotted lines). Some of the lengthening cells are indicated with the orange arrow heads. Scale bar denotes 100 µm

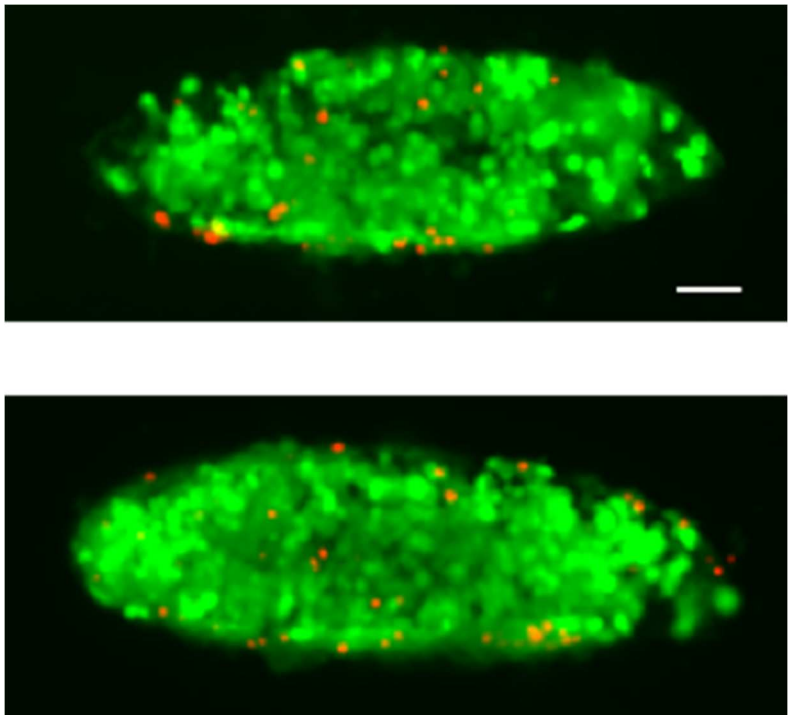

Figure 4.7: Fluorescent images depicting the viability of the liver constructs after 7 days in the integrated system.

Live cells are stained green, while dead cells are stained red. Huh7 cells were seen to be mostly viable in the GelMA construct after 7 days of integrated culture with the cardiac, muscle and cancer tissue. Scale bar denotes 100 μm.

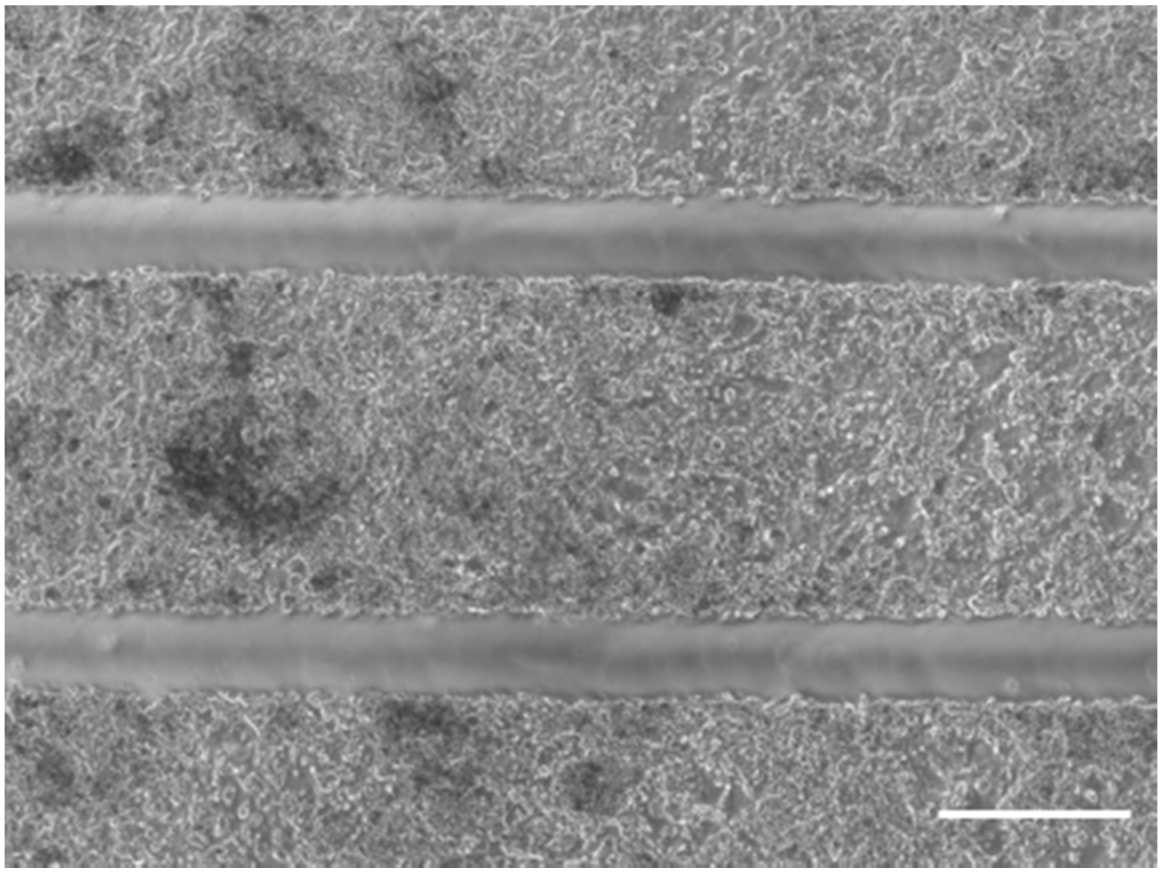

Figure 4.8: Brightfield image of the cardiac strips after 7 days of integrated culture with the other organ-on-a-chip platforms.

Brightfield image of the 2D cardiac strips in the organ-on-a-chip platform. There were no observable differences in the morphology of the strip throughout the 7 days of integrated culture. Scale bar depicts 200 μm

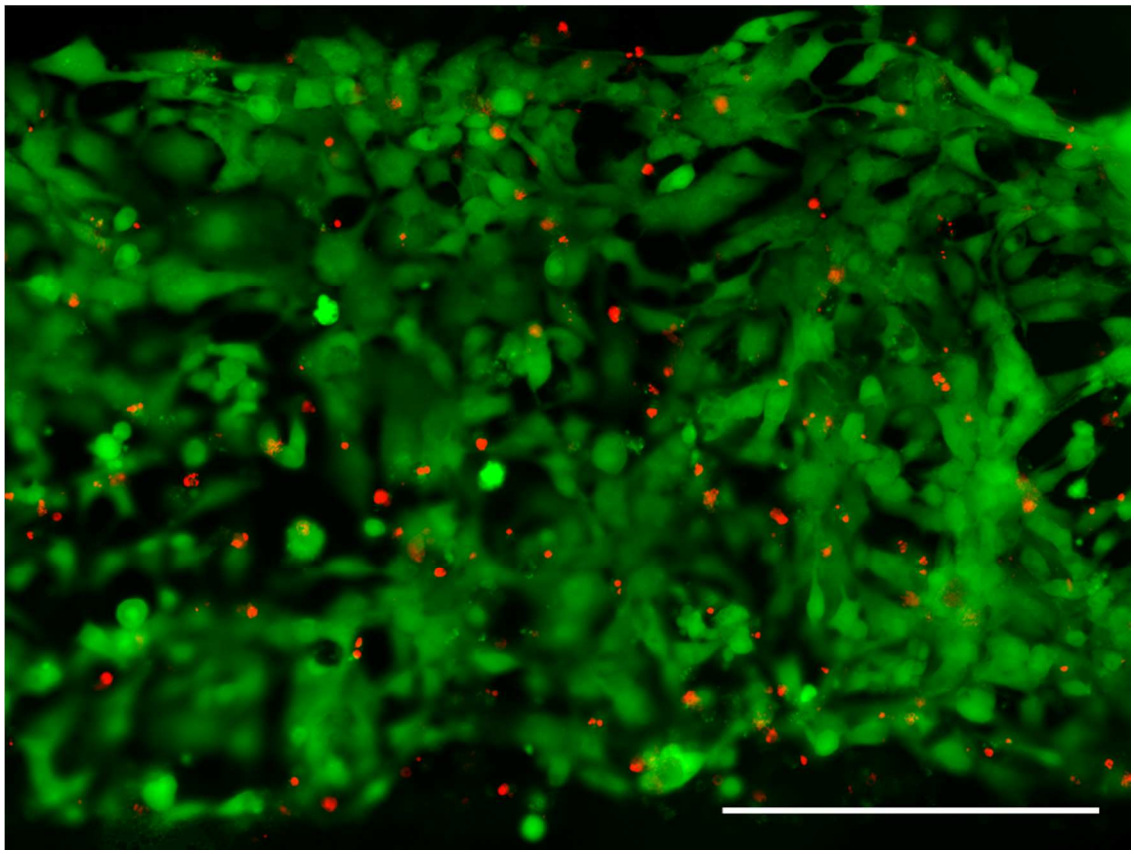

Figure 4.9: Fluorescent images depicting the viability of the iPSC derived cardiomyocyte strips after 7 days in the integrated system.

A live/dead assay was performed that stained live cells green and dead cells red. The iPSC derived cardiomyocytes were the least viable of the integrated devices, with a viability of approximately 85%-90% after 7 days of integrated culture with the liver-, muscle- and cancer-on-a-chip device. Scale bar denotes 100 μm.

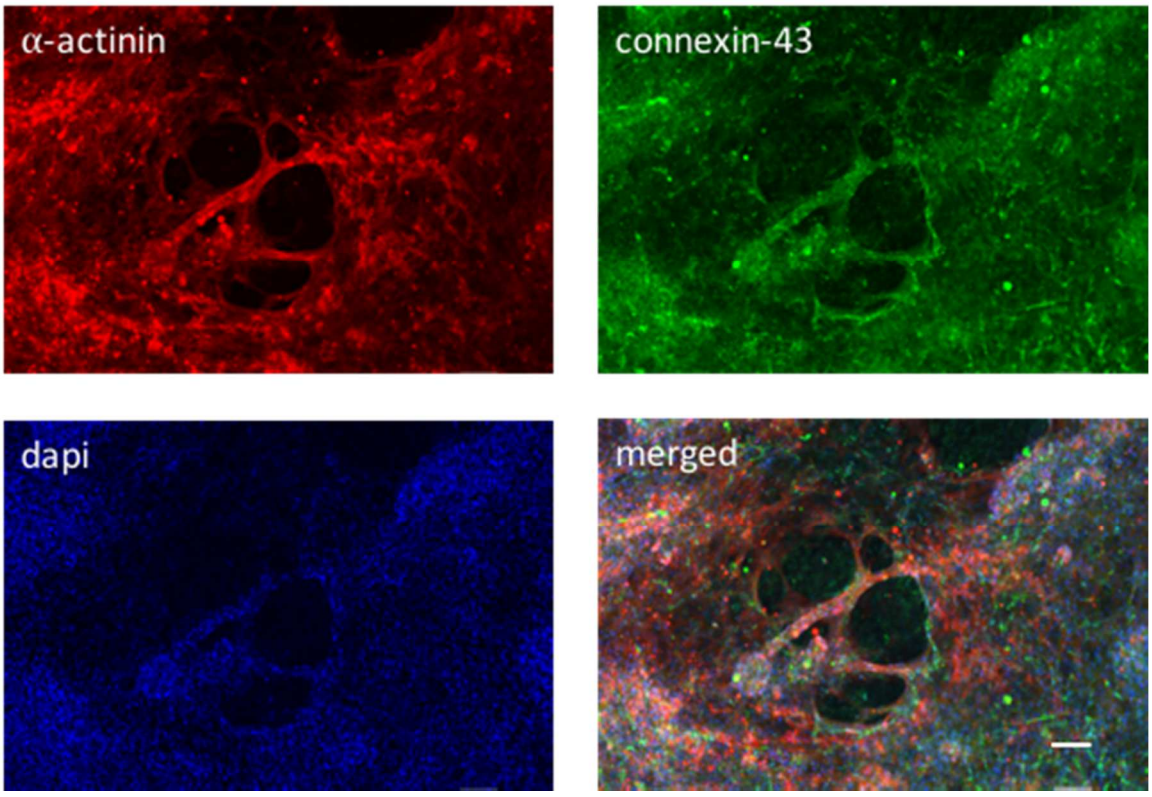

Figure 4.10: Immunofluorescent staining for cardiac markers in the heart-on-a-chip device after 7 days of integrated culture with the other organ-on-a-chip platforms.

The cardiac cell strips were fixed and stained with immunofluorescent antibodies to show positive staining for α-actinin, and connexin-43, markers for sarcomeric formation and gap function formation respectively. Scalebar denotes 100 μm.

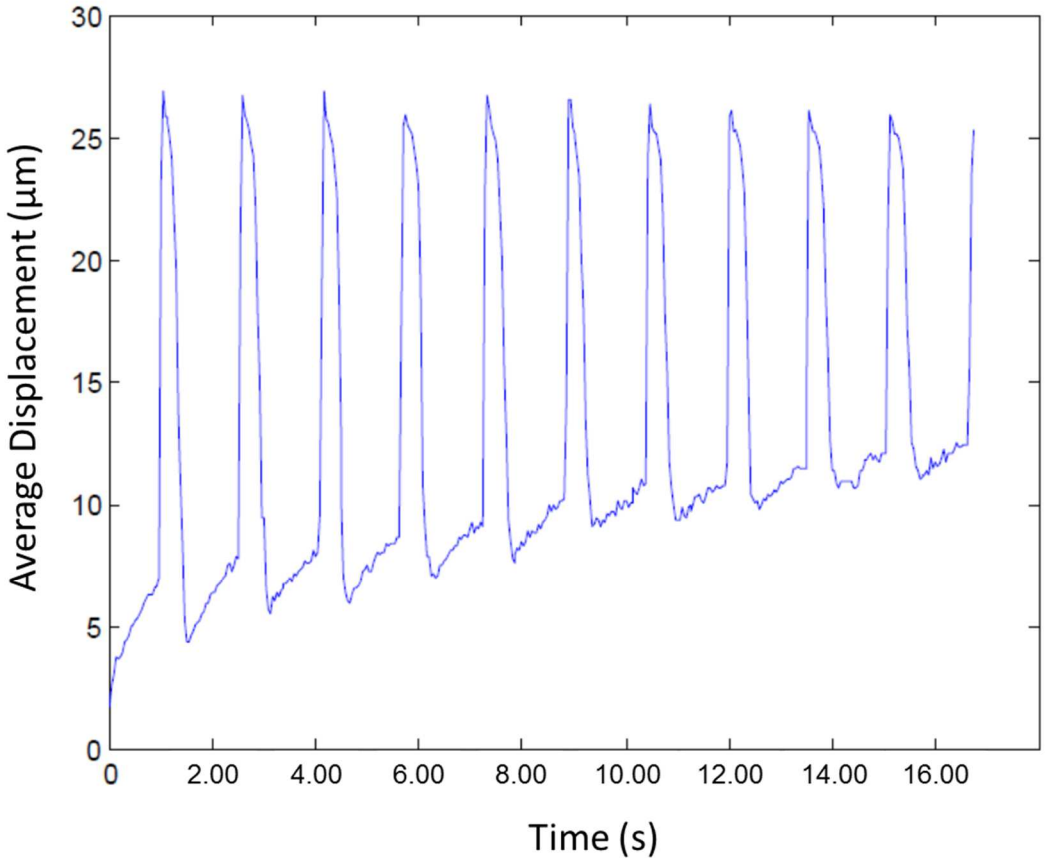

Figure 4.11: Beating frequency of the cardiac strips on the heart-on-a-chip platform

2D cardiac strips were observed to be beating (~0.5 Hz) in the culture.

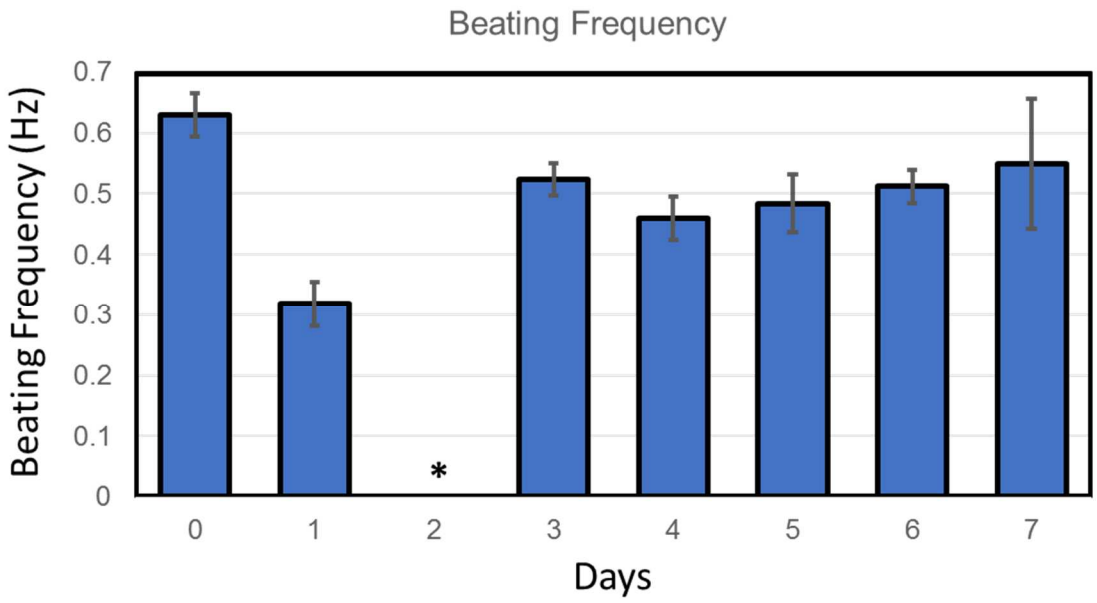

Figure 4.12: Beating frequency of the cardiac strips on the heart-on-a-chip platform

2D cardiac strips were observed to be beating at a frequency of ~0.6 Hz in the culture before integration. After integration, the frequency fell to ~0.3 at day 1 and was undetected at day 2. However, the cells started beating again from day 3 to day 7 at a constant frequency of ~0.5 Hz.

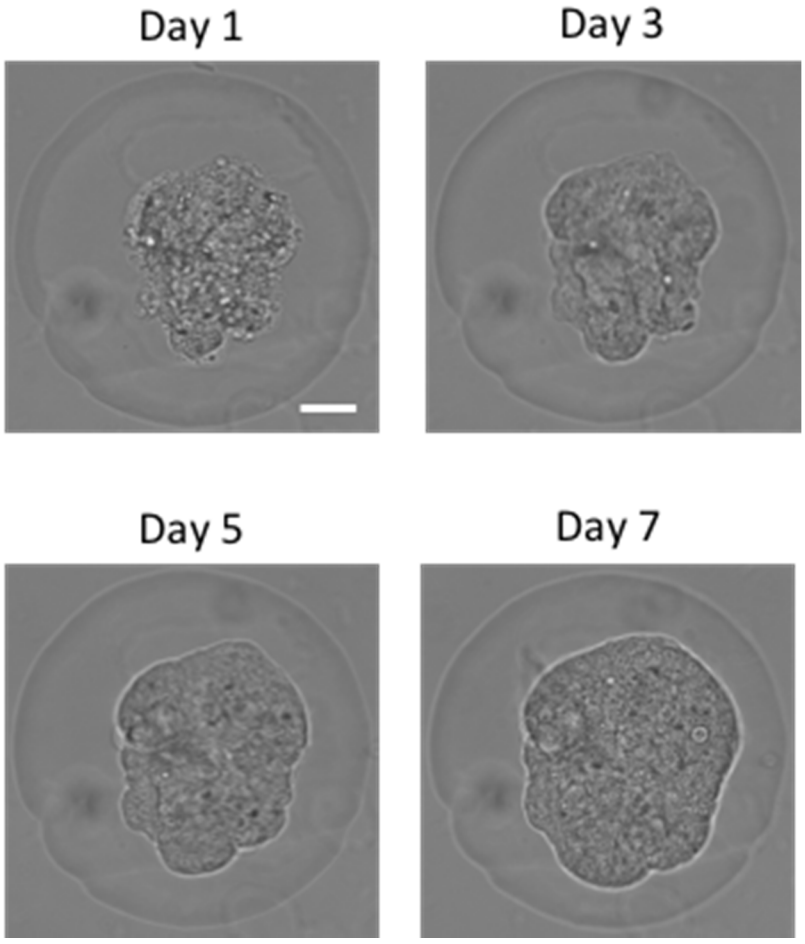

Figure 4.13: Brightfield images of MCF7 Spheroid growing for 7 days under the integrated culture with other organ-on-a-chip platforms.

Bright field images of the growing MCF7 Spheroids are presented at days 1, 3, 5 and 7 of the integrated culture with the other organ-on-a-chip platforms. Scale bar denotes 75 μm.

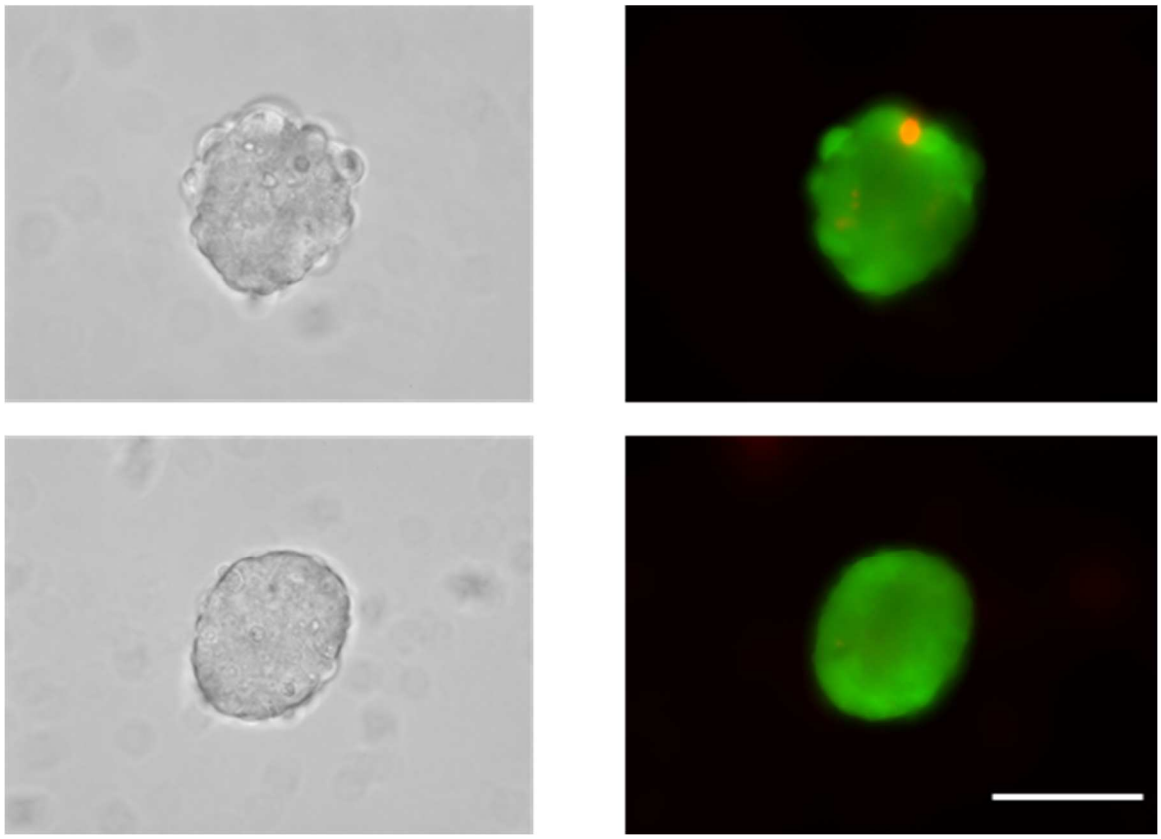

Figure 4.14: Brightfield and fluorescent images depicting the viability of the encapsulated cancer spheroid after 7 days under the integrated culture condition.

The MCF7 spheroid remained largely viable after 7 days in the integrated system. The brightfield images taken as a reference. Scale bar denotes 100 μm

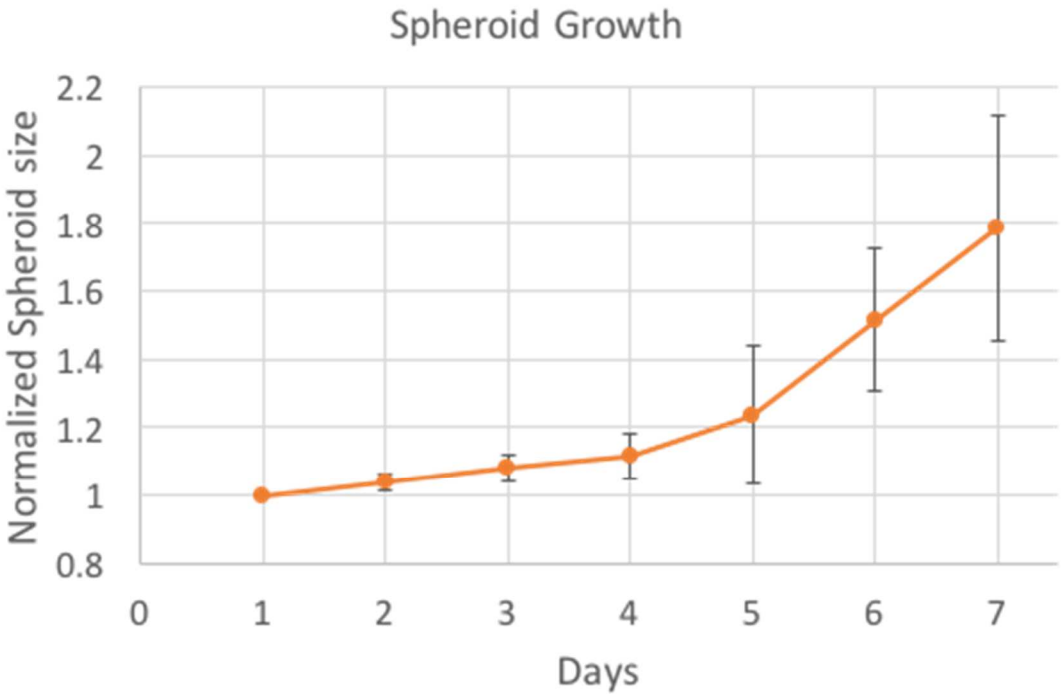

Figure 4.15: Plotting the growth of the MCF7 cancer spheroids during 7 days of culture under the integrated culture condition.

The MCF7 spheroids continued growing over the 7 days of integrated culture with the other organ-on-a-chip platforms.

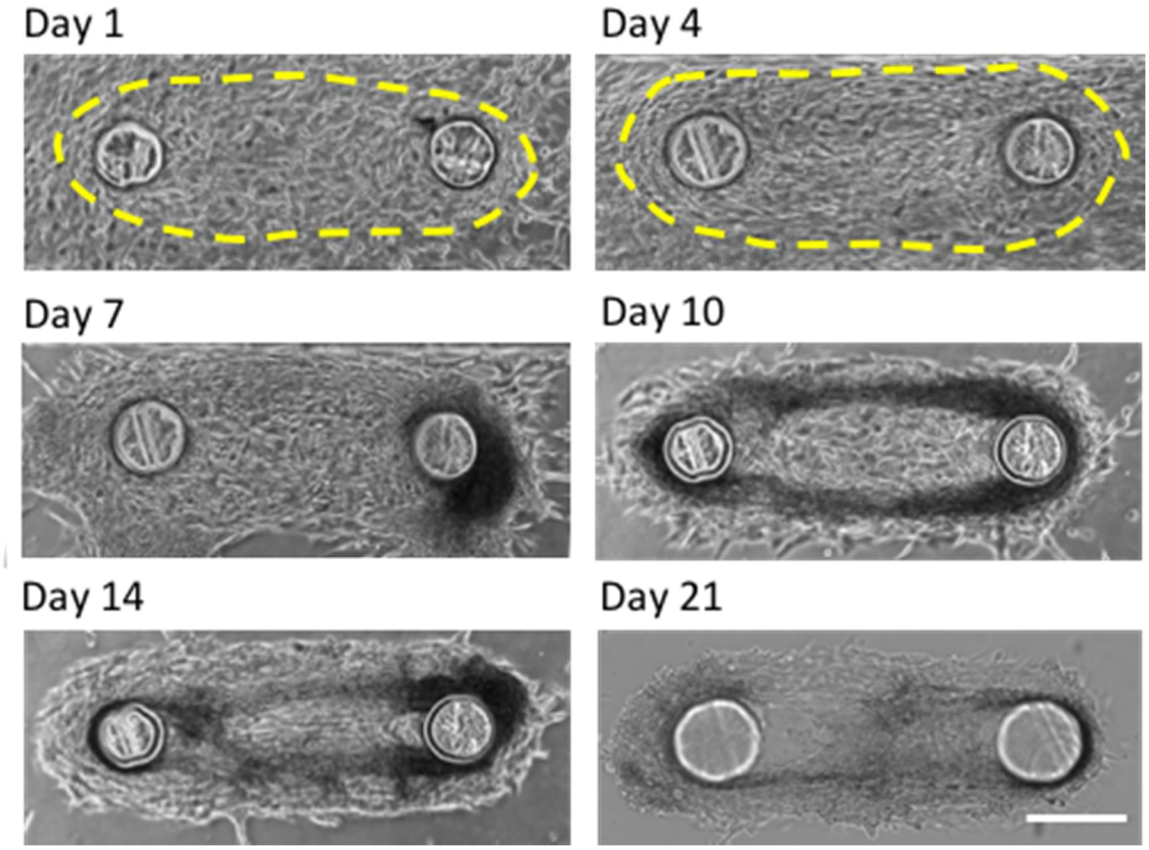

Figure 4.16: Bright field images of c2c12 cells growing and differentiating for the first 14 days as an independent muscle on chip platform, and the for 7 days in the integrated culture with other organ-on-a-chip platforms.

Bright field images of c2c12 cells growing, and then condensing into thick buncles as they start to differentiate and form myotubes (day 1-14). After 7 days in the integrated culture with organ-on-a-chip platforms, the thick bundles appear to have been reversed. Scale bar denotes 200 μm

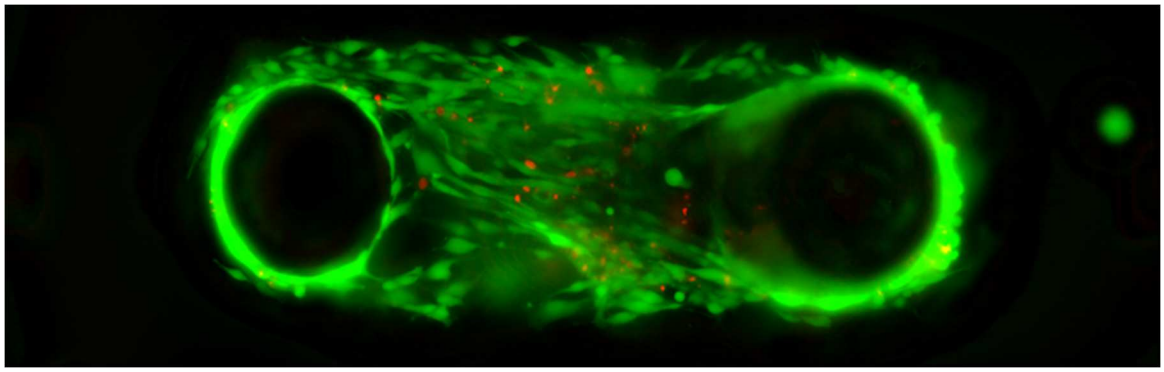

Figure 4.17: Fluorescent images depicting the viability of the muscle tissue after 7 days under the integrated culture condition.

The c2c12 muscle tissue remained largely viable after 7 days in the integrated system. Scale bar denotes 200 μm

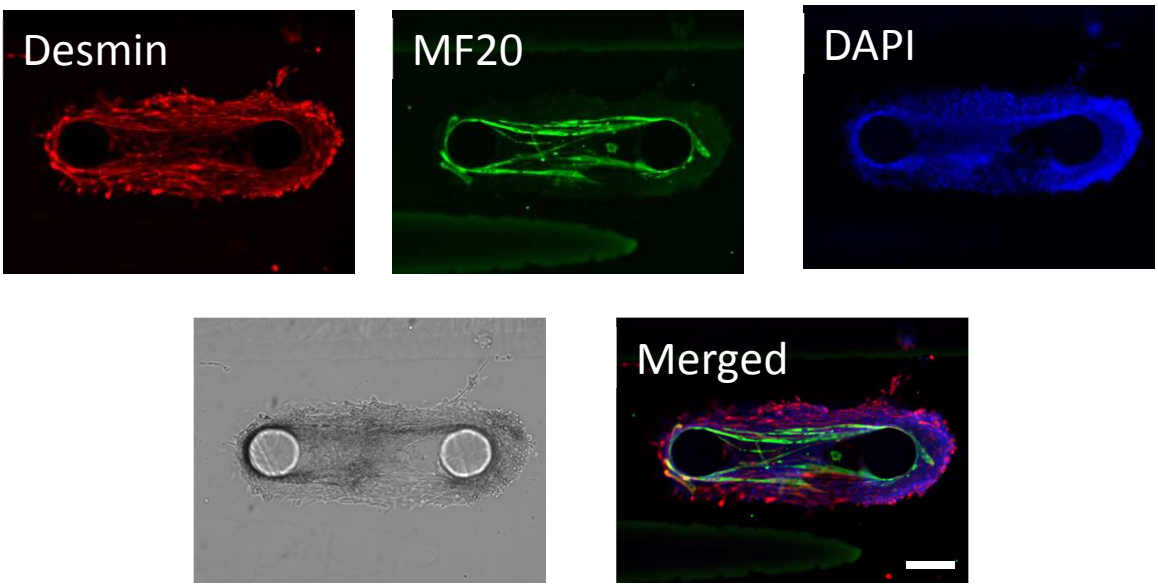

Figure 4.18: Immunofluorescent staining for myo- markers in the muscle-on-a-chip device after 7 days of integrated culture with the other organ-on-a-chip platforms.

The c2c12 cells wrapped around the pair of pillars was fixed and stained with immunofluorescent antibodies to show positive staining for desmin, and MF20, both markers for myogenic differentiation. Scale bar denotes 200 μm

Chapter 5: Future Directions

In the second chapter of this thesis, I have investigated the relationship between cellular stresses and the element of control amongst pairs of cells. The findings from this study indicate that there is a cooperativity between pairs of cells whereby the cell that is not in control undergoes mechanical softening to allow for the cell that is in control to drag it along. We have defined the lack of control as being "stagnant" and being allowed to be pulled along. Further studies should try to unravel the missing link between how being "stagnant" can lead to softening of the cell body. Related studies have suggested that physical or mechanical signaling between cells can induce cytoskeletal modelling, which would be a key modulator of the cells own mechanical property. As one of the most important regulators of cellular stress is activated rho, we could use molecules to inhibit its activation, or silence it from the gene, which will lead to lowered stresses in the cell sheet. However, we can still quantify cellular stresses in these systems, which will help us first determine if stress is indeed the key modulator amongst physical deformation or mechanical forces. Additional studies can also target an increase in the complexity of the system, such as increasing the number of cells that are in the system from a pair to three cells, or four cells, and see if the additional number of cells will affect each other in the same way as if there were only two cells. Such experiments will grant us more insight into the pairwise signaling in cellular collectives, even when multiple cells come together to form a collective.

In the third chapter of this thesis, we discovered a relationship between the rigidity of the encapsulating hydrogel material, and the diffusion of small molecules in the center-most core of the encapsulated spheroid. Specifically, it was observed that the less rigid the

hydrogel material, the higher the diffusivity in the center of the hydrogel. We hypothesize that materials with a higher rigidity would exert a greater amount of stress against the expansion of the cancer, which could lower the diffusivity in the center of the cancer mass. In future experiments, we could utilize computational or experimental techniques to measure the pressure within different regions of the spheroid, we can study the correlation of this pressure with changes in the diffusion coefficient in the spheroid. We can also use the microfluidic system to increase the pressure within the device, thereby artificially recapitulating an increase in the "interstitial fluid pressure". With this, we can determine if an increase in interstitial fluid pressure can also induce the same decrease in diffusivity as if the encapsulating substrate is of a higher rigidity. Depending on the outcome of this study, further experiments that probe the molecular implications of environmental mechanical stress can be conducted to determine how it affects diffusion on biological level.

In the last chapter of this thesis, we demonstrate a proof-of-concept integrated-multiple-organ-on-a-chip platform that maintains the viability and phenotypes of the cells used in each organ-on-a-chip. Additional studies that can be planned include the integration of more of different types of organ-on-a-chip platforms, which will include optimizing the media composition to keep the cells viable. Different types of drugs with known *in vivo* properties and toxicities can also be tested in the platform, to see how the platform fares at recapitulating *in vivo* observations. We can also study how good the system is at recreating *in vivo* diseases and disorders such as cystic fibrosis by obtaining and culturing primary cells from a cystic fibrosis patient. We can then use known drugs to attenuate these phenotypes, to demonstrate how it can be used as a platform to test novel drug candidates

as well. Finally, induced pluripotent stem cells can also be utilized as a cell source for all the different organs, to create a fully integrated device that is specific and personalized. Such platforms can be used as a personalized test bed for different drugs or even drug candidiates to evaluate their toxicity, and drug efficacy in the patient before administration.

References

1. N.I.H. 2017. A to Z list of cancer types.

2. A.S.C.O. 2017. Cancer Progress Timeline.

3. Begum, R., and S. A. Martin. 2016. Targeting Mismatch Repair defects: A novel strategy for personalized cancer treatment. DNA Repair 38:135-139.

4. Zhang, W., T. Duy Le, L. Liu, Z. H. Zhou, and J. Li. 2017. Mining heterogeneous causal effects for personalized cancer treatment. Bioinformatics.

5. Friedl, P., and D. Gilmour. 2009. Collective cell migration in morphogenesis, regeneration and cancer. Nat Rev Mol Cell Biol 10:445-457.

6. Scarpa, E., and R. Mayor. 2016. Collective cell migration in development. J Cell Biol 212:143-155.

7. Mayor, R., and S. Etienne-Manneville. 2016. The front and rear of collective cell migration. Nat Rev Mol Cell Biol 17:97-109.

8. Ridley, A. J., M. A. Schwartz, K. Burridge, R. A. Firtel, M. H. Ginsberg, G. Borisy, J. T. Parsons, and A. R. Horwitz. 2003. Cell migration: integrating signals from front to back. Science 302:1704-1709.

9. Ilina, O., and P. Friedl. 2009. Mechanisms of collective cell migration at a glance. J Cell Sci 122:3203-3208.

10. Haas, P., and D. Gilmour. 2006. Chemokine signaling mediates self-organizing tissue migration in the zebrafish lateral line. Dev Cell 10:673-680.

11. Venhuizen, J. H., and M. M. Zegers. 2017. Making Heads or Tails of It: Cell-Cell Adhesion in Cellular and Supracellular Polarity in Collective Migration. Cold Spring Harb Perspect Biol.

12. Barlan, K., M. Cetera, and S. Horne-Badovinac. 2017. Fat2 and Lar Define a Basally Localized Planar Signaling System Controlling Collective Cell Migration. Dev Cell 40:467-477 e465.

13. Serra-Picamal, X., V. Conte, R. Vincent, E. Anon, D. T. Tambe, E. Bazellieres, J. P. Butler, J. J. Fredberg, and X. Trepat. 2012. Mechanical waves during tissue expansion. Nat Phys 8:628-U666.

14. Reffay, M., M. C. Parrini, O. Cochet-Escartin, B. Ladoux, A. Buguin, S. Coscoy, F. Amblard, J. Camonis, and P. Silberzan. 2014. Interplay of RhoA and mechanical forces in collective cell migration driven by leader cells. Nat Cell Biol 16:217-223.

15. Brahimi-Horn, M. C., J. Chiche, and J. Pouyssegur. 2007. Hypoxia and cancer. J Mol Med (Berl) 85:1301-1307.

16. Kirkpatrick, J. P., D. M. Brizel, and M. W. Dewhirst. 2003. A mathematical model of tumor oxygen and glucose mass transport and metabolism with complex reaction kinetics. Radiat Res 159:336-344.

17. Pruijn, F. B., K. Patel, M. P. Hay, W. R. Wilson, and K. O. Hicks. 2008. Prediction of tumour tissue diffusion coefficients of hypoxia-activated prodrugs from physicochemical parameters. Aust J Chem 61:687-693.

18. Semenza, G. L. 2016. The hypoxic tumor microenvironment: A driving force for breast cancer progression. Bba-Mol Cell Res 1863:382-391.

19. Fu, F., M. A. Nowak, and S. Bonhoeffer. 2015. Spatial heterogeneity in drug concentrations can facilitate the emergence of resistance to cancer therapy. PLoS Comput Biol 11:e1004142.

20. Moreno-Gamez, S., A. L. Hill, D. I. Rosenbloom, D. A. Petrov, M. A. Nowak, and P. S. Pennings. 2015. Imperfect drug penetration leads to spatial monotherapy and rapid evolution of multidrug resistance. Proc Natl Acad Sci U S A 112:E2874-2883.

21. Tannock, I. F., C. M. Lee, J. K. Tunggal, D. S. M. Cowan, and M. J. Egorin. 2002. Limited penetration of anticancer drugs through tumor tissue: A potential cause of resistance of solid tumors to chemotherapy. Clin Cancer Res 8:878-884.

22. Huh, D., B. D. Matthews, A. Mammoto, M. Montoya-Zavala, H. Y. Hsin, and D. E. Ingber. 2010. Reconstituting organ-level lung functions on a chip. Science 328:1662-1668.

23. Jang, K. J., A. P. Mehr, G. A. Hamilton, L. A. McPartlin, S. Chung, K. Y. Suh, and D. E. Ingber. 2013. Human kidney proximal tubule-on-a-chip for drug transport and nephrotoxicity assessment. Integr Biol (Camb) 5:1119-1129.

24. Lee, J. S., R. Romero, Y. M. Han, H. C. Kim, C. J. Kim, J. S. Hong, and D. Huh. 2016. Placenta-on-a-chip: a novel platform to study the biology of the human placenta. J Matern Fetal Neonatal Med 29:1046-1054.

25. Lee, J. B., and J. H. Sung. 2013. Organ-on-a-chip technology and microfluidic whole-body models for pharmacokinetic drug toxicity screening. Biotechnol J 8:1258-1266.

26. Li, X. J., A. V. Valadez, P. Zuo, and Z. H. Nie. 2012. Microfluidic 3D cell culture: potential application for tissue-based bioassays. Bioanalysis 4:1509-1525.

27. Loskill, P., S. G. Marcus, A. Mathur, W. M. Reese, and K. E. Healy. 2015. muOrgano: A Lego(R)-Like Plug & Play System for Modular Multi-Organ-Chips. Plos One 10:e0139587.

28. Williamson, A., S. Singh, U. Fernekorn, and A. Schober. 2013. The future of the patient-specific Body-on-a-chip. Lab Chip 13:3471-3480.

29. Somlyo, A. V., D. Bradshaw, S. Ramos, C. Murphy, C. E. Myers, and A. P. Somlyo. 2000. Rho-kinase inhibitor retards migration and in vivo dissemination of human prostate cancer cells. Biochem Biophys Res Commun 269:652-659.

30. Friedl, P., and K. Wolf. 2003. Tumour-cell invasion and migration: diversity and escape mechanisms. Nat Rev Cancer 3:362-374.

31. Nakajima, M., K. Hayashi, K. Katayama, Y. Amano, Y. Egi, M. Uehata, N. Goto, and T. Kondo. 2003. Wf-536 prevents tumor metastasis by inhibiting both tumor motility and angiogenic actions. Eur J Pharmacol 459:113-120.

32. Malliri, A., S. van Es, S. Huveneers, and J. G. Collard. 2004. The Rac exchange factor Tiam1 is required for the establishment and maintenance of cadherin-based adhesions. J Biol Chem 279:30092-30098.

33. Fukuyama, T., H. Ogita, T. Kawakatsu, M. Inagaki, and Y. Takai. 2006. Activation of Rac by cadherin through the c-Src-Rap1-phosphatidylinositol 3-kinase-Vav2 pathway. Oncogene 25:8-19.

34. Friedl, P., Y. Hegerfeldt, and M. Tusch. 2004. Collective cell migration in morphogenesis and cancer. Int J Dev Biol 48:441-449.

35. Borghi, N., M. Lowndes, V. Maruthamuthu, M. L. Gardel, and W. J. Nelson. 2010. Regulation of cell motile behavior by crosstalk between cadherin- and integrin-mediated adhesions. Proc Natl Acad Sci U S A 107:13324-13329.

36. Humphrey, J. D., E. R. Dufresne, and M. A. Schwartz. 2014. Mechanotransduction and extracellular matrix homeostasis. Nat Rev Mol Cell Biol 15:802-812.

37. Lo, C. M., H. B. Wang, M. Dembo, and Y. L. Wang. 2000. Cell movement is guided by the rigidity of the substrate. Biophys J 79:144-152.

38. Wen, J. H., L. G. Vincent, A. Fuhrmann, Y. S. Choi, K. C. Hribar, H. Taylor-Weiner, S. Chen, and A. J. Engler. 2014. Interplay of matrix stiffness and protein tethering in stem cell differentiation. Nat Mater 13:979-987.

39. Rape, A. D., W. H. Guo, and Y. L. Wang. 2011. The regulation of traction force in relation to cell shape and focal adhesions. Biomaterials 32:2043-2051.

40. Ingber, D. E. 2005. Mechanical control of tissue growth: function follows form. Proc Natl Acad Sci U S A 102:11571-11572.

41. Szabo, A., and R. Mayor. 2015. Cell traction in collective cell migration and morphogenesis: the chase and run mechanism. Cell Adh Migr 9:380-383.

42. Dupin, I., E. Camand, and S. Etienne-Manneville. 2009. Classical cadherins control nucleus and centrosome position and cell polarity. J Cell Biol 185:779-786.

43. Omelchenko, T., J. M. Vasiliev, I. M. Gelfand, H. H. Feder, and E. M. Bonder. 2003. Rho-dependent formation of epithelial "leader" cells during wound healing. Proc Natl Acad Sci U S A 100:10788-10793.

44. Abraham, S., M. Yeo, M. Montero-Balaguer, H. Paterson, E. Dejana, C. J. Marshall, and G. Mavria. 2009. VE-Cadherin-mediated cell-cell interaction suppresses sprouting via signaling to MLC2 phosphorylation. Curr Biol 19:668-674.

45. Carmona-Fontaine, C., H. K. Matthews, S. Kuriyama, M. Moreno, G. A. Dunn, M. Parsons, C. D. Stern, and R. Mayor. 2008. Contact inhibition of locomotion in vivo controls neural crest directional migration. Nature 456:957-961.

46. Nelson, C. M., H. Wibisono, H. Purwanto, I. Mansyur, V. Moniaga, and A. Widjaya. 2004. Hepatitis B vaccine freezing in the Indonesian cold chain: evidence and solutions. Bull World Health Organ 82:99-105.

47. Nakagawa, M., M. Fukata, M. Yamaga, N. Itoh, and K. Kaibuchi. 2001. Recruitment and activation of Rac1 by the formation of E-cadherin-mediated cell-cell adhesion sites. J Cell Sci 114:1829-1838.

48. Kim, S. H., Z. Li, and D. B. Sacks. 2000. E-cadherin-mediated cell-cell attachment activates Cdc42. J Biol Chem 275:36999-37005.

49. Hartsock, A., and W. J. Nelson. 2008. Adherens and tight junctions: structure, function and connections to the actin cytoskeleton. Biochim Biophys Acta 1778:660-669.

50. Halbleib, J. M., and W. J. Nelson. 2006. Cadherins in development: cell adhesion, sorting, and tissue morphogenesis. Genes Dev 20:3199-3214.

51. Butler, J. P., I. M. Tolic-Norrelykke, B. Fabry, and J. J. Fredberg. 2002. Traction fields, moments, and strain energy that cells exert on their surroundings. Am J Physiol Cell Physiol 282:C595-605.

52. Trepat, X., M. R. Wasserman, T. E. Angelini, E. Millet, D. A. Weitz, J. P. Butler, and J. J. Fredberg. 2009. Physical forces during collective cell migration. Nat Phys 5:426-430.

53. Tambe, D. T., C. C. Hardin, T. E. Angelini, K. Rajendran, C. Y. Park, X. Serra-Picamal, E. H. Zhou, M. H. Zaman, J. P. Butler, D. A. Weitz, J. J. Fredberg, and X. Trepat. 2011. Collective cell guidance by cooperative intercellular forces. Nat Mater 10:469-475.

54. Hur, S. S., J. C. del Alamo, J. S. Park, Y. S. Li, H. A. Nguyen, D. Y. Teng, K. C. Wang, L. Flores, B. Alonso-Latorre, J. C. Lasheras, and S. Chien. 2012. Roles of cell confluency and fluid shear in 3-dimensional intracellular forces in endothelial cells. P Natl Acad Sci USA 109:11110-11115.

55. Kim, J. H., X. Serra-Picamal, D. T. Tambe, E. H. Zhou, C. Y. Park, M. Sadati, J. A. Park, R. Krishnan, B. Gweon, E. Millet, J. P. Butler, X. Trepat, and J. J. Fredberg. 2013. Propulsion and navigation within the advancing monolayer sheet. Nat Mater 12:856-863.

56. Vedula, S. R., H. Hirata, M. H. Nai, A. Brugues, Y. Toyama, X. Trepat, C. T. Lim, and B. Ladoux. 2014. Epithelial bridges maintain tissue integrity during collective cell migration. Nat Mater 13:87-96.

57. Grashoff, C., B. D. Hoffman, M. D. Brenner, R. Zhou, M. Parsons, M. T. Yang, M. A. McLean, S. G. Sligar, C. S. Chen, T. Ha, and M. A. Schwartz. 2010. Measuring mechanical tension across vinculin reveals regulation of focal adhesion dynamics. Nature 466:263-266.

58. Vedula, S. R. K., A. Ravasio, C. T. Lim, and B. Ladoux. 2013. Collective Cell Migration: A Mechanistic Perspective. Physiology 28:370-379.

59. Doxzen, K., S. R. Vedula, M. C. Leong, H. Hirata, N. S. Gov, A. J. Kabla, B. Ladoux, and C. T. Lim. 2013. Guidance of collective cell migration by substrate geometry. Integr Biol (Camb) 5:1026-1035.

60. Mayor, R., and C. Carmona-Fontaine. 2010. Keeping in touch with contact inhibition of locomotion. Trends Cell Biol 20:319-328.

61. Grantab, R., S. Sivananthan, and I. F. Tannock. 2006. The penetration of anticancer drugs through tumor tissue as a function of cellular adhesion and packing density of tumor cells. Cancer Research 66:1033-1039.

62. Grantab, R. H., and I. F. Tannock. 2012. Penetration of anticancer drugs through tumour tissue as a function of cellular packing density and interstitial fluid pressure and its modification by bortezomib. Bmc Cancer 12.

63. Baxter, L. T., and R. K. Jain. 1989. Transport of fluid and macromolecules in tumors. I. Role of interstitial pressure and convection. Microvasc Res 37:77-104.

64. Jain, R. K., J. M. Weissbrod, and J. Wei. 1980. Mass transport in tumors: characterization and applications to chemotherapy. Adv Cancer Res 33:251-310.

65. Thoma, C. R., M. Zimmermann, I. Agarkova, J. M. Kelm, and W. Krek. 2014. 3D cell culture systems modeling tumor growth determinants in cancer target discovery. Adv Drug Deliv Rev 69-70:29-41.

66. Tunggal, J. K., D. S. M. Cowan, H. Shaikh, and I. F. Tannock. 1999. Penetration of anticancer drugs through solid tissue: A factor that limits the effectiveness of chemotherapy for solid tumors. Clin Cancer Res 5:1583-1586.

67. Fletcher, J. I., M. Haber, M. J. Henderson, and M. D. Norris. 2010. ABC transporters in cancer: more than just drug efflux pumps. Nat Rev Cancer 10:147-156.

68. Fletcher, J. I., R. T. Williams, M. J. Henderson, M. D. Norris, and M. Haber. 2016. ABC transporters as mediators of drug resistance and contributors to cancer cell biology. Drug Resist Updat 26:1-9.

69. Modok, S., H. R. Mellor, and R. Callaghan. 2006. Modulation of multidrug resistance efflux pump activity to overcome chemoresistance in cancer. Curr Opin Pharmacol 6:350-354.

70. Martinez-Lacaci, I., P. Garcia Morales, J. L. Soto, and M. Saceda. 2007. Tumour cells resistance in cancer therapy. Clin Transl Oncol 9:13-20.

71. Lovitt, C. J., T. B. Shelper, and V. M. Avery. 2014. Advanced cell culture techniques for cancer drug discovery. Biology (Basel) 3:345-367.

72. Xu, X., M. C. Farach-Carson, and X. Jia. 2014. Three-dimensional in vitro tumor models for cancer research and drug evaluation. Biotechnol Adv 32:1256-1268.

73. Lu, Y. C., W. Song, D. An, B. J. Kim, R. Schwartz, M. M. Wu, and M. L. Ma. 2015. Designing compartmentalized hydrogel microparticles for cell encapsulation and scalable 3D cell culture. J Mater Chem B 3:353-360.

74. Gong, X., C. Lin, J. Cheng, J. S. Su, H. Zhao, T. L. Liu, X. J. Wen, and P. Zhao. 2015. Generation of Multicellular Tumor Spheroids with Microwell-Based Agarose Scaffolds for Drug Testing. Plos One 10.

75. Graff, C. P., and K. D. Wittrup. 2003. Theoretical analysis of antibody targeting of tumor spheroids: Importance of dosage for penetration, and affinity for retention. Cancer Research 63:1288-1296.

76. Thurber, G. M., M. M. Schmidt, and K. D. Wittrup. 2008. Antibody tumor penetration: Transport opposed by systemic and antigen-mediated clearance. Adv Drug Deliver Rev 60:1421-1434.

77. Wong, H. L., Z. C. Shen, Z. Lu, M. G. Wientjes, and J. L. S. Au. 2011. Paclitaxel Tumor-Priming Enhances siRNA Delivery and Transfection in 3-Dimensional Tumor Cultures. Mol Pharmaceut 8:833-840.

78. Sharkey, R. M., and D. M. Goldenberg. 2008. Use of antibodies and immunoconjugates for the therapy of more accessible cancers. Adv Drug Deliver Rev 60:1407-1420.

79. Carver, K., X. Ming, and R. L. Juliano. 2014. Multicellular Tumor Spheroids as a Model for Assessing Delivery of Oligonucleotides in Three Dimensions. Mol Ther-Nucl Acids 3.

80. Chitcholtan, K., P. H. Sykes, and J. J. Evans. 2012. The resistance of intracellular mediators to doxorubicin and cisplatin are distinct in 3D and 2D endometrial cancer. J Transl Med 10.

81. Ong, S. M., Z. Zhao, T. Arooz, D. Zhao, S. Zhang, T. Du, M. Wasser, D. van Noort, and H. Yu. 2010. Engineering a scaffold-free 3D tumor model for in vitro drug penetration studies. Biomaterials 31:1180-1190.

82. Walsh, C. L., B. M. Babin, R. W. Kasinskas, J. A. Foster, M. J. McGarry, and N. S. Forbes. 2009. A multipurpose microfluidic device designed to mimic microenvironment gradients and develop targeted cancer therapeutics. Lab Chip 9:545-554.

83. Hakanson, M., E. Cukierman, and M. Charnley. 2014. Miniaturized pre-clinical cancer models as research and diagnostic tools. Adv Drug Deliver Rev 69:52-66.

84. Ellenbroek, S. I., and J. van Rheenen. 2014. Imaging hallmarks of cancer in living mice. Nat Rev Cancer 14:406-418.

85. Saggar, J. K., A. S. Fung, K. J. Patel, and I. F. Tannock. 2013. Use of molecular biomarkers to quantify the spatial distribution of effects of anticancer drugs in solid tumors. Mol Cancer Ther 12:542-552.

86. Nugent, L. J., and R. K. Jain. 1984. Extravascular Diffusion in Normal and Neoplastic Tissues. Cancer Research 44:238-244.

87. Brown, C. M., D. R. Rivera, I. Pavlova, D. G. Ouzounov, W. O. Williams, S. Mohanan, W. W. Webb, and C. Xu. 2012. In vivo imaging of unstained tissues using a compact and flexible multiphoton microendoscope. J Biomed Opt 17:040505.

88. Zipfel, W. R., R. M. Williams, and W. W. Webb. 2003. Nonlinear magic: multiphoton microscopy in the biosciences. Nat Biotechnol 21:1369-1377.

89. Huh, D., G. A. Hamilton, and D. E. Ingber. 2011. From 3D cell culture to organs-on-chips. Trends Cell Biol 21:745-754.

90. Esch, M. B., T. L. King, and M. L. Shuler. 2011. The role of body-on-a-chip devices in drug and toxicity studies. Annu Rev Biomed Eng 13:55-72.

91. Wikswo, J. P., E. L. Curtis, Z. E. Eagleton, B. C. Evans, A. Kole, L. H. Hofmeister, and W. J. Matloff. 2013. Scaling and systems biology for integrating multiple organs-on-a-chip. Lab Chip 13:3496-3511.

92. Schepers, A., C. Li, A. Chhabra, B. T. Seney, and S. Bhatia. 2016. Engineering a perfusable 3D human liver platform from iPS cells. Lab Chip 16:2644-2653.

93. Wang, G., M. L. McCain, L. Yang, A. He, F. S. Pasqualini, A. Agarwal, H. Yuan, D. Jiang, D. Zhang, L. Zangi, J. Geva, A. E. Roberts, Q. Ma, J. Ding, J. Chen, D. Z. Wang, K. Li, J. Wang, R. J. Wanders, W. Kulik, F. M. Vaz, M. A. Laflamme, C. E. Murry, K. R. Chien, R. I. Kelley, G. M. Church, K. K. Parker, and W. T. Pu. 2014. Modeling the mitochondrial cardiomyopathy of Barth syndrome with induced pluripotent stem cell and heart-on-chip technologies. Nat Med 20:616-623.

94. Huh, D., D. C. Leslie, B. D. Matthews, J. P. Fraser, S. Jurek, G. A. Hamilton, K. S. Thorneloe, M. A. McAlexander, and D. E. Ingber. 2012. A human disease model of drug toxicity-induced pulmonary edema in a lung-on-a-chip microdevice. Sci Transl Med 4:159ra147.

95. Stucki, A. O., J. D. Stucki, S. R. Hall, M. Felder, Y. Mermoud, R. A. Schmid, T. Geiser, and O. T. Guenat. 2015. A lung-on-a-chip array with an integrated bio-inspired respiration mechanism. Lab Chip 15:1302-1310.

96. Punde, T. H., W. H. Wu, P. C. Lien, Y. L. Chang, P. H. Kuo, M. D. Chang, K. Y. Lee, C. D. Huang, H. P. Kuo, Y. F. Chan, P. C. Shih, and C. H. Liu. 2015. A biologically inspired lung-on-a-chip device for the study of protein-induced lung inflammation. Integr Biol (Camb) 7:162-169.

97. Grosberg, A., P. W. Alford, M. L. McCain, and K. K. Parker. 2011. Ensembles of engineered cardiac tissues for physiological and pharmacological study: heart on a chip. Lab Chip 11:4165-4173.

98. Agarwal, A., J. A. Goss, A. Cho, M. L. McCain, and K. K. Parker. 2013. Microfluidic heart on a chip for higher throughput pharmacological studies. Lab Chip 13:3599-3608.

99. Mathur, A., P. Loskill, K. Shao, N. Huebsch, S. Hong, S. G. Marcus, N. Marks, M. Mandegar, B. R. Conklin, L. P. Lee, and K. E. Healy. 2015. Human iPSC-based cardiac microphysiological system for drug screening applications. Sci Rep 5:8883.

100. Aung, A., I. S. Bhullar, J. Theprungsirikul, S. K. Davey, H. L. Lim, Y. J. Chiu, X. Y. Ma, S. Dewan, Y. H. Lo, A. McCulloch, and S. Varghese. 2016. 3D cardiac mu tissues within a microfluidic device with real-time contractile stress readout. Lab Chip 16:153-162.

101. Bissell, D. M., G. J. Gores, D. L. Laskin, and J. H. Hoofnagle. 2001. Drug-induced liver injury: mechanisms and test systems. Hepatology 33:1009-1013.

102. Soldatow, V. Y., E. L. Lecluyse, L. G. Griffith, and I. Rusyn. 2013. In vitro models for liver toxicity testing. Toxicol Res (Camb) 2:23-39.

103. Dambach, D. M., B. A. Andrews, and F. Moulin. 2005. New technologies and screening strategies for hepatotoxicity: use of in vitro models. Toxicol Pathol 33:17-26.

104. Bhise, N. S., V. Manoharan, S. Massa, A. Tamayol, M. Ghaderi, M. Miscuglio, Q. Lang, Y. Shrike Zhang, S. R. Shin, G. Calzone, N. Annabi, T. D. Shupe, C. E. Bishop, A. Atala, M. R. Dokmeci, and A. Khademhosseini. 2016. A liver-on-a-chip platform with bioprinted hepatic spheroids. Biofabrication 8:014101.

105. Lee, J., S. H. Kim, Y. C. Kim, I. Choi, and J. H. Sung. 2013. Fabrication and characterization of microfluidic liver-on-a-chip using microsomal enzymes. Enzyme Microb Technol 53:159-164.

106. Wagner, I., E. M. Materne, S. Brincker, U. Sussbier, C. Fradrich, M. Busek, F. Sonntag, D. A. Sakharov, E. V. Trushkin, A. G. Tonevitsky, R. Lauster, and U. Marx. 2013. A dynamic multi-organ-chip for long-term cultivation and substance testing proven by 3D human liver and skin tissue co-culture. Lab Chip 13:3538-3547.

107. Maschmeyer, I., A. K. Lorenz, K. Schimek, T. Hasenberg, A. P. Ramme, J. Hubner, M. Lindner, C. Drewell, S. Bauer, A. Thomas, N. S. Sambo, F. Sonntag, R. Lauster, and U. Marx. 2015. A four-organ-chip for interconnected long-term co-culture of human intestine, liver, skin and kidney equivalents. Lab Chip 15:2688-2699.

108. Dash, A., M. B. Simmers, T. G. Deering, D. J. Berry, R. E. Feaver, N. E. Hastings, T. L. Pruett, E. L. LeCluyse, B. R. Blackman, and B. R. Wamhoff. 2013. Hemodynamic flow improves rat hepatocyte morphology, function, and metabolic activity in vitro. Am J Physiol Cell Physiol 304:C1053-1063.

109. Lee, P. J., P. J. Hung, and L. P. Lee. 2007. An artificial liver sinusoid with a microfluidic endothelial-like barrier for primary hepatocyte culture. Biotechnol Bioeng 97:1340-1346.

110. Kim, H. J., D. Huh, G. Hamilton, and D. E. Ingber. 2012. Human gut-on-a-chip inhabited by microbial flora that experiences intestinal peristalsis-like motions and flow. Lab Chip 12:2165-2174.

111. Esch, M. B., J. H. Sung, J. Yang, C. H. Yu, J. J. Yu, J. C. March, and M. L. Shuler. 2012. On chip porous polymer membranes for integration of gastrointestinal tract epithelium with microfluidic 'body-on-a-chip' devices. Biomed Microdevices 14:895-906.

112. Huh, D., Y. S. Torisawa, G. A. Hamilton, H. J. Kim, and D. E. Ingber. 2012. Microengineered physiological biomimicry: organs-on-chips. Lab Chip 12:2156-2164.

113. Wilmer, M. J., C. P. Ng, H. L. Lanz, P. Vulto, L. Suter-Dick, and R. Masereeuw. 2016. Kidney-on-a-Chip Technology for Drug-Induced Nephrotoxicity Screening. Trends Biotechnol 34:156-170.

114. Mu, X., W. Zheng, L. Xiao, W. Zhang, and X. Jiang. 2013. Engineering a 3D vascular network in hydrogel for mimicking a nephron. Lab Chip 13:1612-1618.

115. Sung, J. H., and M. L. Shuler. 2009. A micro cell culture analog (microCCA) with 3-D hydrogel culture of multiple cell lines to assess metabolism-dependent cytotoxicity of anti-cancer drugs. Lab Chip 9:1385-1394.

116. Zhang, C., Z. Zhao, N. A. Abdul Rahim, D. van Noort, and H. Yu. 2009. Towards a human-on-chip: culturing multiple cell types on a chip with compartmentalized microenvironments. Lab Chip 9:3185-3192.

117. Maruthamuthu, V., B. Sabass, U. S. Schwarz, and M. L. Gardel. 2011. Cell-ECM traction force modulates endogenous tension at cell-cell contacts. Proc Natl Acad Sci U S A 108:4708-4713.

118. Beningo, K. A., M. Dembo, I. Kaverina, J. V. Small, and Y. L. Wang. 2001. Nascent focal adhesions are responsible for the generation of strong propulsive forces in migrating fibroblasts. Journal of Cell Biology 153:881-887.

119. Liu, Z. J., J. L. Tan, D. M. Cohen, M. T. Yang, N. J. Sniadecki, S. A. Ruiz, C. M. Nelson, and C. S. Chen. 2010. Mechanical tugging force regulates the size of cell-cell junctions. P Natl Acad Sci USA 107:9944-9949.

120. Das, T., K. Safferling, S. Rausch, N. Grabe, H. Boehm, and J. P. Spatz. 2015. A molecular mechanotransduction pathway regulates collective migration of epithelial cells. Nat Cell Biol 17:276-287.

121. Weber, G. F., M. A. Bjerke, and D. W. DeSimone. 2012. A mechanoresponsive cadherin-keratin complex directs polarized protrusive behavior and collective cell migration. Dev Cell 22:104-115.

122. Chen, C. S., J. Tan, and J. Tien. 2004. Mechanotransduction at cell-matrix and cell-cell contacts. Annual Review of Biomedical Engineering 6:275-302.

123. Wozniak, M. A., and C. S. Chen. 2009. Mechanotransduction in development: a growing role for contractility. Nat Rev Mol Cell Bio 10:34-43.

124. Murrell, M., R. Kamm, and P. Matsudaira. 2011. Tension, free space, and cell damage in a microfluidic wound healing assay. Plos One 6:e24283.

125. Bindschadler, M., and J. L. McGrath. 2007. Sheet migration by wounded monolayers as an emergent property of single-cell dynamics. Journal of Cell Science 120:876-884.

126. Raghavan, S., C. M. Nelson, J. D. Baranski, E. Lim, and C. S. Chen. 2010. Geometrically Controlled Endothelial Tubulogenesis in Micropatterned Gels. Tissue Eng Pt A 16:2255-2263.

127. Gjorevski, N., and C. M. Nelson. 2010. Endogenous patterns of mechanical stress are required for branching morphogenesis. Integr Biol-Uk 2:424-434.

128. Ng, M. R., A. Besser, G. Danuser, and J. S. Brugge. 2012. Substrate stiffness regulates cadherin-dependent collective migration through myosin-II contractility. Journal of Cell Biology 199:545-563.

129. Thery, M. 2010. Micropatterning as a tool to decipher cell morphogenesis and functions. Journal of Cell Science 123:4201-4213.

130. Aung, A., Y. N. Seo, S. Y. Lu, Y. X. Wang, C. Jamora, J. C. del Alamo, and S. Varghese. 2014. 3D Traction Stresses Activate Protease-Dependent Invasion of Cancer Cells. Biophysical Journal 107:2528-2537.

131. Sadati, M., N. T. Qazvini, R. Krishnan, C. Y. Park, and J. J. Fredberg. 2013. Collective migration and cell jamming. Differentiation 86:121-125.

132. Mumenthaler, S. M., J. Foo, N. C. Choi, N. Heise, K. Leder, D. B. Agus, W. Pao, F. Michor, and P. Mallick. 2015. The Impact of Microenvironmental Heterogeneity on the Evolution of Drug Resistance in Cancer Cells. Cancer Inform 14:19-31.

133. Dimanche-Boitrel, M. T., P. Genne, O. Duchamp, and B. Chauffert. 1994. Confluence dependent resistance (CDR) to doxorubicin and E-cadherin expression in murine mammary cells. Cancer Lett 85:171-176.

134. Xu, H., J. Wu, C. C. Chu, and M. L. Shuler. 2012. Development of disposable PDMS micro cell culture analog devices with photopolymerizable hydrogel encapsulating living cells. Biomed Microdevices 14:409-418.

135. Burridge, P. W., E. Matsa, P. Shukla, Z. C. Lin, J. M. Churko, A. D. Ebert, F. Lan, S. Diecke, B. Huber, N. M. Mordwinkin, J. R. Plews, O. J. Abilez, B. Cui, J. D. Gold, and J. C. Wu. 2014. Chemically defined generation of human cardiomyocytes. Nat Methods 11:855-860.